Dark Matter Search with Cryogenic Phonon-Light Detectors

Dissertation
der Fakultät für Physik
der Ludwig-Maximilians-Universität
München

vorgelegt von
Federica Petricca
aus Italien

angefertigt am
Max-Planck-Institut für Physik
Werner-Heisenberg-Institut
München

München
25.02.2005

1. Gutachter: Prof. Dr. Otmar Biebel

2. Gutachter: Prof. Dr. Wolfgang Dünnweber

Tag der mündlichen Prüfung: 09.05.2005

Kurzfassung

Das Ziel des Dunkle-Materie-Experimentes CRESST (Cryogenic Rare Event Search with Superconducting Thermometers) besteht darin, WIMPs (Weakly Interacting Massive Particles) durch ihre Streuung an Kernen erstmals direkt nachzuweisen. Da die Energie, die in einem solchen Streuereignis auf den Kern übertragen wird, höchstens wenige 10 keV beträgt, ist eine möglichst niedrige Energieschwelle der Detektoren entscheidend für die Empfindlichkeit des Experimentes. Die erwartete Rate an Streuereignissen ist darüberhinaus äußerst gering. Untergrundereignisse, die zu einer Verfälschung des WIMP-Signals führen, müssen daher effizient unterdrückt werden.

Ein CRESST-Detektormodul besteht aus einem szintillierenden $CaWO_4$-Kristall (300 g), der als Tieftemperaturkalorimeter betrieben wird. Neben dem Temperatursignal wird das bei Energiedeposition im Kristall erzeugte Szintillationslicht von einem zweiten, aus einer Siliziumscheibe bestehenden Tieftemperaturkalorimeter nachgewiesen, welches unmittelbar neben dem $CaWO_4$-Kristall angebracht ist. Da durch Neutronen oder WIMPs verursachte Kernrückstöße eine wesentlich geringere Lichtausbeute zeigen als die von α-Teilchen, Elektronen oder γ-Quanten hervorgerufenen Elektronrückstöße, kann damit das ursprüngliche Ereignis identifiziert und Untergrund unterdrückt werden. Zur passiven Untergrundunterdrückung werden die CRESST-Detektoren in einem radioaktivitätsarmen Aufbau betrieben, der in einem unterirdischen Labor untergebracht ist.

Im Rahmen der vorliegenden Arbeit wurden höchstsensitive Tieftemperaturkalorimeter zum Nachweis von Szintillationslicht entwickelt. Da nur etwa 1 % der durch Elektronen oder γ-Quanten in $CaWO_4$ deponierten Energie als Szintillationslicht nachgewiesen wird, ist die Empfindlichkeit der Lichtdetektoren von herausragender Bedeutung für die effiziente Unterscheidung zwischen Elektron- und Kernrückstößen.

Durch die Verwendung von Phononenkollektoren konnte die Wärmekapazität des Temperatursensors unabhängig von der Phononsammeleffizient minimiert und die Detektorsensitivität entscheidend gesteigert werden. Darüberhinaus wurde durch die Verwendung eines dünnen Metallfilms zur thermischen Kopplung der Kalorimeter an das Kältebad die thermische Relaxationszeit des Thermometers an die bei tiefen Temperaturen sehr langsame Lichtemission angepasst.

Darüberhinaus wurden neue Materialien auf ihre Eignung als Absorber für Lichtdetektoren der nächsten Generation untersucht.

Ergebnisse der Erprobungsphase von Prototyp-Detektormodulen, die unter Verwendung obiger Lichtdetektoren im CRESST-Experiment betrieben wurden, und insbesondere die damit erhaltenen kompetitiven Grenzen für WIMP-Parameter werden vorgestellt.

Abstract

The CRESST (Cryogenic Rare Event Search with Superconducting Thermometers) Dark Matter search is aiming to directly detect Weakly Interacting Massive Particles (WIMP) via their elastic scattering off nuclei in a target. Due to the low event rate expected for WIMP-nucleus scattering the suppression of background which would hide or mimic the WIMP signal is of crucial importance. Moreover, since the energy transferred to a nucleus in a WIMP-nucleus elastic scattering is extremely low (a few tens of keV), the energy threshold and the sensitivity of detectors are additional fundamental issues in a Dark Matter search.

CRESST detectors consist of a $300\,\mathrm{g}$ $CaWO_4$ scintillating crystal operated as a cryogenic calorimeter in close proximity to a second much smaller cryogenic calorimeter used to detect the scintillation light produced in the target crystal. The lower light yield of nuclear recoils, caused by neutrons and WIMPs, with respect to electron recoils resulting from α, β and γ interactions is used to identify the event in the scintillating absorber.

In the second phase of the CRESST experiment active background suppression is achieved by the simultaneous measurement of a phonon and a light signal from a scintillating cryogenic calorimeter. Passive background suppression is achieved by operating CRESST detectors in a low background facility located in a deep underground site. About 1% of the energy deposited in $CaWO_4$ by β or γ interactions can be detected as scintillation light; therefore the sensitivity of light detectors is a fundamental issue for the discrimination of electron recoils from nuclear recoils at energies relevant for WIMP searches.

This work reports on the development of extremely sensitive cryogenic calorimeters for the detection of the scintillation light. These detectors applied a new thermometer geometry characterized by phonon collectors and a thin film thermal coupling to the heat sink. This concept allows a high sensitivity by decoupling the area required for the collection of non-thermal phonons and the heat capacity of the sensor and permits to make the thermal relaxation time of the thermometer long enough to allow for the integration of the scintillation light, despite the slow light emission of $CaWO_4$ at low temperature.

Results on new materials to be used as absorbers for a new generation of light detectors are presented.

First competitive limits on WIMP Dark Matter established by the CRESST experiment running scintillating $CaWO_4$ cryogenic detectors in association with the light detectors developed in the course of this work are reported together with main results of the detector prototyping phase.

Contents

iv

Chapter 1

Introduction to Dark Matter

The existence of Dark Matter was first suggested, using simple gravitational arguments, in the 1930s [Zwi33]. Nowadays there is overwhelming indirect evidence for the existence of Dark Matter but, up to the present day, it has not been detected directly despite the increasing experimental effort. Over the last few years precision measurements of the microwave background spectrum, combined with other astronomical and astrophysical data, have yielded the basic parameters of the cosmological model of the Universe with high accuracy. It has been shown that ordinary baryonic matter represents only about 4% of the mass of the Universe, while non-baryonic Dark Matter represents a much larger part, about 26% of the total mass. About 70% of the total density needed for the presently favoured flat Universe is an energy of unknown nature, indicated as Dark Energy.

The Dark Matter enigma appears to find a well-motivated solution in supersymmetric massive particles, generically called WIMPs (Weakly Interacting Massive Particles). The CRESST (Cryogenic Rare Event Search with Superconducting Thermometers) Dark Matter search is an experiment dedicated to the direct detection of WIMPs.

In this chapter arguments for the existence of Dark Matter will be summarized and the main candidates will first be introduced. In the remainder of the chapter more detailed aspects of the WIMP candidate and the methods by which it may be detected directly will be presented.

1.1 Dark Matter motivation

Hubble's observation of an expanding Universe in the 1930s [Hub29], the observed relative abundance of light elements explained by Gamow in the 1940s [Gam46] [Gam48a] together with the first observation of the Cosmic Microwave Background [Pen65] represented a solid base for the now well established Standard

Cosmological Model which is based upon the successful hot Big Bang theory [1].
The theoretical framework of the Cosmological Model is based on general relativity and on the idea that the geometry of space-time is determined by the energy content of the Universe. The early assumption of Einstein and Friedmann of an homogeneous and isotropic Universe as supposed by the "Cosmological Principle" and later confirmed by the detection of the Cosmic Microwave Background, translates to the Friedmann-Robertson-Walker (FRW) metric which is expressed as:

$$ds^2 = c^2 dt^2 - a^2(t) \left[\frac{dr^2}{(1 - kr^2)} + r^2 \left(d\theta^2 + \sin^2 \theta d\phi^2 \right) \right] \tag{1.1}$$

where the scale factor $a(t)$ determines the physical size of the Universe and the constant k characterizes the spatial curvature of the Universe ($k = -1$, 0, $+1$ for a spatially open, flat or closed Universe respectively). Describing the Universe as a perfect fluid, that is a fluid in which an observer comoving with the fluid would see the Universe around as isotropic, the generic Einstein equation for the metric in equation 1.1 yields the Friedmann equation

$$\left(\frac{\dot{a}}{a} \right)^2 + \frac{k}{a^2} = \frac{1}{3} 8\pi G_N \rho_{tot} \tag{1.2}$$

where G_N is Newton's gravitational constant and ρ_{tot} is the total average density of the Universe. In the context of the FRW metric the Universe's expansion first observed by Hubble is characterized by a quantity known as Hubble rate of expansion $H(t) = \dot{a}/a$, with a value today denoted by H_0 [2]. The equation 1.2 can therefore be written as:

$$H^2 = \frac{1}{3} 8\pi G_N \rho - \frac{k}{a^2} + \frac{\Lambda}{3} \tag{1.3}$$

where Λ is the cosmological constant (the term can be associated with the vacuum energy of quantum field theory).

Defining the critical density [Wei72] $\rho_c = 3H^2 / 8\pi G_N$ such that in the absence of a cosmological constant $\rho = \rho_c$ would correspond to a flat Universe, the cosmological density parameter is defined as:

$$\Omega \equiv \frac{\rho}{\rho_c}. \tag{1.4}$$

The Friedmann equation can then be rewritten as :

$$\Omega - 1 = \frac{k}{H^2 a^2} - \frac{\Lambda}{3H^2} \tag{1.5}$$

---

[1] Although powerfully predictive, the hot Big Bang theory suffers from problems concerning the initial conditions.

[2] The present value H_0 can be written in terms of the Hubble parameter h as $H_0 = h \cdot 100 \, \text{km} \, \text{s}^{-1} \, \text{Mpc}^{-1}$ ($1 \, \text{pc} \approx 3 \times 10^{16} \, \text{m}$). Recent observations yield $h = 0.71 \pm 0.04$ [Spe03].

so that the sign of k, in absence of a cosmological constant, is determined by the value of Ω

$$\begin{array}{llll} \rho < \rho_c; & \Omega < 1; & k = -1; & \text{open Universe} \\ \rho = \rho_c; & \Omega = 1; & k = 0; & \text{flat Universe} \\ \rho > \rho_c; & \Omega > 1; & k = 1; & \text{closed Universe.} \end{array}$$

In terms of the critical density it is possible to define the ratios $\Omega_i \equiv \rho_i/\rho_c$ for matter[3], curvature and cosmological constant today as:

$$\Omega_m \equiv \frac{8\pi G_N \rho_m}{3H_0^2}, \quad \Omega_k \equiv \frac{-k}{a_0^2 H_0^2}, \quad \Omega_\Lambda \equiv \frac{\Lambda}{3H_0^2}. \tag{1.6}$$

As a consequence the Friedmann equation of today's Universe can be written as:

$$\Omega_m + \Omega_k + \Omega_\Lambda = 1 \tag{1.7}$$

that is, in the context of a FRW Universe, the total fraction of matter density, spatial curvature and cosmological constant must add up to one.

Despite its predictive power, the Standard Cosmological Model suffers from problems concerning the initial conditions. It does not explain the finite baryon density (i.e. the matter-antimatter asymmetry), the extraordinary flatness and smoothness of the Universe on very large scales and the origin of primordial density perturbations which gave rise to the cosmic structure formation [Pri96].

A cosmic inflation (exponential expansion in the early stage of the Universe) provides a solution to some of these problems. It explains the isotropy and homogeneity on very large scales [GB99b] and in particular it predicts a Universe very close to flat (i.e. $k=0$).

At present there is direct evidence from Cosmic Microwave Background (CMB) anisotropies measurements that Ω is very close to unity ($\Omega_{tot} = 1.02 \pm 0.02$ [Spe03]).

1.1.1 Observational evidence for Dark Matter

The most convincing and direct evidence for Dark Matter on galactic scales comes from the observations of the flat rotation curves of galaxies[4] (see figure 1.1). In newtonian dynamics the rotational velocity is expected to be given by:

$$v(r) = \sqrt{\frac{G\,M(r)}{r}}. \tag{1.8}$$

where $M(r) \equiv 4\pi \int \rho(r) r^2 dr$, with $\rho(r)$ the mass density profile. For a mass distribution concentrated in the optical disk the circular velocity should be falling

---

[3]The radiation component Ω_r to the total density of today's Universe can be safely neglected [GB99a].

[4]Rotation curves are graphs of rotational velocities of stars and gas as a function of their distance from the galactic center.

proportionally to $1/\sqrt{r}$ beyond the visible radius. The fact that $v(r)$ is approximately constant implies the existence of a halo with $M(r) \propto r$ and $\rho \propto 1/r^2$. Despite the uncertainties of the slope in the innermost regions of galaxies there
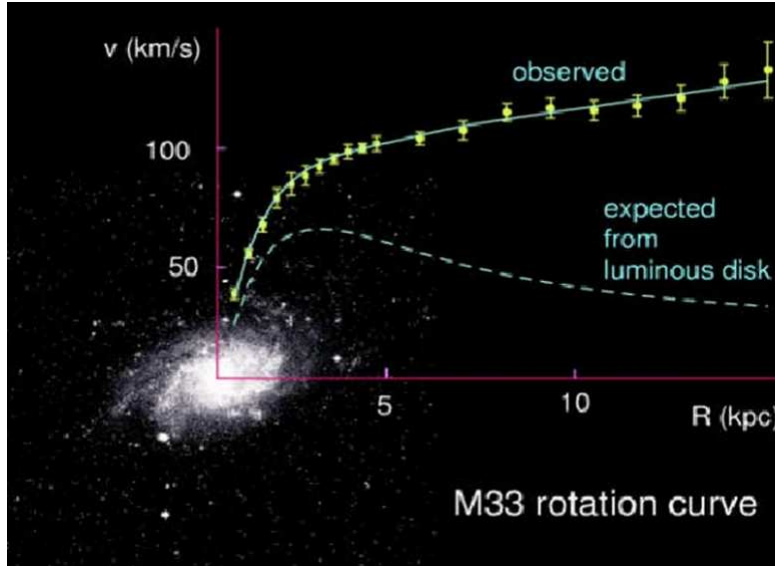

Figure 1.1: Observed rotation curve of the dwarf spiral galaxy M33, superimposed on its optical image. For comparison the expected velocity from the luminous disk is shown [Kha02].

is a consensus about the shape of Dark Matter halos at large distances. The measured rotation curves of disk galaxies provide strong evidence for the existence of a spherical Dark Matter halo. Whereas current observations of luminous matter in galaxies determine $\Omega_{lum} \lesssim 0.01$ [Cop96], analyses of rotation curves imply $\Omega \gtrsim 0.1$ [Kha02].

Besides galactic rotation curves a number of other observations indicate the presence of Dark Matter in both galaxies and galaxy clusters.

Clusters of galaxies are the largest gravitationally bound systems in the Universe and from the observation of the velocity dispersion of galaxies in the Coma cluster in 1933, Zwicky [Zwi33] first inferred the existence of Dark Matter [5]. The mass of clusters can be alternatively estimated from their X-rays emission. Galaxy clusters are in fact the most powerful X-ray sources in the sky; the emission extends over the entire cluster and thus reveals the presence of large amounts of hot gas where X-rays are produced by electron bremsstrahlung [Raf97]. Under the assumption of hydrostatic equilibrium one can fit the measured X-ray profiles to models of temperature and density distribution in order to extract the mass

---

[5]If the cluster is virialized, velocities of galaxies in the cluster are a measure of their potential energy.

of the cluster. Results obtained from these measurements are in good agreement and indicate the existence of a substantial amount of Dark Matter in clusters. The more recent method of studying the gravitational lensing confirms the previous conclusions. Here a cluster acts as a lens which distorts the light emitted by quasars and other galaxies in its background due to the gravitational bending of light (see figure 1.2). All these analyses favour a value of $\Omega \approx 0.2 - 0.3$ ([Bah98], [Kas98], [Car99], [Hoe02]).
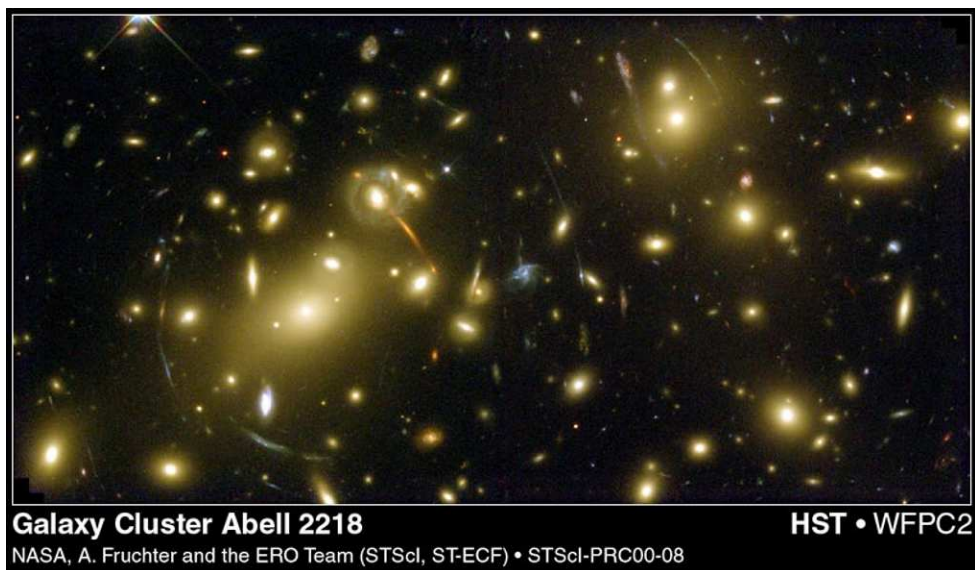
Figure 1.2: Gravitational lensing observed around the galaxy cluster Abell-2218 by the Hubble Space Telescope [hub]. Due to the lensing a luminous source in the background is seen as many arclets surrounding the cluster.

1.1.2 Dark Matter problems

On distance scales of the size of galaxies and clusters of galaxies observational evidence for Dark Matter appears to be compelling, but the observations do not allow estimation of the total amount of Dark Matter in the Universe. This information has been recently extracted from the precision analysis of the Cosmic Microwave Background [Spe03].

The existence of background radiation originating from photons created in the early Universe was already predicted in the 1940s [Gam48b] but it was (unintentionally) discovered only in 1965 by Penzias and Wilson [Pen65].

After decades of experimental effort the CMB is known to be isotropic at the 10^{-5} level and to follow the spectrum of a black body corresponding to a temperature $T = 2.762\,\mathrm{K}$. Today the analysis of its anisotropies (see figure 1.3) enables

accurate testing of cosmological models and puts stringent constraints on cosmological parameters [col03].

Figure 1.3: CMB temperature fluctuations observed by WMAP. Image courtesy of WMAP Science Team.

The precision data of WMAP CMB measurements [Spe03] taken in combination with the supernova discovery of acceleration of the cosmic expansion [Kno03] has led to a "concordance model" (ΛCDM):

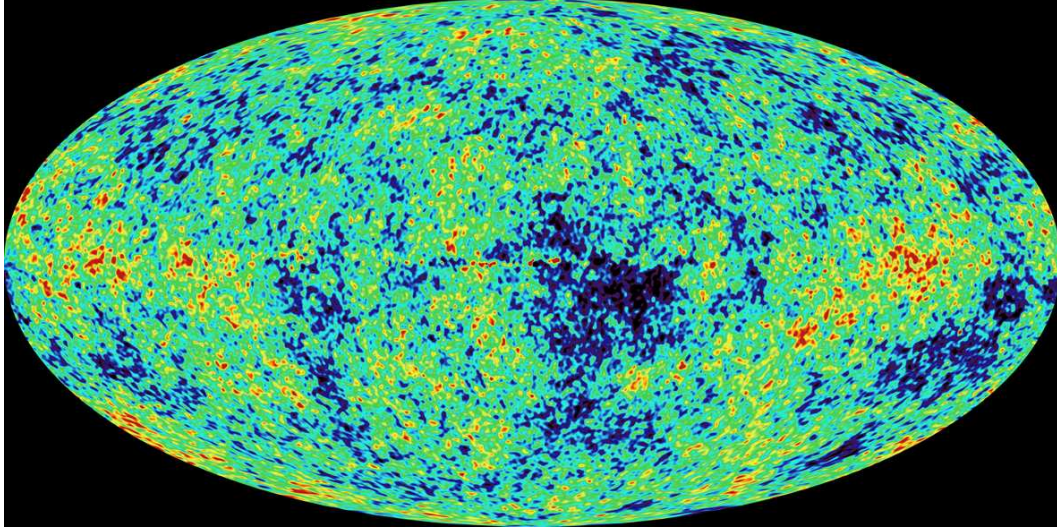$$\left\{ \begin{array}{l} \Omega_m \approx 0.27; \\ \Omega_\Lambda \approx 0.73. \end{array} \right.$$

This is in good agreement with the inflationary prediction of the matter and cosmological constant contributions adding up to unity, but produces the mystery of having a non-zero but exceedingly small value of the cosmological constant compared to the natural scale of gravity which is the Planck scale. The contribution of the luminous matter to the matter density ($\Omega_{lum} = 0.002 - 0.006$ [Cop96]) is, however, far too small to account for Ω_m, indicating the presence of non-luminous matter in the Universe whose nature is not yet fully understood. The Big Bang Nucleosynthesis (BBN) sets stringent constraints on the baryon contribution Ω_b to Ω_m. Recent measurements yield a value $\Omega_b = 0.044 \pm 0.004$ [Spe03].
The concordance model is summarized in figure 1.4. As illustrated in the picture, between the baryon density predicted by the combination of CMB and BBN and the measured contribution of the luminous matter to the matter density there is a fraction of Dark Matter in the form of baryons while the difference between the best fit for Ω_m and the predicted Ω_b must be in the form of non-baryonic Dark Matter.
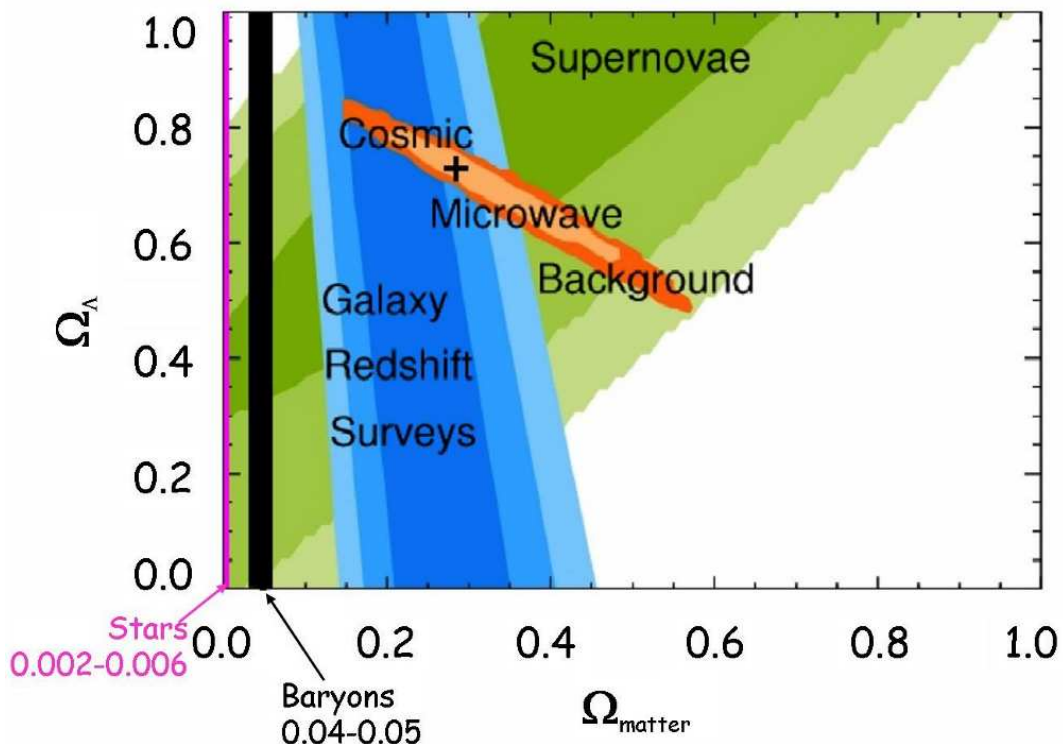
Figure 1.4: Current cosmological constraints on the matter density Ω_m and the energy density Ω_Λ give the best estimate marked with a cross at Ω_m=0.27, Ω_Λ=0.73. The baryon density (black vertical band) does not exceed 0.05. The rest of the matter is non-baryonic. Luminous matter (pink vertical band) does not contribute more than 0.006. Figure adapted from [Gon04].

1.2 Dark Matter candidates

The evidence for the existence of Dark Matter is compelling on all astrophysical scales. The inventory of Dark Matter candidates is rather large. Whereas baryonic Dark Matter is in the form of relatively "standard" astrophysical objects like cold hydrogen clouds or compact objects as neutron stars, brown dwarfs or black holes[6], the nature of the missing density needed to account for the result in section 1.1.2 is still subject to speculation.

While the cause and exact nature of the Dark Energy remains mysterious, there is increasing hope to connect the non-baryonic Dark Matter to current models of particle physics. Supersymmetric models provide several excellent candidates, with the lightest neutralino being the prime example.

---

[6]These astrophysical bodies are collectively known as MAssive Compact Halo Objects (MACHOs).

1.2.1   Baryonic candidates

As illustrated in figure 1.4 a significant fraction of the expected amount of baryonic matter is dark in the sense that it neither emits nor absorbs light. This results in stringent observational limits on many plausible candidates [Spi99] [Spi00]. Thus baryonic Dark Matter cannot be in the form of hot diffuse gas as this would result in a larger X-ray flux than the observed one, nor in the form of cold gas since it would absorb light and re-emit it in the infrared. Neutron stars or black holes that are created in supernova explosions would eject heavy elements into the galaxy and thus could be spectroscopically observed. White dwarfs, stars that are not massive enough to reach the supernova phase, are a good candidate. However they would produce too much light or too many metals and helium that have not been observed. The most plausible candidates are brown dwarfs, stars with small mass ($0.01\,\mathrm{M_\odot} < \mathrm{M} < 0.08\,\mathrm{M_\odot}$) which never ignite hydrogen and thus shine only due to gravitational contraction. As most of the stars are small one would expect a significant number of such objects in the galaxy. Up to the present time their existence is difficult to prove, nevertheless they appear to be the most plausible candidate of baryonic Dark Matter. Finally, primordial black holes which have been created in the early Universe could also be a good candidate, but the main objection against them is the lack of a plausible mechanism for their formation.

1.2.2   Non-Baryonic candidates

A major classification of non-baryonic Dark Matter is based on its temperature at the time of decoupling from thermal equilibrium. The reason for such a classification originates from the fundamentally different consequences for structure formation in the Universe.

Hot Dark Matter candidates (HDM) were relativistic at the time of decoupling. Such particles would stop only in very large overdensities; as a consequence the first structures formed would be clouds of HDM particles of supergalactic size, all smaller fluctuations being erased by the free streaming, followed by the infall of the baryonic matter after recombination. HDM models yield therefore to a top-down scenario where supergalaxies are formed first and galaxies later from their collapse[7].

Cold Dark Matter candidates (CDM) were non relativistic at the time of decoupling. As a consequence when the Universe became matter dominated and galaxy formation started they were slow enough to be bound in perturbations on the galactic scale. CDM models do produce galaxies naturally and large scale

---

[7]There are several examples of galaxies older than the group in which they are; in addition in this scenario galaxies in clusters would be expected to fall in rather than streaming away.

structures have to be assembled from them later[8].

The intermediate state of warm Dark Matter that was semi-relativistic at the time of galaxies formation has been proposed as well.

N-body simulations of huge parts of the Universe showed that a consistent scenario results for a substantial cold Dark Matter component and a subdominant hot Dark Matter component [Dav85].

Another important classification of particle Dark Matter rests upon its production mechanism. Particles which were in thermal equilibrium in the early Universe are classified as thermal relics (neutrinos, neutralinos and most other WIMPs) while particles which were produced by a non-thermal mechanism and which never had the chance of reaching thermal equilibrium in the early Universe are called non-thermal relics (axions).

Here only the best motivated and most interesting candidates will be presented.

Neutrinos

Dark Matter candidates that are known to exist in nature have an obvious advantage over candidates that have not been detected. The chief particles in this category are the neutrinos.

In recent years observations of solar and atmospheric neutrinos have indicated that they do have a mass; this means that neutrinos could compose a fraction of the Dark Matter. A stringent limit on the neutrino relic density comes from the analysis of the CMB combined with large scale structures' data, suggesting $\Omega_\nu h^2 < 0.0067$ (95% C.L.). Such an upper limit forbids currently known neutrinos from being a major constituent of Dark Matter. Moreover, since they are light[9] and relativistic at the time of galaxies formation, the three known neutrinos are a hot, therefore subdominant, Dark Matter component.

Axions

These hypothetical light pseudoscalar particles, introduced in the attempt to solve the strong CP problem[10] [Pec77], have often been discussed as Dark Matter candidates [Tur90].

Laboratory searches [col04a], stellar cooling and the dynamics of the supernova SN1987A constrain axions to be very light and to have an extremely small coupling to ordinary matter and therefore an extremely long lifetime (many orders

---

[8]In this scenario there is not enough time to achieve the observed structure within the known age of the Universe.

[9]The best laboratory constraint on neutrino masses comes from tritium β-decay experiments [Wei03] which give an upper limit on the neutrino mass of $m_i < 2.05$ eV (95% C.L.) that applies for all three active neutrinos mass eigenvalues since the mass differences among them are constrained by the observation of flavor oscillation [GG03].

[10]This problem arises because Quantum Chromo Dynamics includes in its Lagrangian a CP violating term, and therefore there are important experimental bounds against it.

of magnitude larger than the age of the Universe). Axions that would have been produced in the Big Bang[11], were never in thermal equilibrium and always non-relativistic (i.e. they are cold Dark Matter). The calculation of axion relic density depends on the assumption made regarding the production mechanism. Nevertheless it is possible to find a range where axions satisfy all present day constraints to represent a possible Dark Matter candidate [Ros00].

Supersymmetric candidates - WIMPs

Supersymmetry is a symmetry of space-time that has been introduced in the process of unifying the fundamental forces of nature. Of importance for cosmology is the fact that supersymmetry requires the existence of a new particle for each particle in the Standard Model of particle physics[12]. If supersymmetry were an explicit symmetry of nature, superpartners would have the same mass as the Standard Model particles. To explain why superpartners have not been detected so far, it is assumed that supersymmetry is broken; superpartners can therefore be much heavier than their normal counterpart.

The minimal supersymmetric extension of the Standard Model is denoted as the Minimal Supersymmetric Standard Model (MSSM). The MSSM is minimal in the sense that it contains the smallest possible field content to give rise to all fields of the Standard Model. One assumption of the MSSM is the conservation of the R-parity[13], R being a multiplicative quantum number defined as:

$$R \equiv (-1)^{3B+L+2s} \tag{1.9}$$

where B, L and s are baryon, lepton and spin numbers respectively. It follows that $R = 1$ for ordinary particles while $R = -1$ for superpartners. As a consequence the lightest supersymmetric particle (LSP) is stable and can only be destroyed via pair annihilation, making it an excellent Dark Matter candidate. The LSP in the MSSM cannot have a non-zero electric charge or color, otherwise it would have condensed with baryonic matter producing heavy isotopes, in conflict with observations.

Among possible LSP, the best motivated Dark Matter candidate is the lightest neutralino, χ, that is the lightest of the four Majorana fermionic mass eigenstates obtained from the mixing of the superpartners of the neutral electroweak gauge bosons and of the neutral Higgs bosons.

Neuralinos represent a particular realization of a generic Weakly Interacting Massive Particle (WIMP).

---

[11] Axions could also be produced in the core of the stars by means of the Primakoff conversion of the plasma photons.

[12] Supersymmetric partners differ by half a unit of spin. Such a transformation turns fermions into bosons and vice-versa.

[13] R-parity was first introduced to suppress the rate of proton decay.

WIMPs were in thermal equilibrium with ordinary particles in the early Universe and were non-relativistic at the time of decoupling. The relic density of such a thermal WIMP can be calculated from the freeze-out condition (annihilation rate equal to the expansion rate of the Universe H) as:

$$\Omega h^2 = \frac{\rho}{\rho_c} h^2 \approx \frac{3 \times 10^{-27} cm^3 s^{-1}}{\langle \sigma_{ann} v \rangle} \qquad (1.10)$$

where σ_{ann} is the total cross section for annihilation of a pair of WIMPs into standard model particles, v is the relative velocity between the two WIMPs and $\langle ... \rangle$ denotes thermal averaging.

From equation 1.10 it is possible to see that the canonical weak interaction cross section is just right to make the relic density in the range needed to obtain the observed density of the Universe. This raises the hope of detecting relic WIMPs directly [Goo85] [Was86].

The aim of the CRESST experiment is to search for WIMPs as non-baryonic Dark Matter candidates.

1.3 Dark Matter searches

Direct detection experiments appear today as one of the most promising techniques to detect WIMP Dark Matter [14]. The basic idea on which all direct detection experiments are based relies on the fact that WIMPs cluster gravitationally with ordinary matter in galactic halos and therefore must be present in our own galaxy. As a consequence there will be a flux of these particles on the Earth, making possible the detection of the interaction of such particles with ordinary matter.

In addition to detecting WIMPs directly, there are methods for the indirect detection by looking for evidence of WIMP annihilations in the galactic halo, in the center of the Sun or other regions.

1.3.1 Direct detection

The physics underlying the direct detection technique is the scattering of a WIMP with the material of a detector placed on the Earth. The two quantities which are crucial for direct detection experiments are the local Dark Matter density ρ_0 and the velocity dispersion of Dark Matter particles $\bar{v} = \langle v^2 \rangle^{1/2}$. Rotation curves, that are the most important observational quantities in determining ρ_0 and $\bar{v}$, are much better known for external galaxies than for the Milky Way due to the

---

[14]It is worth noticing that there are several accelerator experiments in preparation in order to detect supersymmetric particles.

position of the Earth inside the galaxy[15]. Using an isothermal sphere model for the Dark Matter halo, at the position of the Sun (around $8.5\,\mathrm{kpc}$ away from the galactic center) the mean density of particles trapped in the gravitational potential well of the galaxy is expected[16] to be $\rho_0 \approx 5 \times 10^{-25}\,\mathrm{g\cdot cm^{-3}} \simeq 0.3\,\mathrm{GeV\cdot cm^{-3}}$ [Jun96]. In this model the local velocity distribution in the galactic rest frame (the halo is assumed to be non rotating) is Maxwellian[17], that means

$$f(v)d^3v = (1/v_0^3\pi^{3/2})\exp(-v^2/v_0^2)d^3v \qquad (1.11)$$

where v_0 is the velocity at the local position. The velocity dispersion $\overline{v}$ is directly related to the asymptotic flat rotation velocity as [Bin87] $\overline{v} = \sqrt{3/2}v_\infty$. In the Milky Way the rotation curve appears to be already flat at the local position with $v_\infty = v_0 = 220 \pm 20\,\mathrm{km\cdot s^{-1}}$ [Ker86], therefore $\overline{v} = 270 \pm 25\,\mathrm{km\cdot s^{-1}}$. To evaluate the WIMP interaction rate, equation 1.11 has to be transformed to the rest frame of the Earth, which moves through the galaxy with a velocity $v_\odot = 232 \pm 20\,\mathrm{km\cdot s^{-1}}$.

Within the direct detection techniques an important distinction has to be made between the detection through elastic and inelastic scattering with nuclei.

The elastic WIMP-nucleus scattering in a detector is simply the interaction of the WIMP with the nucleus as a whole, causing it to recoil. Here the observed signal is the recoil energy spectrum in the target, therefore detector sensitivity for nuclear recoils is crucial.

In the case of inelastic scattering the WIMP interacts with orbital electrons in the target, either exciting them or ionizing the target. Alternatively the WIMP could interact with a target nucleus leaving it in an excited nuclear state. In the latter case the signature is a recoil followed by a photon emission that has to compete with background of natural radioactivity.

In the remaining part of the section the attention will be limited to the direct detection through elastic scattering on nuclei that represents the most relevant direct detection process.

Theoretical event rate

Knowing the density and the velocity distribution of WIMPs in the solar neighbourhood, it is possible to evaluate the rate of events expected in an experiment

---

[15]Although the available data on our galaxy do not provide a compelling evidence for a flat rotation curve, the feature is observed for a large number of spiral galaxies and therefore it looks reasonable to assume its validity for the Milky Way.

[16]The uncertainty comes from the uncertainty in the measured rotation curve, from the uncertainty in the dark halo model considered and from the uncertainty in the contribution of the disk to the rotation curve. A comprehensive numerical study [Gat95] indicates that ρ_0 falls in the (conservative) range $0.1 \lesssim \rho_0 \lesssim 0.7\,\mathrm{GeV\cdot cm^{-3}}$.

[17]The distribution is truncated by an escape velocity whose value is somewhat uncertain [Leo90]. The reference value $v_{esc} \approx 650\,\mathrm{km\cdot s^{-1}}$ is generally used [Bot97].

as

$$R \approx \sum_i N_i n_\chi \langle \sigma_{i\chi} \rangle \tag{1.12}$$

where the index i runs over nuclei species present in the detector, N_i is the number of target nuclei of the species i present in the detector, n_χ is the local number density of WIMPs and $\langle \sigma_{i\chi} \rangle$ is the cross section for the elastic scattering of WIMPs off nuclei of species i, averaged over the relative WIMP velocity with respect to the detector [Ber05].

Elastic scattering cross section

WIMP scattering off nuclei is commonly discussed in the context of two classes of couplings. Spin dependent (axial) interactions result from the coupling to the spin content of a nucleon, therefore the cross section for spin dependent scattering is proportional to $J(J+1)$ rather than the number of nucleons as in the case of spin independent (scalar) cross section.

Both spin dependent and spin independent cross sections are modified at high momentum transfer q by form factors[18] $F(E_r)$ that reflect the spatial distribution of nucleons inside the nucleus, E_r being the recoil energy. When the momentum transfer to the nucleus q ($q^2 \equiv |\bar{q}|^2 = 2 m_N E_r$, m_N being the mass of the target nucleus) is such that the de Broglie wavelength $\lambda = h/q$ is smaller than the size of the nucleus, the effective scattering cross section decreases with increasing momentum.

While spin independent form factors are simply related to nuclear densities, spin dependent cross sections reflect delicate aspects of nucleonic and nuclear structure [Eng92]. For the coherent process of spin independent scattering the form factor can be derived analytically, being defined at non-zero momentum transfer as the Fourier transform of the nuclear matter distribution. In contrast, in the spin dependent case the form factor calculations require significant effort since nuclear properties have to be calculated for each nucleus with an appropriate nuclear model (for detailed calculations see for example [Ber05] [Jun96]).

The effective cross section for both types of interaction can be written thus

$$\sigma = \sigma_0 F^2(E_r) \tag{1.13}$$

where σ_0 is the zero momentum transfer cross section which contains all dependencies on the specific interaction and $F(E_r)$ depends only on the momentum transfer.

The cross section at zero momentum transfer for spin independent WIMP interaction is related to the mass of the target nucleus by the relation [Lew96]:

$$\sigma_{0si} \propto \mu^2 m_N^2 \tag{1.14}$$

---

[18]The form factor parameterizes the loss of coherence due to the finite size of the nucleus for the WIMP-nucleus interaction as the energy of the WIMP increases.

where μ is the reduced mass ($\mu = (m_\chi m_N)/(m_\chi + m_N)$). In the case of spin dependent interaction [Lew96]

$$\sigma_{0sd} \propto \mu^2 \lambda^2 J(J+1) \tag{1.15}$$

where $\lambda^2 J(J+1)$ is the nuclear spin factor. Equation 1.14 indicates that, for coherently interacting WIMPs, massive nuclei are desirable since the interaction cross section scales as the nucleus mass squared. However in this case coherence losses must be considered. The spin dependent cross section in equation 1.15 indicates instead that the most desirable detector nuclei are those that maximize energy transfer, i.e. which match nuclear and WIMP masses. Relatively small nuclear masses are therefore favoured.

A generic WIMP will have both scalar and axial interactions with the nucleus. The differential and total event rate will be therefore the sum of the differential and total event rate for the two interactions.

Recoil energy spectra

As WIMP velocities are non-relativistic, the energy E_r deposited in a detector due to the WIMP nucleus elastic scattering is expressed as:

$$E_r = \frac{m_\chi^2 m_N}{(m_\chi + m_N)^2} v^2 (1 - \cos\theta) \tag{1.16}$$

where m_χ and v are WIMP mass and velocity respectively and θ is the scattering angle in the center of mass frame. The differential rate per unit detector mass for the elastic WIMP-nucleus scattering is given by the relation [Jun96]:

$$\frac{dR}{dE_r} = \frac{\rho_0 \sigma_0}{2m_\chi \mu^2} F^2(E_r) \int_{v_{min}}^{v_{esc}} \frac{f_1(v)}{v} dv; \quad v_{min} = \sqrt{\frac{E_r m_N}{2\mu^2}} \tag{1.17}$$

where $f_1(v)$ is the distribution of speeds relative to the detector, found by integrating over angles the three-dimensional velocity distribution in equation 1.11. The total event rate is computed by integrating dR over all possible incoming velocities and over deposited energies between the detector threshold E_{thr} and $E_{max} = 2\mu^2 v^2/m_N$. By using the energy transfer, the dependence on WIMP velocities is confined to one integral. Defining the dimensionless quantity

$$T(E_r) = \frac{\sqrt{\pi}}{2} v_0 \int_{v_{min}}^{v_{esc}} \frac{f_1(v)}{v} dv \tag{1.18}$$

equation 1.17 can be written as:

$$\frac{dR}{dE_r} = \frac{\rho_0 \sigma_0}{\sqrt{\pi} v_0 m_\chi \mu^2} F^2(E_r) T(E_r). \tag{1.19}$$

Neglecting for simplicity the motion of the Sun[19] and the Earth and integrating over angles the Maxwellian velocity distribution of WIMPs in equation 1.11 to find the speed distribution $f_1(v)dv$, equation 1.19 becomes:

$$\frac{dR}{dE_r} = \frac{\rho_0 \sigma_0}{\sqrt{\pi} v_0 m_\chi \mu^2} F^2(E_r) \exp\left(-\frac{E_r m_N}{2\mu^2 v_0^2}\right). \tag{1.20}$$

The integration to obtain the total event rate requires the knowledge of the dependency of the form factor on the deposited energy [Lew96].
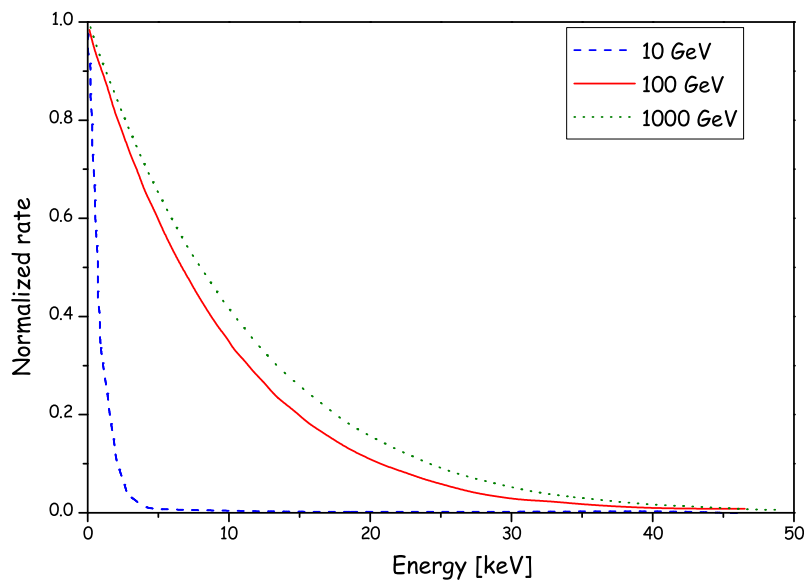

Figure 1.5: Normalized recoil spectrum for WIMP elastic scattering on $CaWO_4$ for WIMP masses of 10, 100 and $1000\,GeV/c^2$.

Figure 1.5 illustrates the quasi-exponential dependence of the signal rate as a function of recoil energy for three different WIMP masses having $CaWO_4$ as target material. It is worth noticing that, in the case of $CaWO_4$, the expected recoil energy spectrum extends only up to about $40\,keV$.

Experimental requirements

The described characteristics of the WIMP-nucleus elastic scattering determine the main experimental requirements for direct detection experiments based on this interaction, namely:

---

[19]The motion of the Sun has a large effect on the shape of the spectrum, therefore it cannot be neglected when computing the rate expected in an experimental setup (see below).

Energy threshold as low as possible due to the quasi exponential decreasing
of the signal as a function of the recoil energy.

Target mass as high as possible in order to compensate the small cross section
for WIMP-nucleus elastic scattering.

Background highly suppressed in order to allow a spectrum of rare nuclear
recoils to be observed.

The suppression of background is particularly important due to the fact that the
sensitivity of a WIMP search is determined by the ability to detect a WIMP
energy spectrum on top of a background spectrum of unknown shape. For this
purpose various experimental strategies have been developed.

To have positive evidence with detectors that cannot distinguish WIMP interac-
tions from background, the expected exponential recoil energy spectrum has to
be observed on top of the background. Conversely, such a detector can exclude a
WIMP model if the model predicts a spectrum with a higher event rate than the
observed background. In this case, when no events are observed, the sensitivity
improves as MT, where M is the detector mass and T its exposure time. The
maximum WIMP exclusion sensitivity is limited by the background level and an
increase of the target mass or of the exposure time yields no improvement.

The experimental sensitivity can be enhanced by applying a background sub-
traction. This strategy presumes an independent knowledge of the background
spectrum. In this case the WIMP spectrum is represented by the residuals. For
a background model perfectly fitting the observed spectrum the sensitivity im-
proves as $\sqrt{MT}$ due to fluctuations of the background. In such analysis the
required accuracy of the background model also grows with time in order for
statistical errors to dominate. Most experiments applying the background sub-
traction eventually reach the point where the systematic error on the subtraction
starts to dominate over the statistical error. When this situation is reached the
experimental sensitivity cannot be improved further.

A different strategy to enhance the experimental sensitivity, pursued by many
groups, relies on the ability of detectors to distinguish the background. Due
to the fact that WIMPs and neutrons interact predominantly with nuclei while
ionizing radiation interacts predominantly with atomic electrons, the possibility
of detectors to discriminate among nuclear and electron recoils establishes an
efficient background rejection technique.

Signatures for direct detection

Taking into account the motion of the Sun and the Earth in equation 1.19 results
in an increase of the event rate and yield a yearly modulation in the event rate
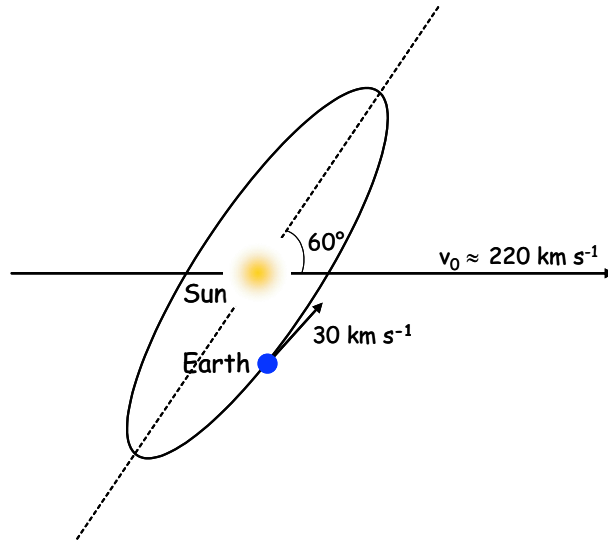which might serve for discriminating background from a Dark Matter signal.

Figure 1.6: Schematic view of the Earth's motion around the Sun.

For example as shown schematically in figure 1.6, in June the Earth's rotation velocity adds to the Sun velocity through the halo (with a maximum around June 2) whereas in December the two velocities are in opposite direction. When this is taken into account the Earth velocity is given by [Fre88]:

$$v_E = v_0 \left\{ 1.05 + 0.07 \cos \left[\frac{2\pi(t - t_m)}{1 \ year} \right] \right\} \tag{1.21}$$

where t_m=June 2± 1.3 days. This fluctuation produces a rate variation of about 7% over the course of the year, therefore direct detection experiments based on this signature need large statistics.

A second possible WIMP signature arises from the detector material dependence. From equation 1.20 it can be seen that the WIMP rate and the spectral shape depend on the target material; as a consequence experiments that use different target materials in the same setup could identify the WIMP signal by comparing rates and spectra. This method would require a positive signal exceeding the expected background[20] and is within the potential of the second phase of the CRESST experiment.

The most convincing WIMP signature in a direct detection experiment would arise from the directional asymmetry of the recoiling nuclei, given a direction sensitive detector. In this case the directionality would be subject to additional diurnal modulation by the Earth's rotation about its axis. In the case of a

---

[20]Due to the low WIMP event rate, such a sensitivity can be reached by experiments with large mass, low threshold and a nuclear recoils discrimination capability.

positive signal the diurnal modulation would represent the most sensitive proof of WIMP interactions.

WIMP exclusion limits

The difficulty of direct detection experiments in constraining the WIMP interaction cross section arises from the fact that the shape of the expected energy spectrum is known with the exception of the normalization, and in addition to the expected signal there might be a contribution from a background of unknown shape contaminating the data.

To set an upper limit for the cross section the value of σ is varied until the resulting theoretical event rate becomes incompatible with the observed event rate and this is done for all possible WIMP masses. Any set of the parameter space which produces a theoretical event rate exceeding this limit is then excluded to a given confidence level (usually 90% CL) without any assumption on the background shape. As a first step in the calculation procedure the theoretical WIMP recoil spectrum has to be convoluted with experimental resolution and then, for a given mass, compared with the observed spectrum applying criteria that would produce 90% CL exclusion limits. Different criteria for deciding the compatibility of expected and observed spectra have been applied by the various experiments ([Gre02], [Tov00], [Ang02], [Yel02]). The analysis of the CRESST data is based on the "optimum interval method" proposed by Yellin [Yel02].

Direct detection experiments

As already mentioned, existing experiments can be classified along the lines of whether or not the detectors are able to distinguish between a possible WIMP signal and background on an event by event basis.

• Non-discriminating experiments

Classical germanium *ionization detectors* have been applied to Dark Matter searches since the 1980s. These detectors are characterized by an excellent energy resolution and a very high radiopurity level, but are intrinsically limited by the restricted choice of target materials and the lack of discrimination capability. Due to the substantial effort spent in obtaining low background conditions, the lowest background rate (0.05 counts/kg/keV/day above 15 keV) without background rejection technique has been obtained by the Heidelberg-Moscow experiment (HDMS) located in the Gran Sasso Laboratory [Bau99]. The best result from germanium ionization detectors has been obtained by the IGEX experiment located at Canfranc Underground Laboratories [Ira02] that could exclude a WIMP-nucleon cross section larger than about 10^{-5} pb for WIMPs of about 100 GeV (see figure 1.8).

At present, the project GERDA has been proposed which will operate 100 kg of

high purity germanium enclosed in high purity liquid nitrogen. The proposed MAJORANA project is aiming for the operation of 1/2 ton of high purity ^{76}Ge detectors.

Several WIMP searches make use of *scintillation detectors*, mostly NaI (pure or doped with Tl) or liquid xenon detectors. In spite of their poorer energy resolution and radiopurity with respect to germanium detectors, they have the advantage of a wide choice of materials and the possibility to build large detector masses with limited costs. Many different groups are using NaI as target material (DAMA, ANAIS, ELEGANT, NAIAD) but the best results have been obtained by the DAMA collaboration investigating the annual modulation in the count rate during 7 years of data taking in Gran Sasso Laboratory, corresponding to a total exposure of 107000 kg day (see figure 1.7). The observed annual modulation in the count rate is stated to be compatible in phase and amplitude with a signal from WIMPs of ~ 52 GeV mass and spin-independent WIMP-nucleon cross section of 7.2×10^{-42} cm^2 [Ber03]. The DAMA experiment was upgraded in 2002 to the LIBRA setup which is currently running 250 kg of NaI crystals. The UKDMC group is using liquid xenon scintillator detectors. The ZEPLIN-I
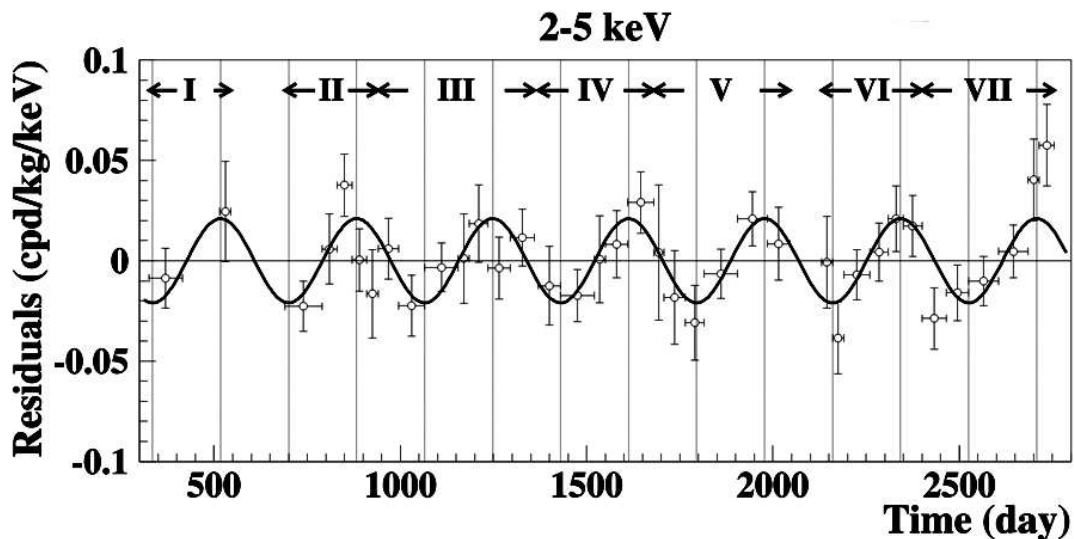

Figure 1.7: Model independent residual rate for events in the (2-5) keV energy interval as a function of the time elapsed since January 1st of the first year of data taking [Ber03]. The superimposed curve represents the cosinusoidal behaviour expected from the annual modulation.

setup consists of a 4 kg prototype detector, located in the Boulby mine in the UK, in which the scintillator is viewed by three photomultipliers whose coincidence allows background suppression.

The CRESST Phase I experiment used sapphire *cryogenic detectors* and, as will

be discussed later, gave the best sensitivity for low WIMP masses with spin-dependent interaction. However, due to the non-discriminating technique, it was limited by the residual background in the detector [Ang02].

• Discriminating experiments
A significant number of experiments which apply an event by event discrimination make use of *cryogenic detectors* (CDMS, EDELWEISS CRESST-II).
The CDMS experiment, located in the Soudan mine, operates germanium and silicon cryogenic detectors with both superconducting thin films and NTD-GE thermistors as temperature sensors [Abr02]. The electron recoil discrimination is achieved by drifting ionization charges to thin film electrodes on the crystal surface. This experiment gives at present the most competitive exclusion limits as can be seen from figure 1.8 [col04b]. The EDELWEISS collaboration, based in the Frejus Underground Laboratory, operated three $320\,\mathrm{g}$ germanium detectors similar to those used by the CDMS collaboration, equipped with NTD-Ge sensors and aluminium thin film charge collection electrodes [Ben02]. Currently the experiment is in preparation for its second phase that promises to operate $30\,\mathrm{kg}$ of detectors. Both groups exclude the DAMA signal region with a high confidence level. Recent publications have shown that this exclusion also resists to variations of the halo model parameters [Cop03], [Kur04].
The CRESST experiment will be extensively discussed in the remainder of this work.
A number of experiments using liquid xenon *scintillation detectors* are being proposed. In these detectors the event by event discrimination is obtained by pulse shape analysis (XENON [Apr04]) or via the simultaneous measurement of ionization and scintillation in liquid xenon time projection chambers (ZEPLIN-II(III) [Har02], XMASS).

The next generation experiments that are close to come, such as EDELWEISS-II, CDMS-II, CRESST-II, ZEPLIN-III, are aiming for an improvement of about 2 orders of magnitude to test a WIMP-nucleon cross section $\sigma \gtrsim 10^{-44}\,\mathrm{cm^2}$ which would allow them to probe interesting parts of the parameter space of MSSM (see figure 6.16). Such an improvement will be obtained with improved discrimination and a significant increase of the detector mass which has to be achieved having special care in satisfying all the radiopurity constraints in order not to have a background limited sensitivity. It already appears clear that both experimental issues and data analysis will prove to be extremely challenging. Combining results from different target materials and cross-checking with different signatures may prove to be the only way to ever ascertain the existence of WIMPs with reasonable confidence. For a comprehensive overview on the future of Dark Matter direct detection see [dmf].
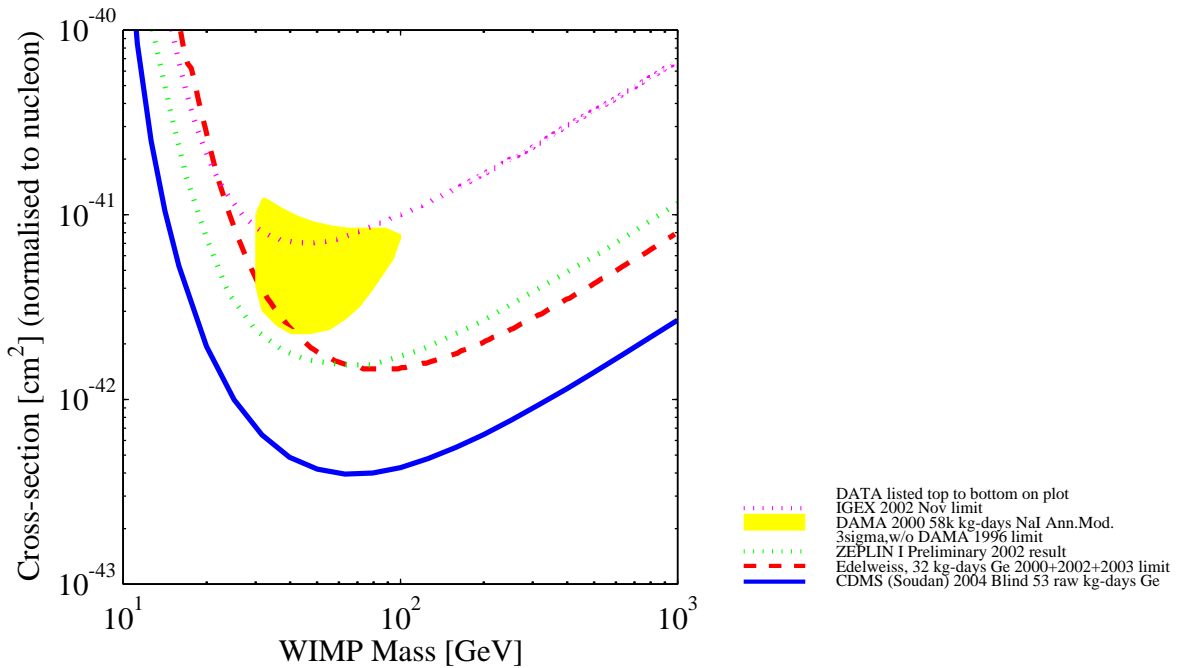
Figure 1.8: WIMP mass - cross section upper limits by several leading experiments. The regions above the curves are excluded; the filled region indicates the DAMA evidence. Figure from [Gai].

1.3.2 Indirect detection

Notwithstanding the strong uncertainties on the detection rates of indirect searches due to uncertainties in the matter distribution, there are various promising methods for the indirect detection of Dark Matter.

WIMPs passing through the Sun and/or Earth may be slowed below escape velocity by elastic scattering; from subsequent scattering they will sink to the center and accumulate there annihilating with other WIMPs. Decays of the annihilation products will produce energetic neutrinos that can be detected by neutrino telescopes. In particular in underground, underwater and under-ice experiments, via the upgoing muons produced by their interactions.

Another way of detecting WIMPs indirectly is through anomalous cosmic rays produced by their annihilation in the galactic halo, using specific products expected from the annihilation to distinguish a possible signal from the standard background of typical cosmic rays.

In some theoretical scenarios indirect detection experiments might be competitive with direct searches [Fen01].
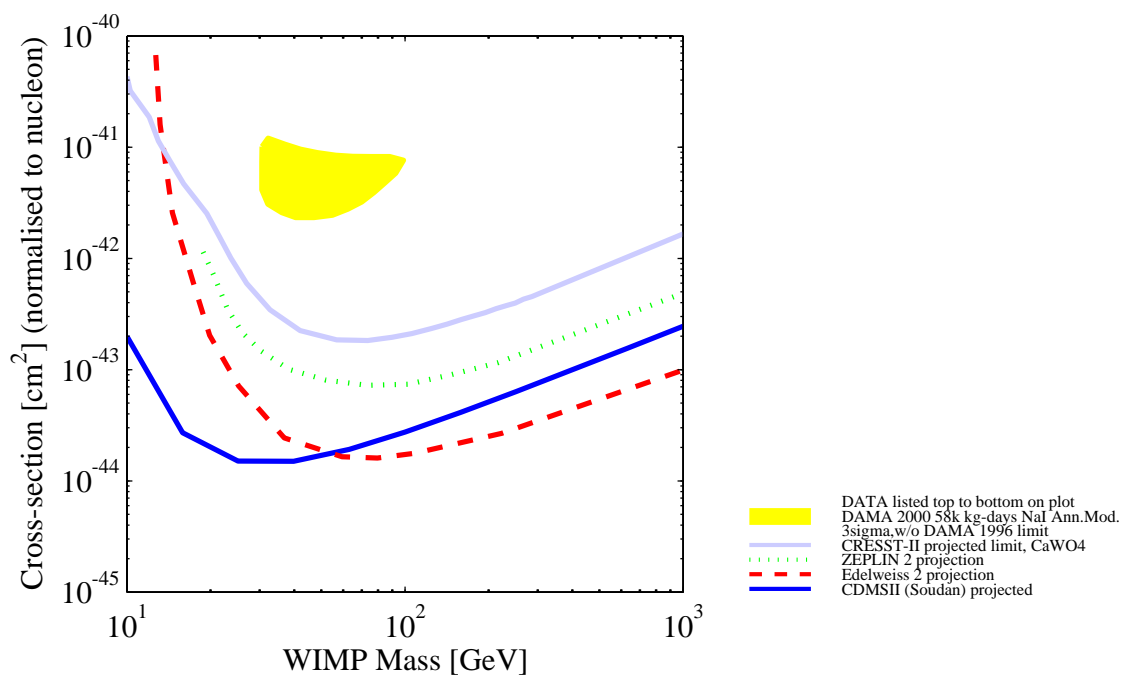
Figure 1.9: Projected sensitivity of some of the next generation experiments in the WIMP mass - cross section parameter space. The filled region indicates the DAMA evidence. Figure from [Gai].

Chapter 2

The CRESST experiment

The aim of the CRESST (Cryogenic Rare Event Search with Superconducting Thermometers) experiment is to detect WIMP Dark Matter particles via their elastic scattering on target nuclei in the absorber of a cryogenic detector.
As discussed in the previous chapter (see 1.3), due to the small energy deposited in a detector by a WIMP-nucleus elastic scattering event and the small expected event rate, it is of crucial importance for all direct detection experiments to suppress signals from radioactivity, which would hide or mimic the WIMP signal. In all experiments passive suppression is achieved via a low background setup and a deep underground site. The residual radioactive background represents the main limitation to the sensitivity of experiments, therefore dramatic improvements are achieved if the detector itself is able to distinguish between radioactive background and a nuclear recoil signal from WIMPs in the absorber.

In this chapter a characterization of the setup in Gran Sasso and an overview of the detector module developed for the second phase of the CRESST experiment are presented.

2.1   Sources of background

Rare event searches are limited by radioactive background signals due to cosmic rays, natural or induced radioactivity. In carefully constructed low background experiments, materials used for detectors are the dominant source of background; therefore careful selection of materials is mandatory.
Cosmic radiation at sea level is composed of about 70% muons, nearly 30% electrons and less than 1% of protons and neutrons. Muons represent the most penetrating component and they can contribute to the detector background in different ways: by depositing energy in traversing the detector itself; by producing energetic electrons, which induce secondary electrons and gamma radiation; by interactions with materials surrounding the detector followed by X, γ and neutrons emission. Furthermore spallation processes induced by muons make

radioactive nuclei both directly and via the produced neutrons.

Besides these cosmogenic radionuclides the main contribution to environmental radioactivity is due to primordial radionuclides and to radioisotopes man-made in the last decades.

2.2   The experimental setup

The shielding of experiments against cosmic radiation is achieved by installing the setup in a deep underground site. The CRESST facility is located in Hall A of the Laboratori Nazionali del Gran Sasso in Italy in a very low background environment.

Figure 2.1: Planimetry of LNGS underground laboratories.

The laboratory is situated in the highway tunnel of the Gran Sasso mountain at an average depth of about $3500\,\mathrm{m.w.e.}$[1] with a minimum rock overburden of $1400\,\mathrm{m}$ ($\sim 3150\,\mathrm{m.w.e.}$); this reduces the cosmic muon flux by 6 orders of magnitude to about $1\,\mathrm{m}^{-2}{\cdot}\mathrm{h}^{-1}$ (see figure 2.2).

2.2.1   Radioactivity at L.N.G.S.

The activity of samples of rock coming from the different laboratory halls has been measured and results are reported in table 2.1. The difference between various halls is due to the different local composition of the rock. The integral gamma flux calculated for all natural chains is $\sim 1\,\gamma{\cdot}\mathrm{cm}^{-2}{\cdot}\mathrm{s}^{-1}$ [Arp92].

A separate treatment is needed for ^{222}Rn that comes from ^{226}Ra α decay (^{238}U
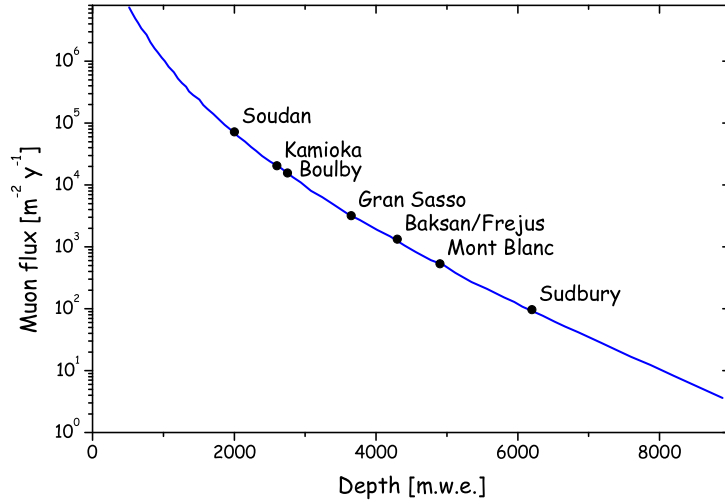
---

[1]Meter water equivalent.

Figure 2.2: The depth - intensity relation of cosmic ray muons. The circles indicate values for some underground laboratories. Figure adapted from [Kos92].

decay chain) which is widely present in rock and soil. The ^{222}Rn half life is long enough for this noble gas to degas from materials containing radium and diffuse through the rock and into the air and groundwater. The activity due to ^{222}Rn and its daughters is therefore strongly dependent on pressure and ventilation; with the present ventilation system the monitored value is between 10 and $20\,\mathrm{Bq\cdot m^{-3}}$ [Buc04].

Sample	γ activity [Bq·kg^{-1}]			
	^{232}Th	^{238}U	^{40}K	^{214}Bi
Hall A Rock	8.8±0.3	84.7±8.4	224±6	41.9±0.6
Hall B Rock	0.25±0.08	5.2±1.3	5.1±1.3	4.2±0.3
Hall C Rock	0.27±0.10	8.2±1.7	2.9±1.4	5.1±0.2

Table 2.1: Activity of samples of rock from different halls of Gran Sasso underground laboratory [Arp92].

In the case of WIMP search experiments particular attention must be devoted to neutrons since they scatter off nuclei in the absorber simulating the WIMP signal. Neutrons can originate from muon interactions in the last meters of rock or in the shielding material surrounding the experiment and from spontaneous fission or (α,n) reactions due to natural radioactivity of the rock or residual radioactivity of the shielding material. A simulation of the different

contributions and of the influence of different shielding materials has been performed. Conservative estimates of the recoil spectra induced by neutrons from different sources in CaWO$_4$ crystal are presented in figure 2.3 [Wul04b] [Wul04a]. It can be seen that, with a neutron moderator installed, the remaining neutron flux is dominated by neutrons induced by muons in the experimental setup. This background can be suppressed with a muon veto system.
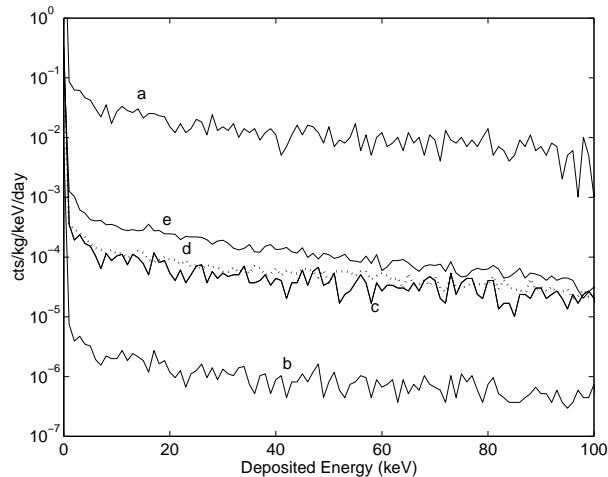

Figure 2.3: Simulated recoil spectra in a CaWO$_4$ detector in different scenarios: (a) low energy neutrons from the rock/concrete without neutron moderator; (b) low energy neutrons from the rock/concrete moderated by 50 cm of polyethylene; (c) low energy neutrons from fission reactions due to 1 ppb ^{238}U contamination in the lead shield; (d) high energy neutrons induced by muons in the rock; (e) high energy neutron induced by muons in the experimental setup. Figure from [Wul04a].

The neutron flux in the Gran Sasso Halls measured by various groups with different techniques is reported in table 2.2.

2.2.2   The cryostat

Since CRESST detectors operate at about 15 mK, the main part of the facility at L.N.G.S. is a cryostat whose design had to combine the requirements of low temperature with those of low background. To avoid any line of sight between detectors and non-radiopure materials, a design has been chosen in which a low background cold box housing the detectors is well separated from a commercial[2] dilution refrigerator. As can be seen in figure 2.4, the dilution unit of the cryostat and the dewars containing cryogenic liquids do not extend into the experimental volume.

---

[2]No special selection of materials for low radioactivity has been applied for the dilution unit.

Hall A		Hall C	
Energy interval (MeV)	Neutron flux ($10^{-6}\cdot$cm$^{-2}\cdot$s^{-1})	Energy interval (MeV)	Neutron flux ($10^{-6}\cdot$cm$^{-2}\cdot$s^{-1})
$< 50 \times 10^{-9}$	1.07 ± 0.05		
$50 \times 10^{-9} \div 10^{-3}$	1.99 ± 0.05		
$10^{-3} \div 2.5$	0.53 ± 0.008	$1 \div 2.5$	0.14 ± 0.12
$2.5 \div 5$	0.18 ± 0.04	$2.5 \div 5$	0.13 ± 0.04
$5 \div 10$	0.04 ± 0.01	$5 \div 10$	0.15 ± 0.04
$10 \div 15$	$(0.7 \pm 0.2)10^{-3}$	$10 \div 15$	$(0.4 \pm 0.4)10^{-3}$
$15 \div 20$	$(0.1 \pm 0.3)10^{-6}$		

Table 2.2: Neutron fluxes measured in the given energy intervals.
Hall A: BF$_3$ counters [Bel85].
Hall C: proton recoil scintillators [Arn99].

The low temperature of the dilution refrigerator is brought to the detectors via a 1.5 m long cold finger. A 20 cm thick lead shield (Plombum lead with a ^{210}Pb activity of 3.6 Bq$\cdot$kg^{-1}) inside a copper can, which transmits the cooling power, is placed between the mixing chamber and the cold finger. This shield, combined with another one at liquid nitrogen temperature surrounding the cold finger, serves to block radiation coming from the dilution refrigerator into the experimental volume.

The cold box consists of five concentric radiation shields which surround the experimental volume and the cold finger: a room temperature vacuum can; a first shield thermally anchored to the liquid nitrogen dewar of the refrigerator; an inner vacuum can sunk at the temperature of the liquid helium dewar; two inner radiation shields at 600 mK and 80 mK. The cold finger and the shields are made of radiopure copper which has been electro-polished after machining to remove residual surface contaminations and to reduce the risk of recontamination. High purity lead is used for vacuum seals [Büh96].

To reduce the effect of external vibrations the cryostat hangs from a 20 cm thick wood plate which rests on air dampers. To reduce the effect of vibrations created inside the cryostat by boiling cryogenic liquids, the detectors in the cold box are mounted onto a spring loaded support plate hanging from the cold finger.

A three level building (figure 2.5) houses the whole setup. A two level Faraday cage which surrounds the experiment has been chosen large enough so that all work on the low-background components can be performed inside the cage. In order to provide clean conditions while mounting detectors the ground floor of the Faraday cage, which houses the cold box and the lower part of the cryostat,
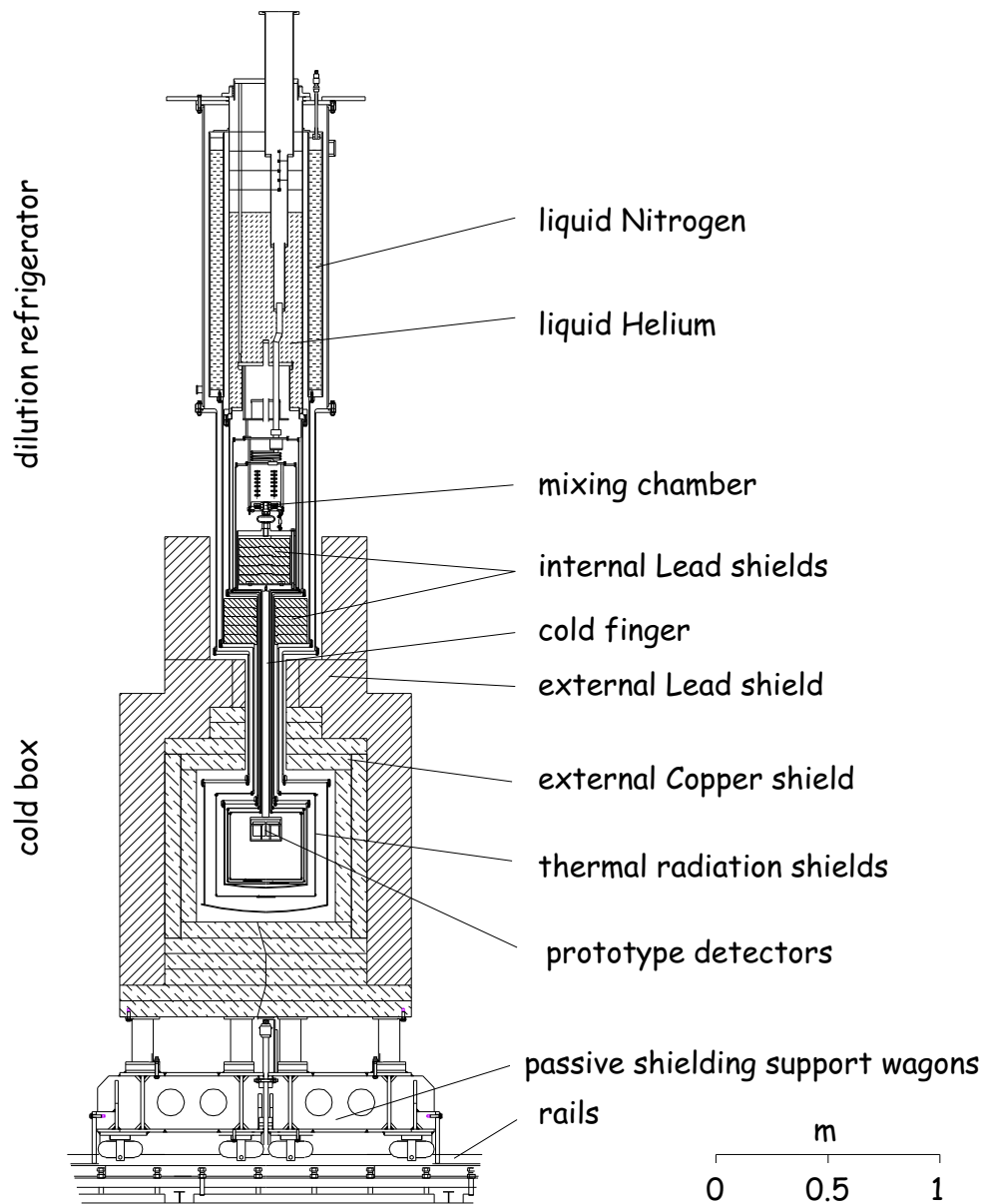
Figure 2.4: Schematic view of CRESST cryostat and passive shielding

is equipped as a class 100 clean room[3]. The upper level of the Faraday cage is outside the clean room and allows access to the top of the cryostat and to the electronics so that maintenance can be done without entering the clean environment. The gas handling and the pumping system of the cryostat, as well as the data acquisition system, are located outside the Faraday cage. On the third floor

---

[3]A class 100 clean room maintains less than one hundred particles larger than 0.5 microns in each cubic foot of air space.

there is a small chemistry laboratory and a laminar flow area where detectors are prepared before being mounted in the cryostat.
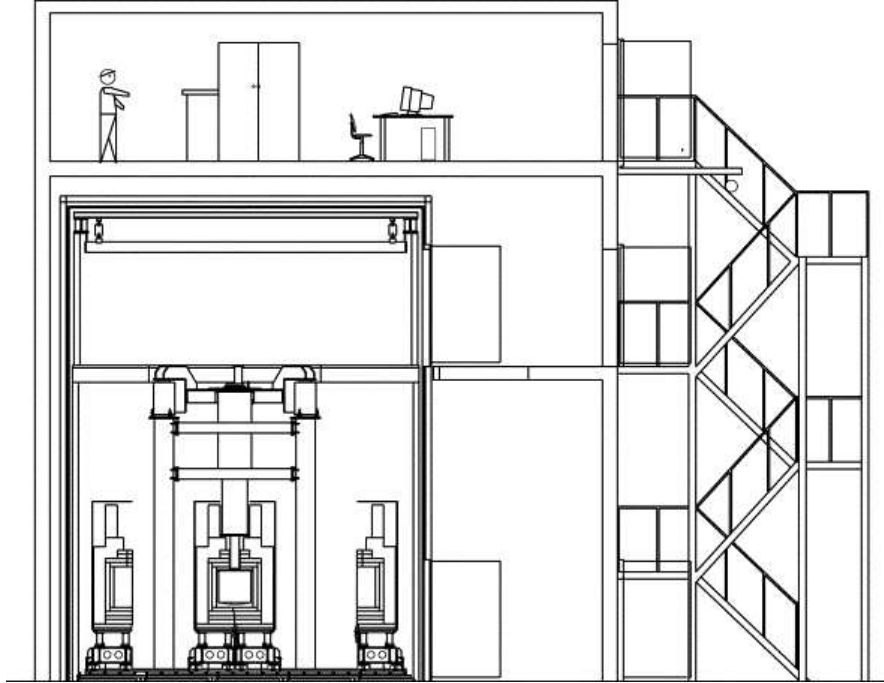

Figure 2.5: Cross section of CRESST building. The external passive shielding is shown in both its open and closed positions.

2.2.3 Shielding

The shielding against environmental radioactivity is achieved by means of high Z and high density materials like lead and radiopure materials like copper. The CRESST passive shielding is made of two closely fitting halves that can be opened without handling the individual pieces. It is composed of 14 cm of radiopure copper directly surrounding the cold box hosting the experimental volume, followed by 20 cm of Bolidean lead with a ^{210}Pb activity of 35 Bq·kg^{-1} [Büh96]. The entire shielding is enclosed in an air tight aluminium container (radon-box) which is constantly flushed with nitrogen gas and maintained at a slight overpressure in order to prevent radon from penetrating the shielding. In figure 2.5 the shielding surrounded by the radon-box is shown in both its open and closed position.

As already mentioned, for WIMP searches the suppression of neutron background is mandatory because their scattering off target nuclei[4] can mimic the WIMP

---

[4]Elastic scattering dominates at energies below 1 MeV. For higher energies the dominant effect is inelastic scattering that, besides producing a target nuclear recoil, would excite the nucleus inducing a de-excitation gamma emission.

signal [Wul04a]. A neutron moderator of 50 cm polyethylene, to be placed outside the radon-box, is currently in preparation. With the moderator installed the remaining neutron flux would be dominated by neutrons induced by muons in the lead of the shielding. Such a background will be suppressed by a muon veto system that will be installed inside the neutron moderator to complete the setup of the CRESST experiment.

No neutron shield was available for the measurements presented in this work.

2.3   CRESST Phase II

In its first phase the CRESST experiment used four sapphire crystals of 262 g each as detectors, equipped with tungsten superconducting phase transition thermometers. With this setup 100% trigger efficiency down to a threshold of 580 eV and a background of 0.73 counts/keV/kg/day throughout a dark matter run were achieved [Ang02]. In figure 2.6 and 2.7 exclusion plots for spin dependent and spin independent interaction derived from this run are shown. The extremely low threshold achieved in CRESST I allowed to explore the WIMP scattering cross section for WIMP masses down to 1 GeV.

The sensitivity of phase I was limited by the residual background in the detector which was of the order of 1 count/kg/keV/day in the energy range from 15 to 25 keV and about 0.3 counts/kg/keV/day at 100 keV. Significant improvements require the possibility to actively distinguish between radioactive background and a possible WIMP interaction in the absorber.

For its second phase the CRESST experiment is using scintillating crystals as absorbers. In such crystals a particle interaction mostly excites phonons, but a small fraction of the deposited energy is converted into scintillation light[5]. Nuclear recoils, which result from WIMP or neutron interaction, release less light than electron recoils resulting from α, β and γ interactions [Bir67]. By a simultaneous measurement of scintillation light and phonons it is therefore possible to discriminate nuclear recoils from radioactive background [GM89].

Other Dark Matter search experiments apply a discrimination technique based on the simultaneous detection of a phonon and a charge signal for silicon and germanium single crystal targets ([Abr02], [Ben01]). A major advantage of scintillators is the absence of signal degradation for events near the absorber surface found in ionization detectors, which may lead to misidentification of electron recoils as nuclear recoils.

The active background discrimination technique based on the simultaneous detection of a phonon and a light signal, allowing the rejection of the remaining background inside the shielding which is dominated by β and γ emissions from

---

[5]Typically for $CaWO_4$ only few percent of the deposited energy is converted into scintillation light, but the light yield depends critically on the crystal sample.
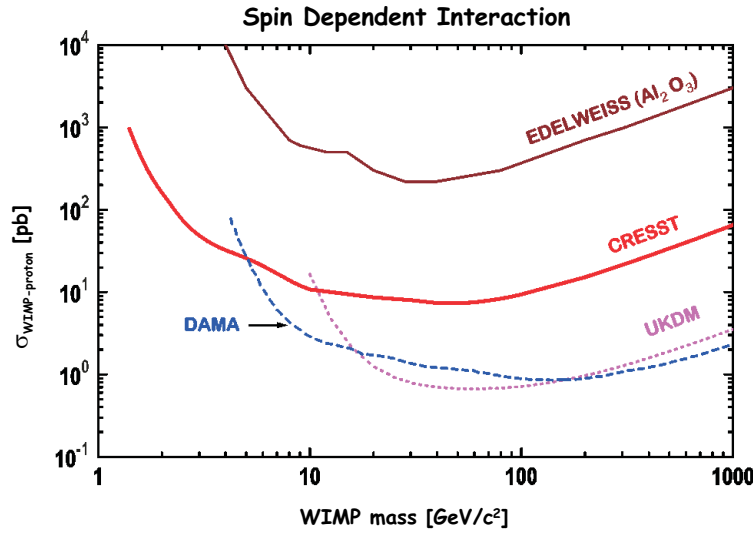
Figure 2.6: Equivalent WIMP-proton cross section limits (90% C.L.) for a spin-dependent interaction as a function of the WIMP mass from a 1.51 kg·day exposure of a 262 g sapphire detector. For comparison limits from EDELWEISS dark matter search with cryogenic sapphire detectors [Bel96] and from UKDM [Spo00] and DAMA [Ber96] with NaI detectors are shown.
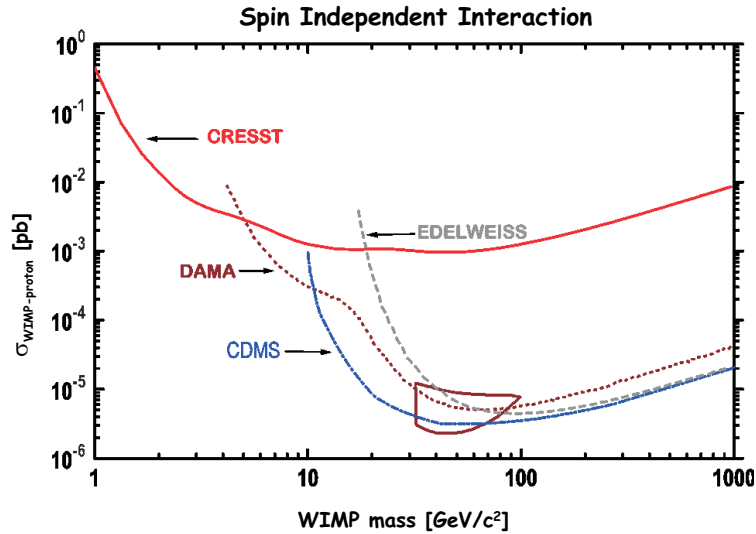
Figure 2.7: Equivalent WIMP-proton cross section limits (90% C.L.) for a spin-independent interaction as a function of the WIMP mass from a 1.51 kg·day exposure of a 262 g sapphire detector. For comparison limits are shown from CDMS with cryogenic detector and statistical subtraction of the neutron background [Abu00], from EDEL-WEISS with heat and ionization Ge detectors [Ben01] and from UKDM [Spo00] and DAMA [Ber96] with NaI detectors. The closed contour indicates the DAMA positive evidence at 3σ C.L. from the annual modulation [Ber00].

radioactive contaminants inside and in the surrounding of detectors, opens significant possibilities of improvement.

2.3.1 Background discrimination with combined light-phonon measurement

The active background discrimination technique can work with many different scintillating crystals[6] (BGO, BaF_2, $PbWO_4$, $CaWO_4$) whose light output has been studied at low temperature [Meu99].
$CaWO_4$ has been chosen because of its relatively high light yield at low temperatures and the absence of a noticeable degradation of the light yield for events near the crystal surface [Meu99]. In addition, the large atomic mass of tungsten (A_W=183.86) that enhances the WIMP-nucleus coherent interaction cross section makes $CaWO_4$ a very favourable target. The possibility to produce detectors with different scintillating absorbers is continuously under investigation due to the need of CRESST to identify a possible WIMP signal by comparing rates and spectra in different target materials (see section 1.3.1).

Proof of Principle

As mentioned before, the goal of the second phase of the CRESST experiment is to improve the sensitivity for WIMP direct detection by active background discrimination using a scintillating crystal as absorber. To test the applicability of such a technique a first proof-of-principle detector with $CaWO_4$ as scintillating absorber was developed [Meu99]. In this detector a 6 g $CaWO_4$ crystal (phonon detector) was operated as a calorimeter in close vicinity to a second much smaller calorimeter used to detect the scintillation light (light detector), both read out by tungsten superconducting phase transition thermometers. The result of this experiment is shown in figure 2.8. The signal in the phonon detector measures the total energy deposited in the $CaWO_4$ absorber, almost independently from the nature of the interaction[7], whereas the light output of the scintillating crystal associated with electron recoils is significantly higher than the one associated with nuclear recoils. This property is quantitatively expressed by the quenching factor that is defined as the ratio of the light yield from an electron recoil to the light yield of a nuclear recoil of the same energy. A quenching factor of 7.4 has been measured for nuclear recoils caused by neutrons while 3.6 was obtained for α particles.

---

[6]The discrimination based on the simultaneous detection of a phonon and a charge signal restricts possible targets to semiconducting materials.

[7]As mentioned, only a small amount of the deposited energy is converted into scintillation light.
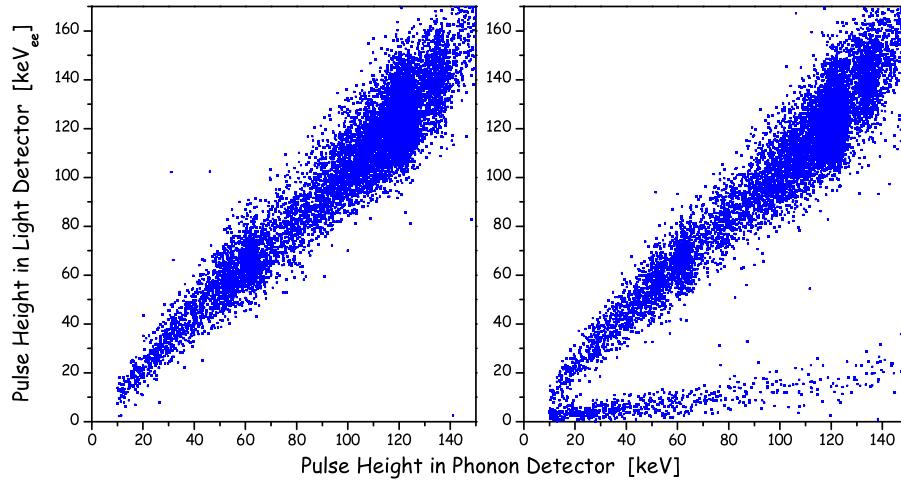
Figure 2.8: Scatter plot of the pulse height in the light detector versus the pulse height in the phonon detector for the proof-of-principle module [Meu99]. A quenching factor of 7.4 for the light output of nuclear recoils caused by neutron interactions with respect to electron recoils has been measured by irradiating the crystal with photons from a ^{57}Co source together with ^{90}Sr β source (left plot) and then adding an Am-Be neutron source (right plot).

Analogous experiments have been recently performed with different scintillating crystals to be used as additional absorber materials in the CRESST experiment [Ang04].

2.3.2 The detector module

Starting from the 6 g proof-of-principle device, the development of 300 g prototype modules as building blocks of a segmented 10 kg detector planned for CRESST phase II has been started in [Fra02]. The schematic view of a module for coincident phonon and light measurement is shown in figure 2.9.

The big challenge of this detector concept is the small amount of light that has to be measured which requires an extremely sensitive light detector. The aim of this work was to optimize the performance of light detection for the second phase of CRESST.

Phonon detectors

Phonon detectors developed for the second phase of the CRESST experiment consist of a 300 g cylindrical $CaWO_4$ crystal with 40 mm diameter and height read out by a tungsten superconducting phase transition thermometer.
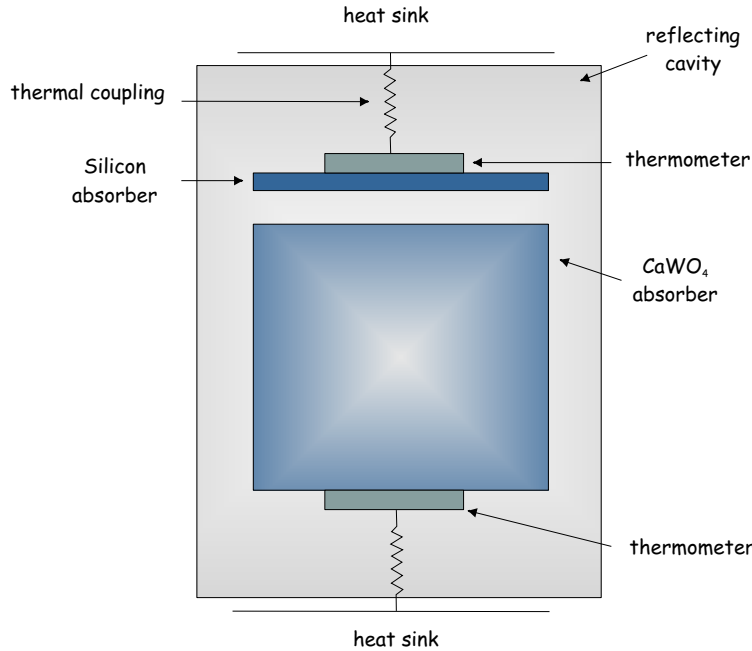
Figure 2.9: Schematic view of a prototype module for coincident light and phonon measurement.

$CaWO_4$ is known as a scintillator, although not widely used for standard applications because of its slow light response that is in the range of hundreds of microseconds at low temperatures [Bla83] (see figure 2.10).

Directed to the CRESST application, scintillation properties of $CaWO_4$ crystals have been thoroughly investigated at room temperature using a standard photomultiplier setup [Nin05].
Light yield and energy resolution have been observed to strongly depend on the crystal sample and to be affected by the crystal processing with a decrease in light yield up to 50% after sensor deposition. An important improvement of energy resolution and light yield has been achieved by roughening the crystal surface facing the light detector [8] to a roughness of about 10μm. This reduces the influence of the internal total reflection typically observed in crystals with high index of refraction ($n_{CaWO_4} = 1.92$) and facilitates the escape of the scintillation light from the crystal.

Light detectors

The detection of the light emitted by the scintillating absorber is obtained by using cryogenic light detectors which consist of a non-transparent absorber for
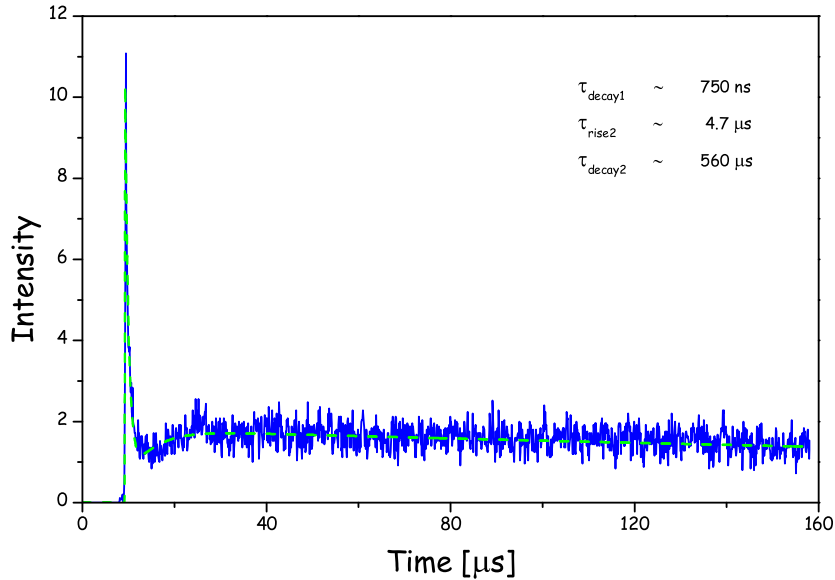
_____
[8]Photomultiplier or cryogenic light detector.

Figure 2.10: Light emission curve of CaWO$_4$ measured at 4 K using a time-of-flight mass spectrometer setup [Nin05].

the scintillation light, equipped with a tungsten superconducting phase transition thermometer.

The choice of cryogenic calorimeters for the detection of light was motivated by the extreme sensitivity achievable with this devices. Furthermore none of the more common photo detectors (photomultipliers, photodiodes) can work at the very low temperatures (few mK) required for operating the phonon detectors.

During the prototyping phase of CRESST II, the light detector absorbers consisted of a $(30 \times 30 \times 0.45)$mm^3 n-type silicon wafer with 200 Å SiO$_2$ layer on both surfaces.

The quenching factor experiment

An important property of scintillators, which is central for the technique of active background discrimination is the quenching factor mentioned. The quenching factor for nuclear recoils caused by neutrons, which for kinematic reasons are mostly oxygen and calcium recoils[9], has been determined to be 7.4 by the proof-of-principle experiment that was described before.

To further exploit the active discrimination technique in order to distinguish between neutron interactions, mainly causing oxygen and calcium recoils, and

---

[9]The energy of the recoiling nucleus is given by $E_r \approx \frac{4AE_n}{(A+1)^2} \cos^2 \theta$, where A is the nucleus mass number, E_n is the energy of the incident neutron and θ is the recoil angle in the laboratory coordinate system, assuming the target nucleus at rest.

WIMP interactions that mainly scatter off tungsten nuclei due to the A^2 scaling of the WIMP-nucleus scalar cross section, a detailed study of the quenching factor for different recoiling nuclei has been started.

Using a time-of-flight mass spectrometer setup the quenching factor for different recoiling nuclei has been measured at room temperature [Nin04b], showing a strong dependence of the light yield on the mass of the nucleus, as shown in figure 2.11.
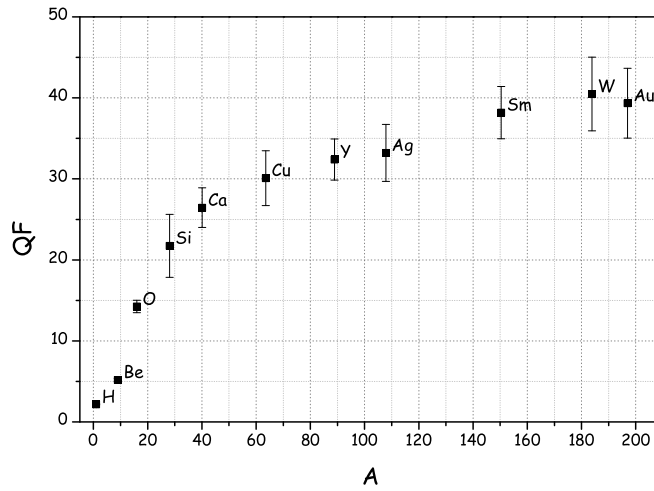

Figure 2.11: Measured quenching factor for 18 keV nuclear recoils of different atomic species. Tungsten recoils, expected from a WIMP interaction in the $CaWO_4$ absorber, show a quenching factor of about 40.

The technique is based on the measurement of the light produced by different ions impinging on the crystal. Ions were produced with a Laser Desorption/Ionization source (LDI), selected with a time-of-flight mass spectrometer and the light produced in the $CaWO_4$ target by the impinging ions was detected with a commercial photomultiplier. The main advantage of such a technique over a neutron scattering experiment comes from the possibility to choose different recoiling nuclei and to adjust their recoil energy.
Measurements at low temperature are currently in progress and seem to confirm the result.

Holder

The detector holder represents the innermost layer of the CRESST setup, therefore high radiopurity standards have been pursued. NOSV copper (a special heat leak free[10] copper) is used for the support structure which consists of two copper

---

[10]Materials with large electronic or nuclear heat capacities and with low thermal conductivity may store energy which is frozen in at higher temperatures and release it as heat over long

rings and three copper rods to hold the scintillating crystal and two end-caps in one of which the light detector is housed. A schematic view of the holder is shown in figure 2.13 and an open detector module can be seen in figure 2.15. During operation detector holders are thermally linked via the cold finger to the mixing chamber of the cryostat.

To avoid soldering[11] screwed electrical connections have been optimized in order to give a reliable contact at low temperatures. To connect detectors to the read-out circuit superconducting wires are screwed onto electrically insulated copper pads on the holder and from these pads $25\,\mu$m diameter aluminium bond wires[12] lead into the inner part of the holder and contact the thermometers as shown in figure 2.12.
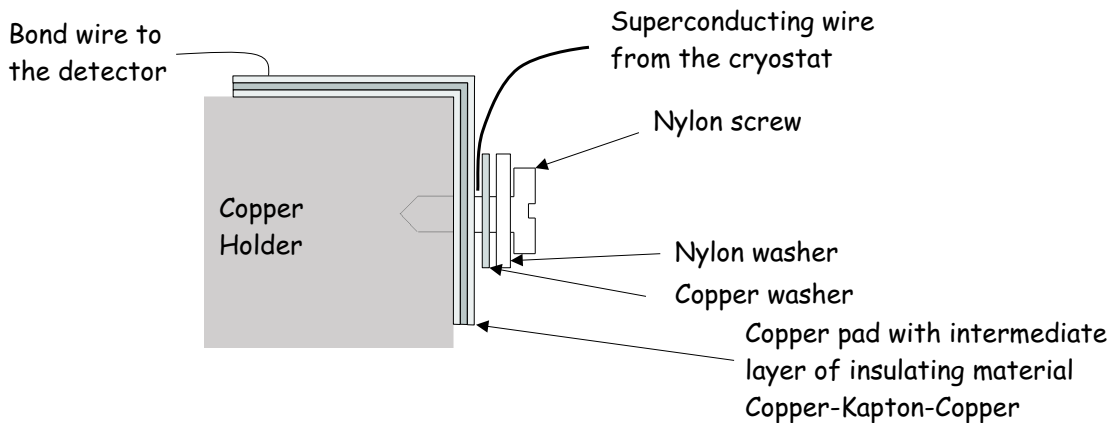

Figure 2.12: Schematic view of screwed electrical connections. For reliable contacts at low temperatures a careful choice of materials taking into account the effect of thermal shrinkage is important.

The mounting of crystals at milli-Kelvin temperatures deserves special attention. The contact area between crystal and holder has to be kept as small as possible to prevent parasitic thermalization of non-thermal phonons. On the other hand the crystal has to be tightly fixed to minimize the effect of vibrations. During the first prototyping phase of CRESST II, $CaWO_4$ crystals were initially held by Teflon ramps, touching the crystal at its edges, specially designed to provide thermal shrinkage compensation [Fra02]. In a number of short runs performed to optimize detectors, spurious pulses in the phonon detector without any associated light (dark events), unexplainable with known background, were observed. In order to investigate any possible correlation with stress in the crystal

---

periods of time.

[11] The presence of lead in soldering alloys, potentially introducing radioactive contaminants in the setup, requires to avoid soldering in the vicinity of detectors.

[12] Aluminium has a superconducting transition at $1.18\,$K, therefore its thermal conductance at operating temperatures is negligible.
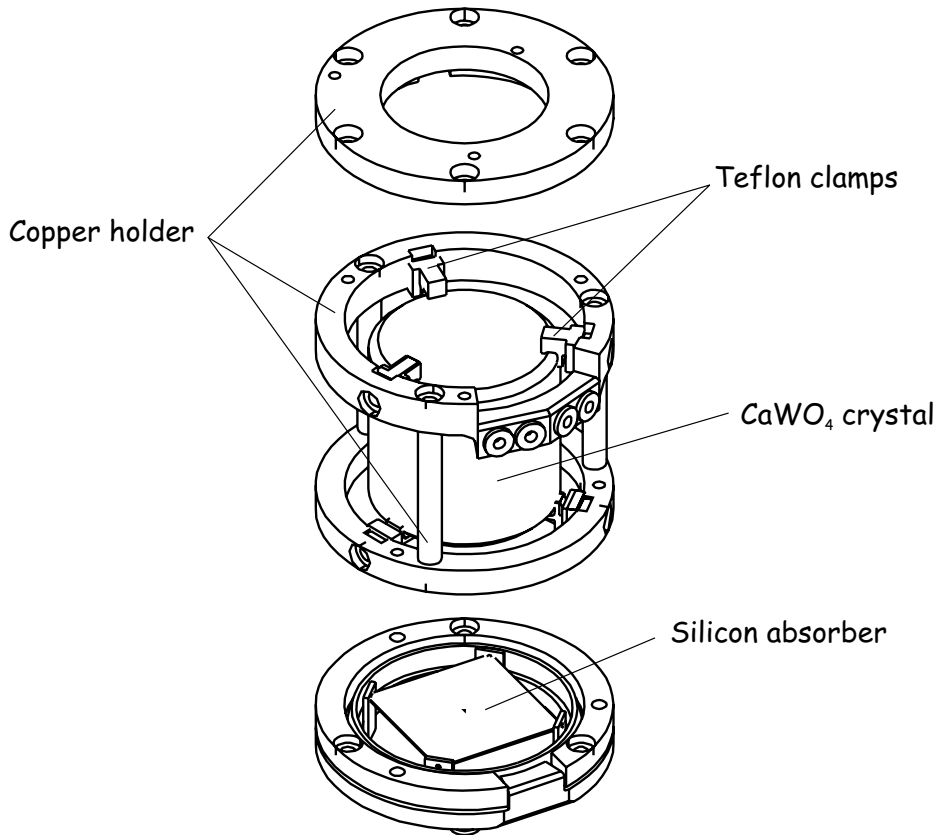
Figure 2.13: Exploded view of a detector module with main parts indicated. The reflector is not shown.

generated by the holding system, the ramps were replaced by Teflon clamps to achieve a tight holding and avoid at the same time a too small contact area that may result in an excessive pressure on the crystal edge. In the second prototyping phase, devoted to study the origin of dark events, Teflon parts touching crystals have been replaced with silver coated Cu-Be clamps that guarantee elasticity at low temperature. As a consequence of this modification dark events disappeared and, despite the relatively large contact area between crystals and a metal entailed by this new holding system, no noticeable loss of sensitivity of the phonon channel has been observed. The holding system by Cu-Be clamps (figure 2.14) will be adopted in the final holder design for CRESST phase II detector modules.

During most of the prototyping phase of CRESST II detectors, the square light detector absorbers were held on the copper holder by four thin Teflon tongues, each corner of the wafer resting in a small hole in the Teflon. This solution ensures a small contact area and a fully exposed surface of the detector. To minimize the presence of Teflon in the surroundings of detectors, a solution using aluminium coated Cu-Be clamps has been tested and will be used in the second phase of CRESST to hold circular light detectors (see figure 5.1).
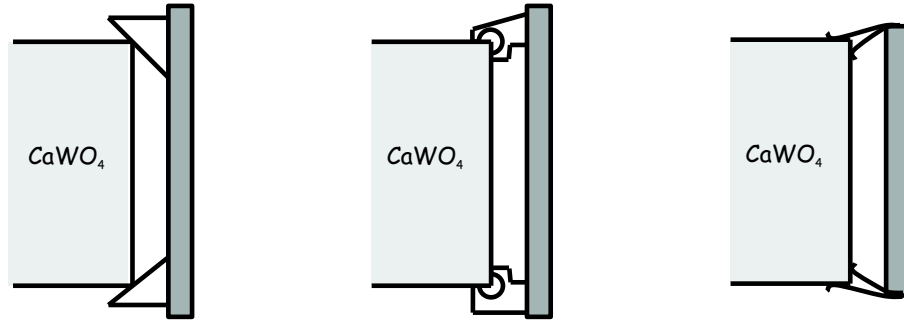
Figure 2.14: Schematic view of different $CaWO_4$ mounting in the holder tested in the prototyping phase for CRESST II. From left to right: Teflon ramps designed to achieve thermal shrinkage compensation; Teflon clamps adopted to reduce the pressure on the crystal edge; Cu-Be clamps chosen for the final design.

Light collection

The scintillation light escaping from the crystal must be absorbed in the light detector. The solution adopted by CRESST has both calorimeters inside a reflector that leads, as mentioned, to a fully exposed light detector. Due to the unfavourable ratio of areas between the light detector and the reflecting surface of the holder, an average photon has to undergo many reflections before hitting the light detector. Therefore the use of a reflector with a high overall reflectivity is mandatory. The reflecting housing is made of a polymeric multilayer foil with a reflectivity above 98% for wavelengths in the range 400-1000 nm[13] for all incident angles and polarizations [Web00]. The holder is assembled to have the transparent Polyethylenenaphthalate (PEN) support layer of the reflecting foil facing the detectors. This solution harnesses the PEN scintillation properties[14] to identify background due to alpha decays of nuclei implanted on the crystal or reflector surface[15], from which the daughter nucleus reaches the detector while the α is absorbed in the foil. These events would represent a potentially dangerous background because the energy of the daughter nucleus of the alpha decay would be detected in the phonon detector together with the light signal typical for the recoil of a heavy nucleus, consequently mimic a WIMP signal. Due to the presence of the scintillating layer, the absorption of the α particle in the foil makes a further production of scintillation light. The additional scintillation light from the α particles absorbed in the scintillating foil should allow clear

---

[13]The spectrum of the scintillation light of $CaWO_4$ at 20 K peaks at about 420 nm [Kee02].

[14]The luminescence properties of the PEN layer have been tested and the reflectivity spectra of both the scintillating and non scintillating side of the polymeric foil have been measured [Nin05].

[15]The deposition of dust particles, and consequently of radon daughters, is favored on materials that have electrostatic charged surfaces, as usually happens in the case of plastic and glass.

identification of these events as background.

During the second prototyping phase of CRESST II, in order to study the recoil background, a silver reflector (reflectivity above 95% for wavelengths above 400 nm with a sharp cutoff at 350 nm) has been tested. The use of this reflector led to a noticeable worsening of the light detector resolution at low energies implying a worsening of the discrimination threshold. Therefore the material has not been further employed.

Parts of the holder that extend inside the reflector are made of Teflon or coated Cu-Be to be as reflective as possible. The interface between the cylindrical reflector around the crystal and the reflector covering the end-caps is provided by overlapping Teflon rings that allow only the two small gaps needed to provide the access for electrical connections.

Simulations of the holder [Fra02] with polymeric multilayer foil as reflector indicate that the efficiency of the holder is almost independent of the position.

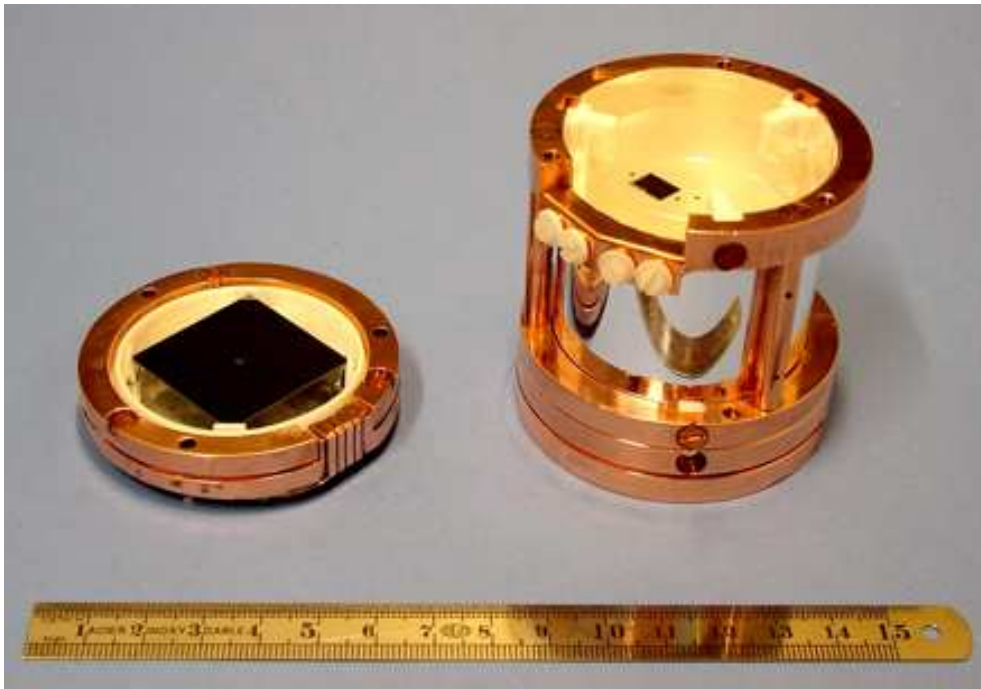Figure 2.15: Picture of an open detector module for CRESST phase II

The final goal of a 300 g module with a discrimination of better than 99.7% down to energies of 15 keV stated in the proposal for CRESST phase II [Alt01] has been completely fulfilled with prototype detectors that have been running in Gran Sasso. Analogous modules will therefore be used for the second phase of the CRESST experiment.

Chapter 3

Cryogenic detectors

The use of cryogenic detectors in WIMP searches has the advantage of having low energy threshold, excellent energy resolution and the ability to measure the full energy deposited by a particle interaction, independent of the interaction mechanism[1]. This combination makes them unique for the detection of nuclear recoils that would result from a WIMP interaction.

In this chapter the general detection principle of low temperature detectors is presented with a detailed description of detectors developed for the CRESST experiment.

3.1 Detector Principle

3.1.1 Basic model

A thermal detector consists of an absorber and a temperature sensor in thermal contact, weakly linked to a heat bath. Modelling the detector as an absorber characterized by its heat capacity C, in an extremely simplified calorimetric model an energy deposition in the absorber ΔE leads to a temperature rise of the detector given by

$$\Delta T = \frac{\Delta E}{C},\tag{3.1}$$

which then relaxes back to its equilibrium value via the thermal coupling to the heat bath. The temperature rise is therefore a direct measurement of the deposited energy.

In dielectric and semiconductor materials the heat capacity at low temperatures is dominated by the phonon system in which $C \propto (T/\Theta_D)^3$, where Θ_D is the Debye temperature. At millikelvin temperatures, due to the T^3 dependence of

---

[1]Conventional detectors that measure ionization or scintillation show a significant quenching for nuclear recoil events with respect to electron recoil events of the same energy.

the heat capacity, the energy deposition following a particle interaction results in a measurable temperature rise.

3.1.2 Thermometer

The temperature sensors developed for CRESST are tungsten superconducting phase transition thermometers (SPT) consisting of tungsten thin films evaporated onto one surface of the absorbers (typically the film thickness varies in the range 1-2 kÅ). The SPT are stabilized in the transition from the normal conducting to the superconducting phase where a small temperature rise leads to a relatively large increase in resistance, making them extremely sensitive thermometers.

Typical transitions (see figure 3.1) have a width of the order of $1\,mK$ [2]. Bulk tungsten has a superconducting transition at $15\,mK$ but transition temperatures of thin films on $CaWO_4$ crystals around $50\,mK$ were obtained in a first stage, probably due to a solid state reaction between the thin film and the substrate at the high temperatures (about 500°C) that are achieved during the evaporation process. With the introduction of a SiO_2 buffer layer to prevent diffusion between the film and the crystal, transition temperatures as low as $7\,mK$ have been obtained. Similarly, using silicon oxide as interdiffusion barrier, superconducting transitions of tungsten films on silicon with critical temperature of the order of $10\,mK$ have been obtained.

The width of the transition curve defines the dynamical range while its slope determines the sensitivity[3] of the thermometer, thus characterizing the performance of the individual detector.

During the prototyping stage for the second phase of the CRESST experiment different thermometer geometries have been tested to optimize the detector response.

Heater and Thermal Coupling

Besides the tungsten superconducting film, additional structures are needed for the detector operation.

Thermometers are stabilized at the operating point within a few μK by a heater, consisting of a normal conducting structure coupled to the tungsten film. The same heater is also used to inject periodic heater pulses to monitor the detector stability. A second normal conducting structure is used to link the sensor to the heat bath.

Different solutions have been adopted to realize heater and thermal coupling for

---

[2]A significant variation of transition shape is observed when the measurement is carried out with high currents that introduce non negligible self heating and critical current effects.

[3]The sensitivity of a specific detector can be increased using a high read-out current.
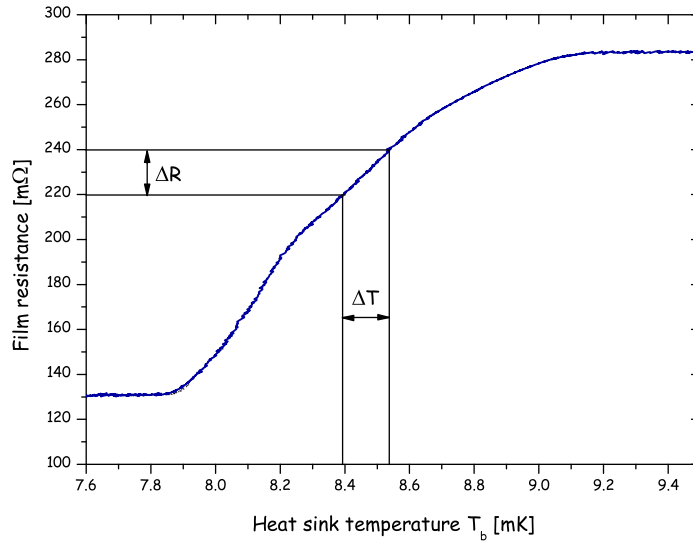
Figure 3.1: Typical measured transition curve of a tungsten film. The normal conducting resistance of the film depends on its geometry.

the two detectors forming the detector module developed for the second phase of the CRESST experiment

In the phonon detector the heater consists of a $25\,\mu$m diameter gold wire bonded from two small aluminium pads on the side of the thermometer onto a gold pad in the center of the SPT as shown in figure 3.2. The thermal coupling is also realized via a gold wire connecting the central gold pad to the detector holder.

In the light detector, the heater and the thermal coupling to the heat sink have been realized with gold film structures whose characteristics will be explained in detail in a following chapter.

3.1.3 Readout

The circuit used to bias and read out the thermometer is shown in figure 3.3. A constant bias current I_0, supplied by a floating current source, is shared between the branch containing the temperature dependent resistance of the film $R_f(T)$ and the branch containing the constant reference resistor (shunt) R_s[4] in series with the input coil of the dc SQUID [5].

---

[4]Reference resistors of $50\,$mΩ have been used during the prototyping phase of CRESST II.

[5]A dc Superconducting QUantum Interference Device consists of two Josephson junctions connected in parallel on a superconducting loop and is so named because it operates with a steady current bias [RI78].
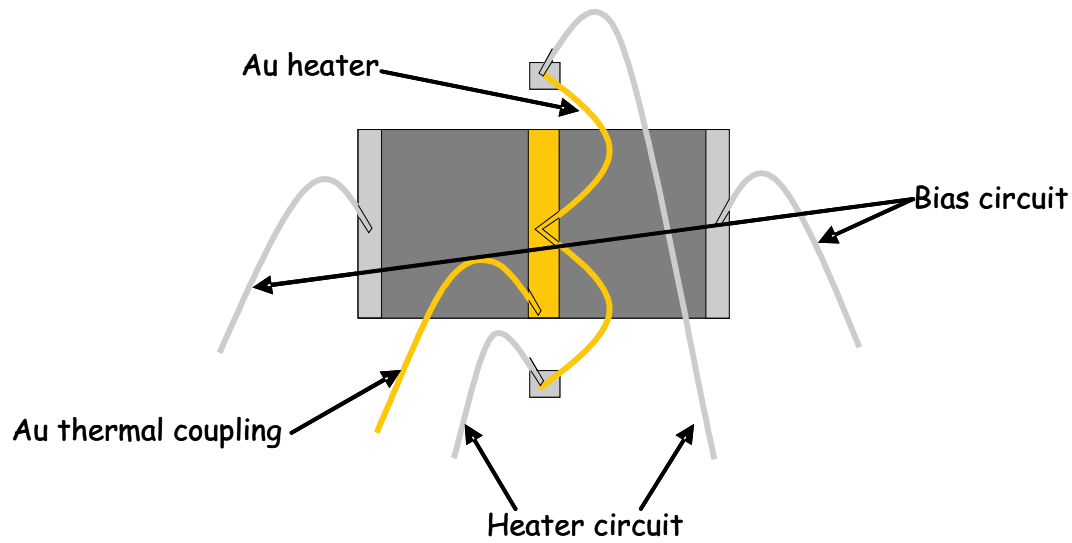
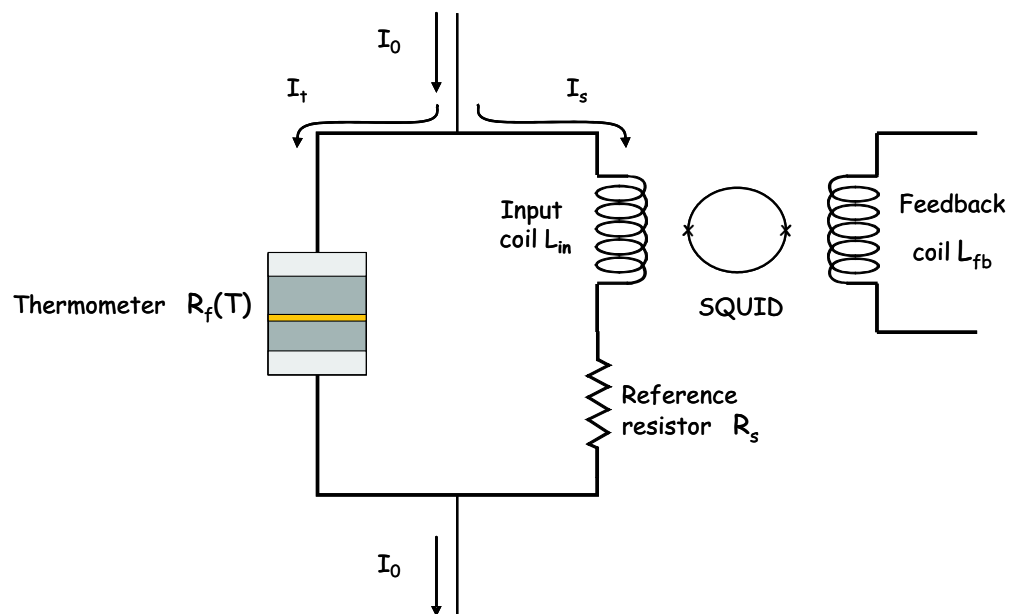Figure 3.2: Layout and connection scheme of a SPT realized on a CaWO$_4$ crystal.

Figure 3.3: Schematic view of the readout circuit.

The current through the SQUID branch is given by:

$$I_s = I_0 \frac{R_f(T)}{R_f(T) + R_s}. \tag{3.2}$$

Any change in the film resistance causes a change in the branching of the bias

current I_0. The increase of the current I_s, that results from an increase of the resistance of the film following an energy deposition, causes a change in the magnetic flux coupled to the SQUID via the input coil.

A SQUID is essentially a flux to voltage transducer, providing an output voltage that is periodic in the applied magnetic flux Φ with the period of one flux quantum $\phi_0 \equiv h/2e \approx 2 \times 10^{-15} \, Wb$ [Cla89]. To overcome the ambiguity due to the periodicity of the response, SQUIDs are operated in flux locked mode (i.e. as null detectors) with a separate feedback coil used to keep the flux through the loop constant. The output voltage of the SQUID electronics is then proportional to the feedback current.

In flux locked mode there is a linear relation between the applied magnetic flux, defined by the current flowing through the input coil I_s, and the output voltage given by:

$$V_{out} = \xi(\Phi + n\phi_0) \tag{3.3}$$

where ξ is the flux to voltage transfer coefficient of the SQUID system. This technique enables the measurement of changes in flux ranging from much less that a single flux quantum to many flux quanta. However the flux locked mode is affected by the existence of a sequence of stable points, originating from the periodicity of the flux-voltage characteristics of the SQUID. As a consequence, this readout scheme is limited by the maximum rate of flux change that the feedback electronics can compensate (slew rate). Signals exceeding the slew rate can cause an offset by a factor $\xi n\phi_0$ in the readout voltage (i.e. a flux quantum loss) and lead to a different base line of the SQUID after the event (different value of n in equation 3.3).

The advantage of using SQUIDs for detector readout, besides their extreme sensitivity, comes from the purely inductive input impedance of the superconductive input coil which matches the small impedance of the biasing circuit.

SQUIDs used for the CRESST experiment are commercially available dc SQUIDs mounted in the liquid helium dewar of the cryostat and connected to detectors via twisted pairs of superconducting wires.

3.1.4   Noise sources

The performance of a detector in terms of threshold and resolution is ultimately limited by the influence of the noise whose contributions originate from the detector itself[6], from the readout system and from the environment in which detectors are operated.

---

[6]An extensive discussion of noise sources affecting calorimeters and bolometers can be found in [Mat82], [Mos84] and [Gal03].

Phonon noise

Spontaneous random energy flow into and out of the thermometer, produced by the random propagation of the energy carriers through the thermal link to the heat bath, occurs at all times leading to a fluctuation of the energy content of the calorimeter. This phonon noise determines the ultimate physical limit for the achievable energy resolution because it represents a constant background noise against which the energy deposition caused by an event must be measured. Classical statistical mechanics gives a result for the amplitude of these fluctuations [McC93] as:

$$\langle \Delta E^2 \rangle = k_B T^2 C \tag{3.4}$$

where T is the temperature of the heat bath and C is the heat capacity of the sensor at the temperature T. Due to the fact that the measured signal in CRESST detectors is a temperature excursion, whose dependence is given in equation 3.1, the contribution of phonon noise to the measured signal shows a $1/\sqrt{C}$ dependence that makes it relevant for sensors with a small heat capacity.

Johnson noise

The white Johnson noise of resistors[7] in the readout circuit of figure 3.3 receives contributions from the thermometer film and from the shunt resistor. In a readout circuit with a $100\,\mathrm{m\Omega}$ film resistor and $50\,\mathrm{m\Omega}$ reference resistor, both at a temperature of $10\,\mathrm{mK}$, the equivalent current due to Johnson noise is about $2\,\mathrm{pA}/\sqrt{\mathrm{Hz}}$.

SQUID noise

Josephson junctions of dc SQUIDs have thin film shunt resistors in parallel. Their Johnson noise current affects the performances of the device by generating a white flux noise in the SQUID loop. The dc SQUIDs used for the CRESST experiment exhibit a flux noise level of the order of $1\,\mathrm{pA}/\sqrt{\mathrm{Hz}}$ that is of the same order of magnitude as the Johnson noise.

Other noise sources

External disturbances like temperature fluctuations of the heat bath or vibrations and electrical interferences that reach the detector can show up as noise in the detector response. These external noise sources can be suppressed by a careful design of the experimental setup.

---

[7]The spectral current density of Johnson noise is expressed as $4k_B T/R$, where T and R are respectively temperature and resistance of the resistor.

3.2 Detector model

The typical detector studied here consists of a dielectric absorber where the particle interaction takes place and a stripe of superconducting material evaporated onto one of its surface serving as a thermometer. The detector response to an energy deposition depends on the various processes occurring in the device. A detailed description of a theoretical model for the signal evolution in a low temperature calorimeter is given in [Prö95].

3.2.1 Heat capacities

Heat capacities of different parts of detectors play a fundamental role because they define the achievable temperature rise for a defined energy deposition.

Non-magnetic crystalline dielectrics have a heat capacity dominated by the lattice specific heat c_{ph}. At low temperatures it is described by the Debye model as:

$$c_{ph} = \frac{12\pi^4}{5} n_a k_B \left(\frac{T}{\Theta_D} \right)^3 = AT^3 \tag{3.5}$$

where Θ_D is the Debye temperature, n_a is the number of lattice atoms per mole and A is a constant of the material. The same cubic dependence of phonon specific heat with temperature characterizes pure semiconductors at low temperatures where conduction electrons are frozen out. Therefore the heat capacity of dielectrics and pure semiconductors at low temperatures is very small, making them suitable materials to be used as absorbers.

The temperature sensors used in CRESST are metal films in which, besides lattice vibrations, there are conduction electrons that can be thermally excited. Accordingly, it is necessary to add[8] to the lattice term c_{ph} of the specific heat the electronic contribution c_e that is given by [Pob92]:

$$c_e = \frac{\pi^2}{2} n_e k_B \frac{T}{T_F} = \gamma T \tag{3.6}$$

where T_F is the Fermi temperature, n_e is the number of conducting electrons per mole and γ is the Sommerfeld constant which depends on the material. The linear dependence of c_e makes it the dominant term of the heat capacity of a metal at low temperatures.

In the absence of an external magnetic field superconducting materials show a

---

[8]The specific heat due to lattice vibrations and to conduction electrons in a metal can be treated independently and then added as a consequence of the large mass difference of nuclei and electrons that allows, to a good approximation, an independent treatment of their motions (Born-Oppenheimer approximation).

	Tungsten	Gold	Aluminium
T_c [mK]	15	-	1180
T_F [K]	27000	63900	134900
Θ_D [K]	383	162	428
γ [mJ $\cdot$ mol^{-1} $\cdot$ K^{-2}]	1.01	0.729	1.356

Table 3.1: Transition temperature, Fermi temperature, Debye temperature and Sommerfeld constant for metals commonly used for CRESST sensors [Kit67] [Tri73].

second-order phase transition[9] at the critical temperature T_c. For simple superconductors the theory of superconductivity [Tin96] predicts a jump of the specific heat given by:

$$\Delta c = 1.43 \gamma T_c \tag{3.7}$$

where γT_c is the electronic specific heat of the normal conducting state at the critical temperature. To estimate the heat capacity in the region of the transition, namely at the operating point of a sensor, a linear approximation may be used. Taking the ratio of the resistance at the operating point R_{op} to the normal conducting resistance R_n as a measure for the fraction of the film in the superconducting phase, the heat capacity at the operating point can be expressed as:

$$c_{op} = c_e \left(2.43 - 1.43 \frac{R_{op}}{R_n} \right). \tag{3.8}$$

Below T_c the electronic specific heat has an exponential temperature dependence, vanishing more rapidly than the electronic specific heat in the normal conducting state of the metal, whereas the lattice contribution is not influenced by the transition to the superconducting state. For temperatures below $T_c/10$ the electronic contribution becomes negligible and the heat capacity is dominated by the lattice specific heat. Table 3.1 compiles the relevant values for metals commonly used in CRESST sensors.

3.2.2   Pulse formation

Any energy deposition in the absorber creates high frequency phonons. Ionizing radiation, that mainly releases its energy in the electron branch, first creates highly excited electrons which initially loose their energy by transfer to other electrons and by excitation of electron-hole pairs down to an energy of less than twice the energy gap in the material[10] and then relax within 10 ps to the band edge via

---

[9]A second-order phase transition has no latent heat at the transition and a jump in the specific heat.

[10]Once the energy of the excited electrons is lower than twice the energy gap in the absorber, the production of electron hole pairs is no longer possible.

the emission of optical phonons[11]. On a time scale of the order of 100 ps, optical phonons decay into acoustic phonons of about half the Debye frequency (Debye frequency ν_D for materials commonly used as absorbers in CRESST detectors are given in table 3.2), leading to an almost monoenergetic frequency distribution. The energy released in the nuclear branch (i.e. via elastic interactions with nuclei), that becomes important for alpha and heavy ions and is dominant for neutrons and WIMPs, excites instead non-thermal acoustic phonons in a broad frequency range via the local deformation of the crystal lattice.

After a time of the order of 100 ps the energy released in the absorber by a generic interaction is transferred into high frequency acoustic phonons, but with a phonon spectrum dependent on the original interaction. These phonon populations are not in equilibrium and start to decay towards a thermal distribution.

		Al_2O_3	Si	$CaWO_4$
Θ_D	[K]	1041	645	228
$\nu_D = k_B\Theta_D/h$	[THz]	≈ 21.7	≈ 13.5	≈ 4.7

Table 3.2: Debye Temperature and Debye frequency for materials commonly used for CRESST absorbers [Ash76], [Glu73]. The values given in the literature differ to some extent depending on the method used to derive them.

The down conversion of longitudinal acoustic phonons, that is induced by lattice anharmonicity, proceeds via three phonon processes with a decay rate $\Gamma_{decay} = \eta(\nu/\nu_D)^5$ where ν is the phonon frequency [Tam85a]. In this formulation the dominant dependence on the material is contained in the ratio (ν/ν_D) and the parameter η is similar for all materials. Transverse acoustic phonons occupy the lowest energetic branch and do not decay in ideal isotropic media; however, even in real anisotropic media, their decay rate can be neglected [Tam85b]. Besides the decay of longitudinal phonons, all phonons scatter on isotopes present in the crystal lattice with a rate $\Gamma_{isotope} \propto \nu^4$ [Mar90] and such an elastic scattering induces rapid mode conversions maintaining an occupation of modes according to the density of states, thus opening an effective decay channel for transverse phonons [Tam85a]. In silicon and sapphire only about 10% of the phonons are in the longitudinal mode, therefore the effective decay rate is only 10% of Γ_{decay}. Simulations of the time development of an initial monoenergetic phonon population of half the Debye frequency show that the strong frequency dependence of Γ_{decay} leads to a very rapid initial decrease of the average phonon frequency. After this time all differences in the phonon spectrum caused by energy releases in the nuclear or electronic branch are washed out. The first fast decay is followed by

---

[11]In the case of scintillating materials the emission of photons, however highly suppressed compared with the emission of phonons, is extremely important for the event discrimination.

a much slower rate of change (figure 3.4), consequently the average phonon frequency distribution stays almost constant for a few milliseconds[12] during which time phonons spread ballistically over the entire absorber filling it uniformly[13].
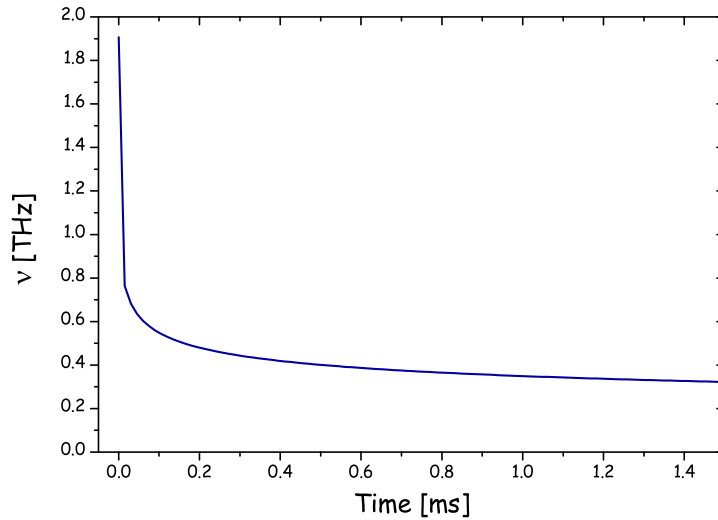

Figure 3.4: Time development of the average phonon frequency resulting from anharmonic decay of a 7.5 THz ($\approx \nu_D(Si)/2$)phonon population in silicon [Prö95].

3.2.3   Thermal coupling

After a few surface reflections non-thermal phonons are uniformly distributed in the absorber, consequently different parts of the detector will assume different temperatures. The temperature of the electron system of the thermometer determines its resistance and hence the measured signal. Its time dependence is determined by the couplings of the different thermal subsystem of the detector.

Kapitza coupling

The transmission probability of acoustic phonons through the boundary between two materials can be calculated within the theory of anisotropic elastic continua. A calculation of the energy flux per unit area and unit time across the boundary

------

[12]The phonon population does not thermalize in the absorber on such a time scale.

[13]A time of the order L/v, where L is the largest dimension of the absorber and v is the sound velocity in the medium averaged over directions and modes, is required to establish a uniform distribution.

Transmission from→ to	G_K [kW· K^{-1}· m^{-2}]	$\langle v_\perp \alpha \rangle$ [m/s]	$\bar{\eta}$
Si→ W	0.440	1485.4	0.246
Al$_2$O$_3$ → W	0.430	2547.5	0.290
CaWO$_4$ → W	1.784	647.9	0.142
Al$_2$O$_3$ → Si	0.495	2933	
Si→ Al$_2$O$_3$	0.495	1668.7	

Table 3.3: Kapitza conductance G_K, $\langle v_\perp \alpha \rangle$ and effective absorption $\bar{\eta}$ for typical absorber-thermometer interfaces of CRESST detectors. Parameters are calculated for the transmission of phonons across the (001) plane of silicon, the ($1\bar{1}02$) plane of sapphire and the (001) plane of CaWO$_4$; tungsten is considered polycrystalline [Prö95].

from material 1 to material 2 ($\dot{Q}_{1\to 2}$), performed by summing over all modes and wave vectors of incident phonons [Prö95], leads to

$$\dot{Q}_{1\to 2} = \left\langle \frac{E}{V} \right\rangle \frac{1}{2} \langle v_\perp \alpha \rangle, \qquad (3.9)$$

where $\langle E/V \rangle$ is the average energy density[14] in the first material, $v_\perp$ is the phonon group velocity normal to the interface, α is the transmission probability and $\langle ... \rangle$ denotes the average over modes and wave vectors of the incident phonons.

If E/V is the thermal energy density, from equation 3.9 the Kapitza boundary conductance G_K of thermal phonons between two materials can be derived as [Prö95]:

$$G_K = \frac{\dot{Q}_{1\to 2}(T + \Delta T) - \dot{Q}_{2\to 1}(T)}{\Delta T} = \frac{C}{2V} \langle v_\perp \alpha \rangle \propto T^3 \qquad (3.10)$$

where C/V is the heat capacity per unit volume of the first material. The cubic temperature dependence of the Kapitza coupling comes from the T^3 dependence of the phonon heat capacity.

Electron-phonon coupling

The electron-phonon coupling G_{ep} determines the thermal coupling of the absorber to the electrons of the thermometer. The frequency dependence of the electron-phonon interaction in normal conducting metals depends on the product $(q \cdot l_e)$, where q is the phonon wave vector and l_e is the mean free path of electrons.

---

[14]Wave vectors of thermal and non-thermal phonons have the same angular distribution because surface and isotope scattering distribute them according to the density of states. Therefore the same equation 3.9 can be used for the energy transmission of thermal or non-thermal phonons by using the appropriate energy density $\langle E/V \rangle$.

For thermal phonons, at low enough temperatures or in the limit where $(q \cdot l_e) \ll 1$ applies, it can be shown ([Liu91],[DiT92]) that the temperature dependence of the electron-phonon thermal coupling can be expressed as:

$$G_{ep} \propto T^5. \tag{3.11}$$

At higher temperatures or in the limit $(q \cdot l_e) \gg 1$ a fourth power temperature dependence is expected. These temperature dependencies lead to an effective thermal decoupling of the electron system from the phonon system of the thermometer and thus from the phonon system of the absorber[15]. In the operating temperature range of the CRESST experiment and for a typical thermal phonon mean free path, the dependence shown in equation 3.11 is expected.

For non-thermal phonons, where $(q \cdot l_e) \gg 1$ holds, longitudinal phonons efficiently interact with the electron system of the thermometer being absorbed in the metal film. For metals with an approximately spherical Fermi surface, the mean free path of longitudinal and transverse phonons due to inelastic scattering on electrons in the limit $(q \cdot l_e) \gg 1$ is given in the Pippard model [Pip55] by:

$$l_L \approx \frac{12 v_L^2}{C_L \nu}, \qquad l_T \approx \frac{v_T l_e}{C_T} \tag{3.12}$$

where v_L and v_T are speeds of sound respectively for longitudinal and transverse modes and C_L and C_T are material constants. The efficient interaction of longitudinal phonons with the electron system of the thermometer film is expressed by the frequency dependence of l_L.

Longitudinal phonons interact strongly with electrons because of the space charge associated with the density variation. Transverse phonons on the other hand involve no density changes and hence no space charge effects, therefore the interaction with electrons arises only from the magnetic field associated with the moving ions and is consequently much weaker [Har79].

From equation 3.12 it can be estimated[16] that non-thermal phonons are practically completely absorbed in $2\,\mathrm{k\mathring{A}}$ thick tungsten films whereas transverse phonons are not. In the extreme assumption of total absorption for transmitted longitudinal phonons and no interaction for transverse phonons, the average absorption probability in the film $\bar{\eta}$ can be calculated [Prö95]. Values of $\bar{\eta}$ of interest are listed in table 3.3.

Absorbed phonons thermalize in the thermometer and increase the temperature of its electron system. Due to the thermal decoupling of electrons and phonons, this leads to a significant overheating of the electrons in the thermometer with respect to the absorber. In such a situation the detector sensitivity is determined by the heat capacity of the thermometer film. The absorber material does

---

[15]The superconducting transition leads to a further weakening of the thermal coupling between electrons and phonons below the transition temperature.

[16]For tungsten at $0\,\mathrm{K}$ v_L=5248 m·s^{-1} and v_T=2908 m·s^{-1} [Sim71].

not affect the detector sensitivity through its heat capacity but by means of its phonon transport properties. Therefore the detector sensitivity shows a linear dependence on the velocity of sound in the absorber material (see equation 3.19).

Thermal coupling to the heat sink

As already mentioned, the thermal coupling of detectors to the heat sink is realized via structures of normal conducting metal, namely gold. The coupling strength defines the thermal relaxation time $\tau = C/G$ of the thermometer. For gold coupling structures the heat conductance G can be calculated from the residual electrical resistance at low temperature via the Wiedemann-Franz law:

$$G = \frac{LT}{R} \tag{3.13}$$

where R is the residual resistance at low temperature T and the Lorenz number L is a constant ($L = 2.45 \cdot 10^{-8}\, W \cdot \Omega \cdot K^{-2}$). For thermometers with a small heat capacity as in the case of light detectors, the thermal relaxation time achievable with the mentioned bond wire coupling can be too short, therefore a thin film gold structure solution has been adopted, which allows realization of a weak coupling G by an appropriate design of the structure.

3.2.4 Calorimeter model

Figure 3.5 is a schematic representation of a thermal model, where the detector consists of three weakly coupled thermal subsystems characterized by their heat capacity C and their temperature T. The phonon system of the absorber and of the thermometer are thermally coupled via the Kapitza coupling G_K; the phonon and the electron system of the thermometer are coupled by the electron-phonon coupling G_{ep}; finally the detector is coupled to the heat bath via the thermal link of the thermometer G_{eb} and directly via its mechanical mounting that can be modelled as a thermal conductance G_{ab}. Since the heat capacity of the phonon system of the thermometer at low temperature can be neglected (see equation 3.5), the Kapitza coupling between the two phonon systems G_K and the electron-phonon coupling G_{ep} are replaced in the model with:

$$G_{ea} = \left(\frac{1}{G_{ep}} + \frac{1}{G_K} \right)^{-1} \tag{3.14}$$

that represents a coupling between the electron system of the thermometer and the phonon system of the absorber.

As already mentioned, non-thermal phonons that enter the thermometer efficiently interact with the electron system of the thermometer that, due to this interaction, experiences a time dependent power input $P_e(t)$. The thermalization
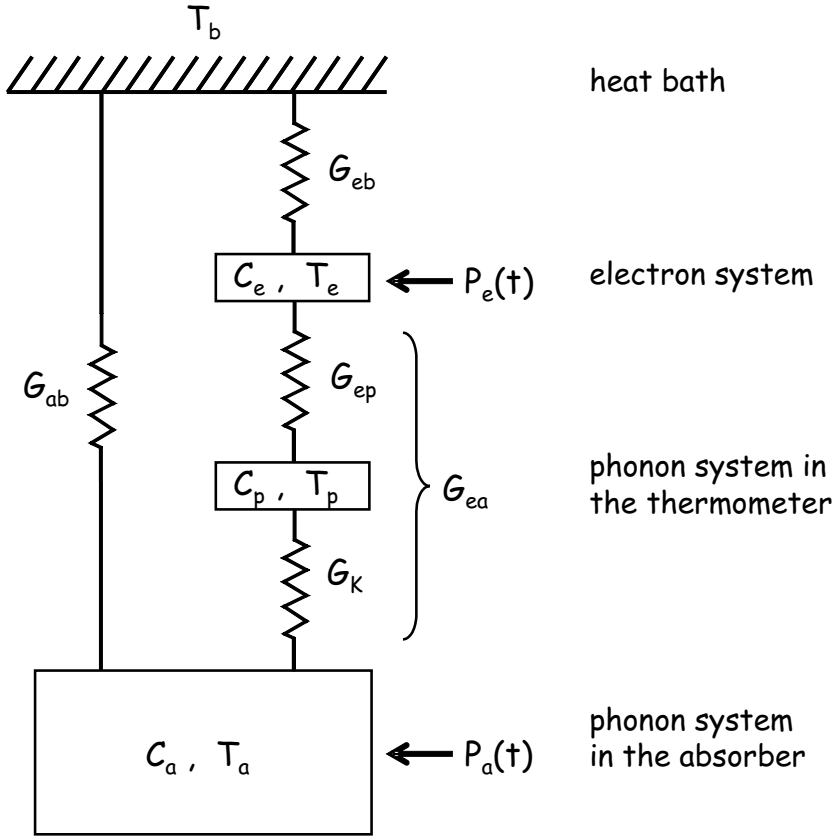
Figure 3.5: Schematic view of the thermal model of the calorimeter.

of high frequency phonons in the absorber is modelled by a direct power input $P_a(t)$ into the thermal phonon population.

To get a quantitative model, it is assumed that the energy ΔE deposited by an interaction creates high frequency phonons directly after the interaction (neglecting processes described in section 3.2.2) and that such high frequency phonons fill the volume of the absorber V_a with a uniform energy density $\Delta E/V_a$. Assuming that the thermalization rate of these phonons is independent of their frequency, the time dependent power inputs can be described as:

$$P_e(t) = P_0 e^{-\frac{t}{\tau_n}}, \qquad P_a(t) = \frac{1-\epsilon}{\epsilon} P_e(t), \qquad (3.15)$$

where ϵ represents the fraction of high frequency phonons thermalized in the thermometer, P_0 is the initial power input into the thermometer ($P_0 = \epsilon \Delta E/\tau_n$) and τ_n is the effective time constant for the thermalization of high frequency phonons that is determined by the two competing phenomena of thermalization

in the absorber and in the thermometer. τ_n can therefore be expressed as:

$$\tau_n = \left(\frac{1}{\tau_{film}} + \frac{1}{\tau_{crystal}} \right)^{-1} \tag{3.16}$$

where τ_{film} and $\tau_{crystal}$ are the time constants for the thermalization in the thermometer film and in the absorber crystal respectively.

The time constant $\tau_{crystal}$ is a property of the crystal and in particular of the crystal surface and is expected to scale as the ratio between the volume and the surface area of the absorber ($\tau_{crystal} \sim V_a/A_a$).

The time constant τ_{film} is given by:

$$\tau_{film} = \frac{\tau_0}{\bar{\eta}}, \qquad \tau_0 = \frac{2V_a}{A\langle v_\perp \alpha \rangle} \tag{3.17}$$

with A being the area of the absorber-thermometer interface and τ_0 being the ideal thermalization time for complete thermalization in the thermometer ($\epsilon = 1$) and complete absorption of high frequency phonons transmitted into the film ($\bar{\eta} = 1$). The fraction of phonons thermalized in the thermometer

$$\epsilon = \frac{\tau_{crystal}}{\tau_{crystal} + \tau_{film}} \tag{3.18}$$

affects the duration of the power input into the electron system of the thermometer $P_e(t)$, whereas the initial power input P_0 only depends on the area of the thermometer-absorber interface and on the transmission and absorption probabilities

$$P_0 = \frac{\epsilon \Delta E}{\tau_n} = \frac{\Delta E}{\tau_{film}}.^{17} \tag{3.19}$$

The simple exponential time structure of $P_e(t)$ in equation 3.15 is a consequence of the assumed frequency independence of the thermalization rate[18].

The thermal model of figure 3.5 can be described by two coupled differential equations for the temperature T_e of electrons in the thermometer and for the temperature T_a of phonons in the absorber:

$$C_e \frac{dT_e}{dt} + (T_e - T_a)G_{ea} + (T_e - T_b)G_{eb} = P_e(t) \tag{3.20}$$

$$C_a \frac{dT_a}{dt} + (T_a - T_e)G_{ea} + (T_a - T_b)G_{ab} = P_a(t) \tag{3.21}$$

---

[17] The dependence of P_0 on τ_n explains the linear dependence of the detector sensitivity on the velocity of sound in the absorber material.

[18] A frequency independent τ_{film} results when the metal film is thick enough to absorb all transmitted phonons. The situation for $\tau_{crystal}$ is less clear. However the assumption of a frequency independent thermalization is justified by observation [Prö95].

where T_b is the temperature of the heat bath.

With the initial conditions $T_a(t = 0) = T_e(t = 0) = T_b$, the equations have the following solution [Prö95] for the thermometer signal $\Delta T_e(t)$:

$$\Delta T_e(t) = \Theta(t)[A_n(e^{-t/\tau_n} - e^{-t/\tau_{in}}) + A_t(e^{-t/\tau_t} - e^{-t/\tau_n})] \qquad (3.22)$$

where the step function $\Theta(t)$ takes into account the assumption of an instantaneously established homogeneous distribution of non-thermal phonons in the absorber after the energy deposition. The solution consists of two components: a non-thermal component, that originates from the direct absorption of non-thermal phonons in the thermometer film, with amplitude A_n given by:

$$A_n = \frac{P_0 \left(\frac{1}{\tau_{in}} - \frac{G_{ab}}{C_a} \right)}{\epsilon \left(\frac{1}{\tau_t} - \frac{1}{\tau_{in}} \right) \left(\frac{1}{\tau_{in}} - \frac{1}{\tau_n} \right)} \left(\frac{\frac{1}{\tau_t} - \frac{G_{ab}}{C_a}}{G_{eb} - \frac{C_e}{C_a} G_{ab}} - \frac{\epsilon}{C_e} \right) \qquad (3.23)$$

and a thermal component, caused by the temperature rise of the absorber as measured by the thermometer, with amplitude A_t given by:

$$A_t = \frac{P_0 \left(\frac{1}{\tau_t} - \frac{G_{ab}}{C_a} \right)}{\epsilon \left(\frac{1}{\tau_t} - \frac{1}{\tau_{in}} \right) \left(\frac{1}{\tau_t} - \frac{1}{\tau_n} \right)} \left(\frac{\frac{1}{\tau_{in}} - \frac{G_{ab}}{C_a}}{G_{eb} - \frac{C_e}{C_a} G_{ab}} - \frac{\epsilon}{C_e} \right). \qquad (3.24)$$

The time constants appearing in the solution 3.22 are the effective time for thermalization of non-thermal phonons τ_n, the intrinsic thermal relaxation time of the thermometer τ_{in} (see section 3.2.3) and the thermal relaxation time of the absorber τ_t. The last two can be expressed respectively as:

$$\tau_{in} = \frac{2}{a + \sqrt{a^2 - 4b}} \qquad \tau_t = \frac{2}{a - \sqrt{a^2 - 4b}}$$

$$\qquad (3.25)$$

$$a = \frac{G_{ea} + G_{eb}}{C_e} + \frac{G_{ea} + G_{ab}}{C_a} \qquad b = \frac{G_{ea}G_{eb} + G_{ea}G_{ab} + G_{eb}G_{ab}}{C_e C_a}.$$

For CRESST detectors $C_e \ll C_a$, therefore equations 3.25 and 3.23 can be simplified as:

$$\tau_{in} \approx \frac{1}{a} \approx \frac{C_e}{G_{ea} + G_{eb}} \qquad (3.26)$$

$$\tau_t \approx \frac{a}{b} \approx \frac{C_a}{\frac{G_{eb}G_{ea}}{G_{eb} + G_{ea}} + G_{ab}} \qquad (3.27)$$

$$A_n \approx \frac{P_0}{(G_{ea} + G_{eb}) \left(1 - \frac{\tau_{in}}{\tau_n} \right) \left(1 - \frac{\tau_{in}}{\tau_t} \right)} = -\frac{\epsilon \Delta E}{C_e \left(\frac{\tau_n}{\tau_{in}} - 1 \right) \left(1 - \frac{\tau_{in}}{\tau_t} \right)}. \qquad (3.28)$$

At very low operating temperatures, where $G_{ea} \ll G_{eb}$, the intrinsic time constant of the thermometer τ_{in} can be controlled by the thermal conductance of

the thermometer to the heat sink G_{eb}.

A detector for which $\tau_{in} \gg \tau_n$ integrates the power input $P_e(t)$ and the amplitude of the non-thermal component measures the total energy of the high-frequency phonons absorbed in the thermometer ($A_n \approx -\epsilon \Delta E / C_e$), therefore the operating mode of the detector is referred to as calorimetric. In this operating mode the time constant τ_n defines the rise time of the non-thermal signal component and τ_{in} defines its decay time. Detectors for which $\tau_n \gg \tau_{in}$ behave as bolometers, measuring the flux of non-thermal phonons, with the amplitude of the non-thermal component being proportional to the power input ($A_n \approx P_0 / (G_{ea} + G_{eb})$).

Light detectors used in the CRESST experiment are optimized to work in the calorimetric mode. Therefore, for a given energy deposition, the amplitude of the non-thermal component is determined by the heat capacity of the electron system of the thermometer film. Phonon detectors, due to the characteristics of the CaWO$_4$ crystals[19], work in the bolometric mode instead.

3.2.5 Phonon collectors

In the calorimetric mode the sensitivity of detectors can be increased by decreasing the heat capacity of the thermometer, that is decreasing the area. The thickness of tungsten films is kept in the range of $2\,\mathrm{k\AA}$ in order to preserve the efficiency of non-thermal phonon absorption. For small enough thermometer films the effective life time of the non-thermal phonon population is given by $\tau_{crystal}$ (see equation 3.16 and 3.17 with $\tau_{film} \gg \tau_{crystal}$); as a consequence the amplitude of the non-thermal component of the temperature signal is independent of the thermometer size. In this limit the sensitivity of detectors can still be enhanced by decoupling the area needed for the collection of non-thermal phonons and the heat capacity of the sensor by means of superconducting phonon collectors.

The phonon collectors used in this work consist of aluminium films which form a proximity bilayer with the underlying tungsten film. The bilayer has a transition temperature close to the transition temperature of aluminium, therefore its heat capacity at typical operating temperatures is negligible.

Phonon collectors absorb the flux of non-thermal phonons and transmit the energy to the thermometer without contributing to the heat capacity of the sensor. The working principle of phonon collectors is illustrated in figure 3.6.

Absorption in phonon collectors

At typical operating temperatures of the detectors incoming high frequency phonons with energy greater than 2Δ break Cooper pairs in the superconducting

---

[19]The effective time for the thermalization of high frequency phonons τ_n is dominated by an extremely long $\tau_{crystal}$.
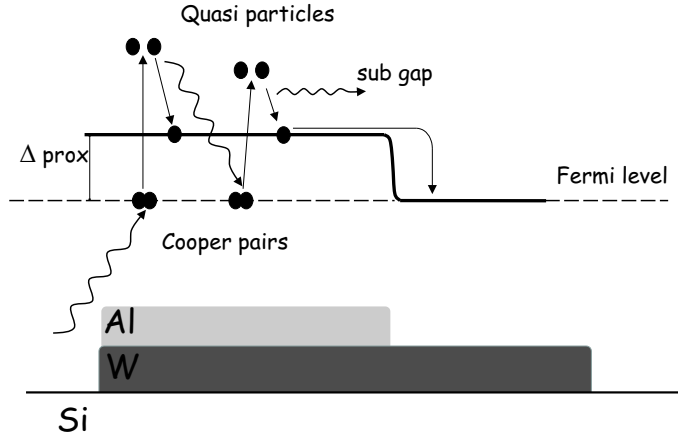
Figure 3.6: Schematic view of the working principle of phonon collectors.

bilayer producing excited quasi-particles. Considering that the average phonon energy in silicon in the relevant time interval is $\bar{E}_p = h\bar{\nu} \approx 1.5\,\mathrm{meV}$ (see figure 3.4), the produced quasi-particles are well above[20] the gap edge of the bilayer. The thickness of the superconducting layer needed to efficiently absorb all transmitted phonons can be estimated knowing the velocity of sound averaged over modes and the lifetime of a phonon of energy E_p due to the absorption with pair breaking [Kap76] in the material. In the case of pure aluminium the mean free path of phonons of energy $E_p = 1.5\,\mathrm{meV}$ ($8\Delta_{Al}$) is calculated[21] as about $3\,\mathrm{k\mathring{A}}$, therefore a $10\,\mathrm{k\mathring{A}}$ thick aluminium film is expected to absorb all transmitted phonons.

Quasi-particles relaxation

The highly excited quasi-particles quickly relax towards the gap edge through the emission of phonons. The relaxation due to inelastic scattering on thermally excited phonons is negligible in the temperature range of interest due to the decrease in the thermal phonon population. A detailed formulation of the rate of spontaneous phonon emission can be found in [Kap76]. In the specific case of aluminium the quasi-particle's lifetime varies from about $200\,\mathrm{ns}$ for quasi-particles of energy $3\Delta_{Al}$ above the gap edge, to about $300\,\mu\mathrm{s}$ for quasi-particles of energy $\Delta_{Al}/10$ above the gap edge[22]. Phonons with energy bigger than twice the energy

---

[20]According to the BCS theory, the energy gap at $T = 0$ is given by : $\Delta(T = 0) = 3.52\,k_B T_c/2$; for pure aluminium this leads to $\Delta_{Al}(T = 0) \approx 0.18\,\mathrm{meV}$. The band gap of the proximity bilayer is smaller than the band gap of pure aluminium [Sol72].

[21]For phonons of energy $E_p = 8\Delta_{Al}$ the lifetime due to absorption with pair breaking is about $88\,\mathrm{ps}$ [Kap76] and the group velocity averaged over modes is $3436\,\mathrm{m\cdot s^{-1}}$.

[22]The given values can be considered as upper limits, different experimental results [Chi79] yield a much faster relaxation.

gap of the superconducting bilayer can break other Cooper pairs exciting new quasi-particles. The process goes on until relaxation phonon energies are smaller than $2\Delta_{prox}$. Once quasi-particles have relaxed to energies smaller than $2\Delta_{prox}$ they cannot break pairs and lose their energy via emission of sub-gap phonons which are re-emitted into the absorber and as a consequence part of the energy initially transmitted by non-thermal phonons is lost [Kur82]. Roughly 50% of the energy remains in excited quasi-particles.

The competing process of recombination in which one quasi-particle combines with another one to form a pair with the emission of a phonon shows a lifetime that increases exponentially at low temperatures, reflecting the exponential decrease in the thermal population of quasi-particles. At temperatures well below the transition temperature of the superconductor the process is negligible compared with relaxation to the gap edge. The quasi-particle recombination has to be taken into account during the diffusion due to the possibility of trapping in sites of reduced energy gap (e.g. caused by the presence of lattice defects or impurities) where the density of quasi-particles can be locally enhanced. In this condition the recombination of a pair would in fact lead to the emission of sub gap phonons that are lost. To minimize losses in phonon collectors the high quality of the aluminium layer which gives a fast diffusion is fundamental.

Quasi-particles diffusion

Quasi-particles excited above the gap edge have a non vanishing group velocity v_g that allows a diffusive propagation through the film. In the limit of quasi-particles in thermal equilibrium at the detector operating temperature, much lower than the transition temperature, the average group velocity is given in [Nar78] as:

$$\langle v_g^2 \rangle \approx \frac{T}{T_c} v_F^2 \tag{3.29}$$

where v_F is the Fermi velocity. Because of the long time needed for quasi-particles to relax to thermal equilibrium due to the slow rate of spontaneous phonon emission at energies close to the gap edge[23], the velocity given in 3.29 represents the lower limit for the quasi-particles group velocity that is not reached within the time scale of interest. It is important to point out that an energy of $\Delta_{Al}/10$ corresponds to a temperature of about $200\,\mathrm{mK}$ while the operating temperature of detectors is typically of the order of $10\,\mathrm{mK}$.
Knowing the mean free path of quasi-particles l_q it is possible to calculate the distance a quasi-particle travels by diffusion within a time t as:

$$L(t) = \sqrt{\frac{\langle v_g \rangle l_q t}{3}} = \sqrt{Dt} \tag{3.30}$$

---

[23]As already mentioned, at an excitation of $\Delta_{Al}/10$ above the gap edge the quasi-particle lifetime for spontaneous phonon emission is about $300\,\mu$s.

where D is the diffusion constant. The mean free path of quasi-particles is determined by the elastic scattering on impurities and lattice defects[24]; high quality of the film is therefore needed in order to maximize the diffusion length. Assuming in the case of the aluminium film a quasi-particle mean free path equal to the normal state mean free path (that is equal to the electron mean free path l) [Hsi68], l_q can be calculated from the film electrical conductivity σ that can be expressed as [Dug77]:

$$\sigma = Ne^2l/mv_F \qquad (3.31)$$

where e and m are respectively charge and mass of electrons, N is their density and v_F is the Fermi velocity[25].

Quasi-particle diffusion in an aluminium-tungsten bilayer has been studied in detail in a previous work of the CRESST group [Loi99] [Loi01]. Diffusion without significant losses has been measured over a distance of $2\,\text{mm}$ and a quasi-particle lifetime of $9\,\text{ms}$ has been observed.

The diffusion length of quasi-particles defines the maximum size of phonon collectors.

Reaching the thermometer, whose energy gap vanishes at the transition temperature, quasi-particles relax releasing their energy to the electron system of the thermometer rising its temperature. For the correct functioning of phonon collectors, a good metallic contact with the thermometer is needed. The use of the aluminium-tungsten bilayer allows a good contact avoiding at the same time the structural defect in the superconducting diffusion film that are expected if it grows over the edges of the thermometer, only partially overlapping the tungsten film.

During the prototyping stage for the second phase of the CRESST experiment phonon collectors have been tested to enhance the sensitivity of thermometers used for light detectors.

3.3   Detector module and event discrimination

The energy deposited in the scintillating crystal by a particle interaction is mainly transferred to the phonon system and only a small fraction is converted into scintillation light. The background discrimination technique relies on the lower light yield of nuclear recoils, which result from WIMP or neutron interaction, with respect to electron recoils resulting from α, β and γ interactions [Bir67].

Photons escaping from the crystal have to be absorbed in the light detector, therefore both detectors are enclosed in a highly reflective housing in order to improve the light collection. The signal detected by a CRESST detector module

---

[24]In the case of film thickness comparable with l_q the effective mean free path is reduced by the scattering on the film surfaces.

[25]Collisions only involve electrons near the Fermi surface.

is therefore represented by two temperature signals of the form shown in equation 3.22 coming from the two calorimeters constituting the module. A schematic view of a particle interaction in a detector module is shown in figure 3.7.
The different light yield for the various interactions (i.e. the different amplitude of signals in the light detector associated with signals of a given amplitude in the phonon detector) is used to identify interactions in the main absorber.
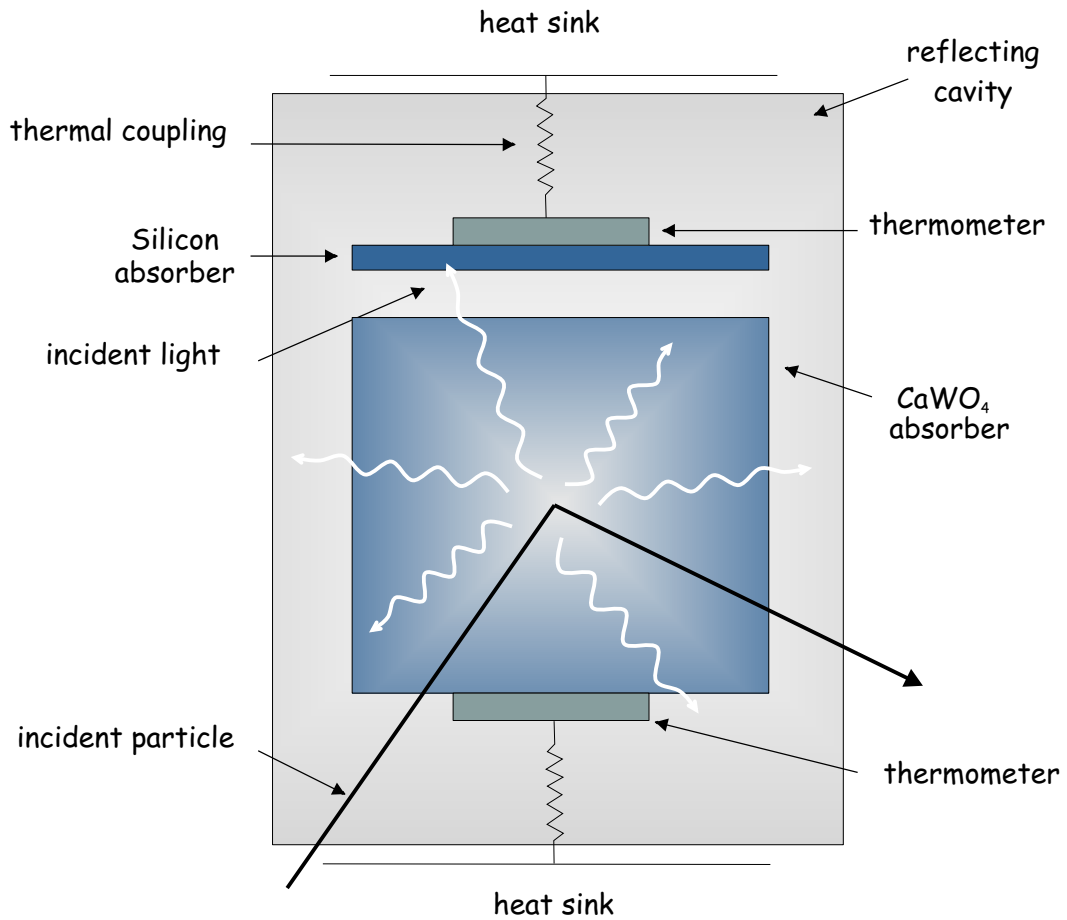

Figure 3.7: Schematic view of a particle interaction in a detector module.

Dark Matter data reported in this work were collected with two $CaWO_4$ crystals "Julia" and "Daisy" associated with light detectors "BE14" and "BE13" respectively. The prototype detector modules are identified later on as Julia/BE14 and Daisy/BE13.

Chapter 4

Data acquisition and data analysis

The setup of the CRESST experiment, where Dark Matter measurements are performed, has been described in a previous chapter. For the purpose of detector development and of light detector characterization a small self made dilution refrigerator has been used. The cryostat, installed in a Faraday cage to isolate it from electromagnetic interferences, is located in the Max-Planck-Institut in Munich[1].

In this chapter the data acquisition system used in both facilities is explained together with the main experimental procedures and the data analysis techniques.

4.1   Data acquisition system

A scheme of the data acquisition systems used both in the Munich facility and in the Gran Sasso facility during the prototyping phase of CRESST II can be seen in figure 4.1.

Copper holders which house detectors are thermally and electrically insulated from the base plate of the cryostat on which they are mounted and are weakly thermally linked to the mixing chamber via a copper wire; this design has been chosen to filter fast temperature fluctuations of the mixing chamber. The mixing chamber temperature is monitored with a carbon resistor (speer) read out by a four point AC resistance bridge able to regulate, via a PID[2] temperature controller, the power input into a heating resistor on the mixing chamber used to stabilize its temperature T_b at the desired value.

During data taking periods in the Gran Sasso setup the mixing chamber was stabilized at a temperature of a about $6\,\mathrm{mK}$; a stability of $\pm 10\,\Omega$ was reached in

---

[1]Being a ground level facility, it is not suitable for the characterization of standard phonon detectors due to the high rate caused by cosmic radiation.

[2]Proportional Integral Differential.

normal running conditions, which translates into $\pm 7\,\mu K$.

In such a setup holders represent the temperature reference for detectors and the coupling of each detector to this reference is defined by the gold thermal link of the thermometer (see section 3.1.2).

The shunt resistors of the biasing circuits (see section 3.1.3) are directly connected to the mixing chamber to minimize their Johnson noise.

Electrical connection of the detectors are realized with twisted pairs of superconducting wires. A voltage controlled floating current source, which can be adjusted by a potentiometer or an external voltage, provides the bias current for the detector readout. To reduce high frequency noise an H-type low pass filter (10 kHz) is present in each line between the current source and the reference resistor.

The SQUID sensors are located in the liquid helium bath at 4.2 K. The output signals run through differential amplifiers and then leave the Faraday cage via feedthrough filters (low pass 50 kHz).

The film heater used to stabilize the detector at the operating point and to inject heater pulses for the stability monitoring is connected to a feedback unit consisting of a summing amplifier where the voltage for regulating the temperature and the voltage corresponding to heater pulses are added, followed by an analog square-rooter needed to linearize the dependence of the heating power with respect to the input voltage[3]. The differential output of the heater circuit is connected via series resistors ($43\,k\Omega$ in the case of phonon detector, $1\,M\Omega$ for light detector; the difference is due to the different resistance of heaters and thermal coupling) to the heater on the film. The heating power and thus the detector stability is regulated by a computer controlled digital to analog converter (DAC) connected to the summing amplifier. The DAC output is provided by a software PID controller; the signal is filtered with a 10 s low pass to suppress the noise from the switching in the DAC. Exponential heater pulses with a decay time adjusted to create detector pulses resembling particle pulses, are produced by a commercial tail pulse generator triggered via software at regular time intervals. In order to span the energy range of interest, the single amplitude produced by the pulse generator is fed into a multiplier module controlled by an external voltage produced by the DAC and passed into the Faraday cage via feedthrough filters. Since the same heater pulses are used for all detectors, attenuators are needed to adjust them to the dynamic range and heater resistance of each detector.

The data acquisition systems are located outside the Faraday cages. Signals from the resistance bridge and the offset level of the feedback unit are read by a digital voltmeter (DVM). SQUID signals are fanned to produce a trigger signal

---

[3]The presence of the square-rooter is essential in a design where the same heater is used for stabilization and for test pulses. The pulse energy would otherwise depend on the offset heating power applied to stabilize the detector at the operating point.

Figure 4.1: Block diagram of the data acquisition systems. The horizontal divisions indicate the different temperature levels in cryostats.

which is shaped and AC-coupled to a trigger unit which triggers the digitizer. The signal itself passes an anti aliasing low pass filter and is then DC-coupled to a 16-bit transient digitizer. The trigger signal starts the post trigger sampling cycle of the digitizer and an external clock is used to inhibit another trigger in the required pre-trigger region for the next event, adding dead time to the measurement. The accumulated dead time is measured with separate clocks for each channel.

Each detector has an independent trigger but, during the data taking periods in the Gran Sasso facility, CRESST detector modules were read out in pairs which means that whenever one of the two detectors constituting a module had a valid trigger, digitizers of both detectors were readout and data were written to disk for off-line analysis.

4.2   Transition curve measurements

As already mentioned in section 3.1.2, the performance of the individual detector is strongly dependent on the shape of the transition curve of the superconducting phase transition thermometer. Since the bias current influences the shape of the transition (high bias currents make the transitions steeper and often more linear), transition curves of each detector are recorded for different bias currents in order to optimize the detector response. A typical example is shown in figure 4.2.
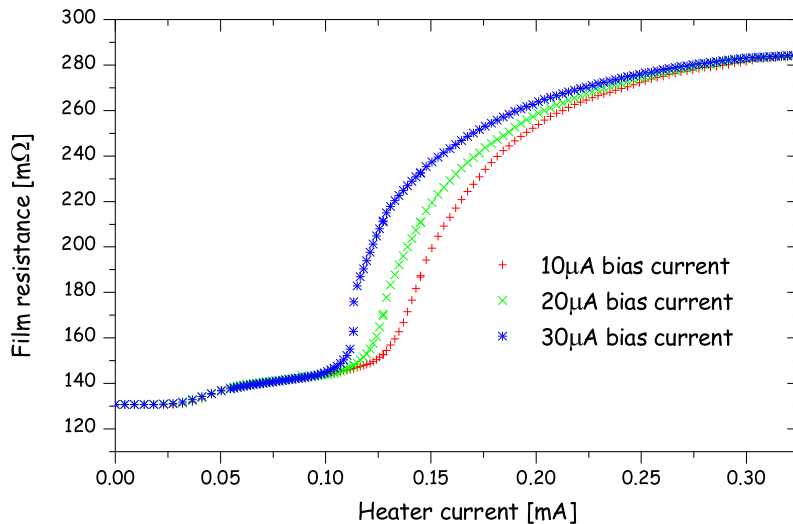

Figure 4.2: Transition curves for the phonon detector Daisy measured for different bias currents.

A transition curve measurement consists in a measurement of the SQUID output for a fixed bias current as a function of the temperature in a neighbourhood of the transition temperature of the film. To be independent from the SQUID operating point an AC-measurement is performed. Namely a square wave voltage, shaped in order not to exceed the slew rate of the SQUID, is fed to the input of the current source. The bias current is therefore switched from $-I_0$ to $+I_0$ and half of the corresponding change of the SQUID output step represents a point of the transition curve. The film temperature can be controlled by fixing the heat sink temperature T_b and varying the heating current through the film heater or alternatively varying the heat sink temperature via the resistance bridge for zero heating current through the film heater (see figure 4.3).
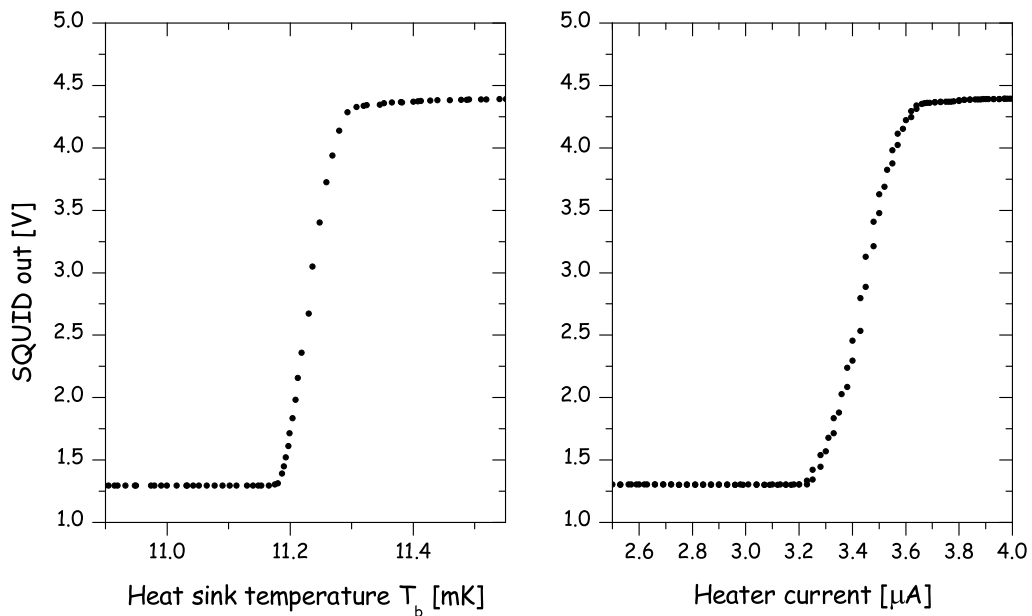

Figure 4.3: Transition curves for the light detector BE13 recorded with a bias current of $1 \, \mu A$. The left curve was recorded varying the heat sink temperature for zero heating current through the film heater; the right curve was recorded varying the heating power with the heat sink temperature fixed.

Since the stabilization of detectors during operations is achieved via the heater on the thermometers, the first method is usually applied.

4.3 The stability control

Each detector has to be stabilized independently at the chosen operating point; for a stable detector response the operating point has to be constant within

few μK. In a first phase of the CRESST II prototyping period, the base line of detectors alone was used as temperature indicator and a software PID controller was used to regulate the control voltage sent into the heater circuit[4]. As already mentioned, pulses exceeding the slew rate of the SQUID can cause flux quantum losses. The control system was dealing with such flux quantum losses by not responding to large jumps in the SQUID base line occurring in one sampling period.

In order to detect occasional fast temperature changes, which may be confused with flux quantum losses, a second control loop was implemented to check for deviations from the operating point by monitoring the amplitude of large heater pulses.

For very large heater pulses that partially saturate the detector, the amplitude of the SQUID output gives a measure of how far the operating point is from the top of the transition. The second control loop, therefore allows the identification and eventually correction of deviations from the operating point.

The achieved stability is visible in figure 4.4 where the measured pulse height of heater pulses in a prototype light detector is plotted as a function of time during a Dark Matter run.
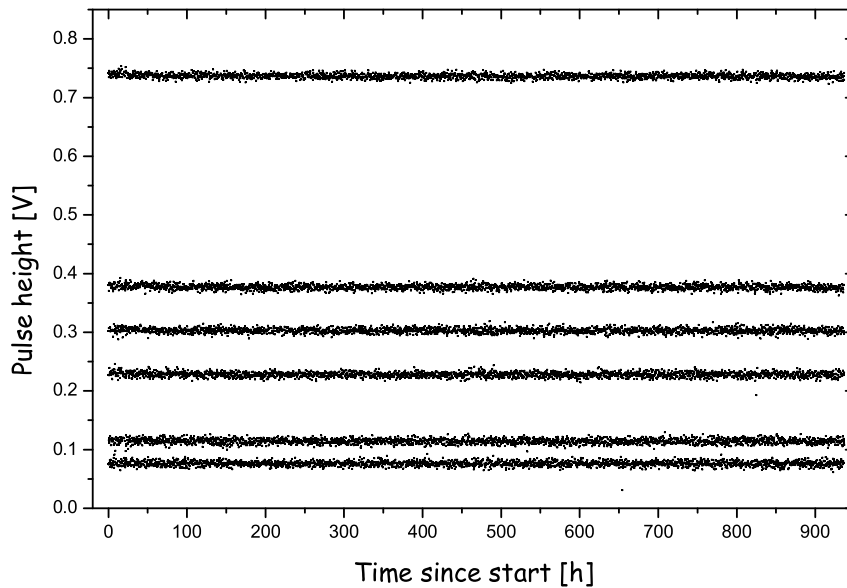

Figure 4.4: Measured pulse height of heater pulses of a prototype light detector installed in the Gran Sasso facility as a function of time. The operating point was controlled with both loops. The detector is seen to be stable within the resolution.

---

[4]The base line was sampled with a 10 Hz rate; during pulses the sampling was interrupted and the voltage kept constant.

The reference heater pulses were also recorded which allowed removal of some unstable operation periods off-line.

4.4 Data analysis

4.4.1 Pulse height evaluation

The data analysis for the CRESST experiment is performed off-line. The first step consists in a correct evaluation of the energy corresponding to recorded pulses. For that purpose the pulse height is estimated via a template fit procedure. In order to apply the procedure it is necessary to produce a template for each type of pulse from the detector of interest (e.g. heater pulses, particle pulses or, in the case of light detector, pulses due to the absorption of scintillation light) in the prevailing operating conditions. Templates are obtained by averaging, for each given pulse type, many measured pulses in the region of small pulse height where the detector is in the linear regime. Templates are then fit to all measured pulses using an amplitude scale factor, the base line and the onset time as free parameters.

This template fit method works as long as the amplitude is in the regime of linear detector response, that is for pulses that do not reach the non-linear part of the superconducting phase transition. For high pulses that approach the top of the transition the pulse height is extracted by excluding from the fit the part of the pulse where the response becomes non-linear (see figure 4.5).
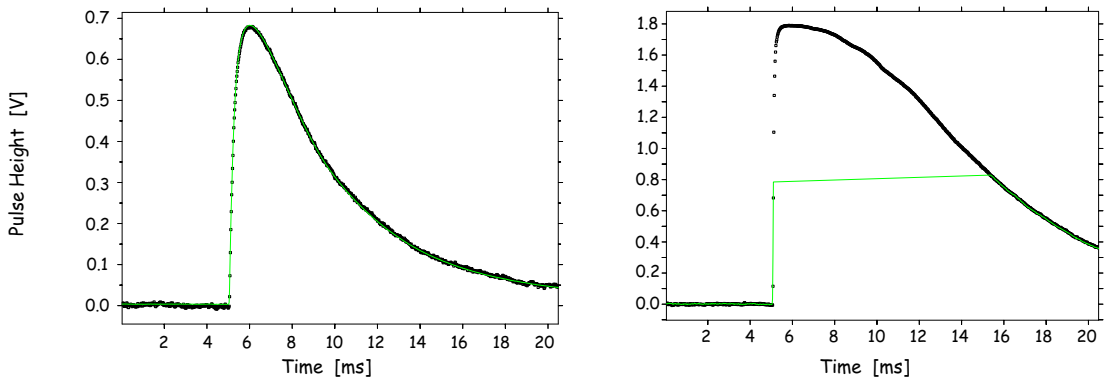

Figure 4.5: Fit of events recorded in a light detector test run with a template obtained averaging pulses from a region where the detector is linear. The fit is truncated at $0.8\,V$. For pulses with amplitude below this limit the fit procedure is standard, for pulses with amplitude exceeding this limit into the non-linear region of the detector the fit is truncated and the amplitude reconstructed from the template.

The necessary condition for the applicability of the truncated fit technique is the absolute stability of a detector at its operating point where the template has been produced. The method is revealed to be especially powerful for events that completely saturate the detector allowing a reconstruction of the spectrum essentially from the duration of pulses (see figure 4.6).
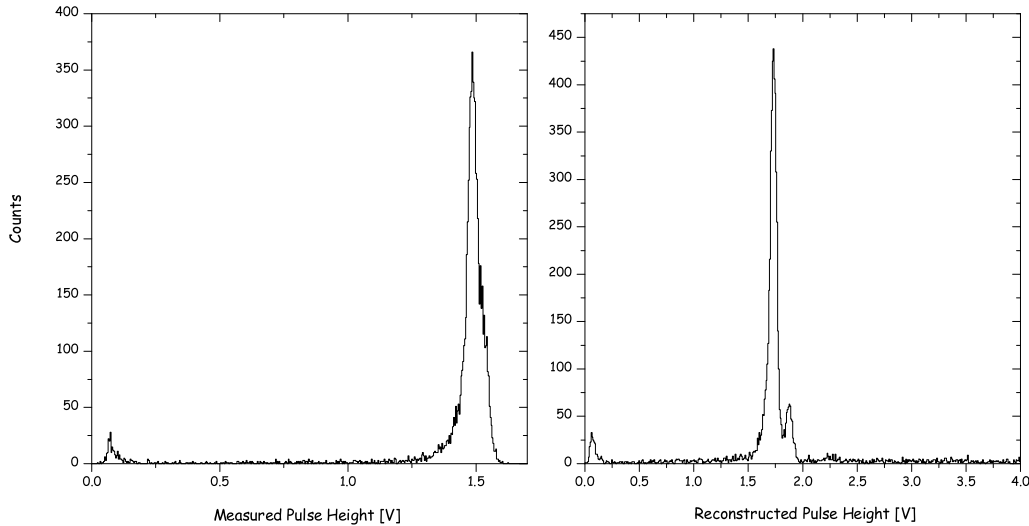

Figure 4.6: ^{55}Fe calibration measurement in a light detector test run. In the measured pulse height spectrum (left) ^{55}Fe events are saturated. The truncated fit procedure gives an accurate reconstruction of the spectrum allowing the resolution of the ^{55}Fe doublet at around 1.75 V pulse height (right).

4.4.2 Calibration procedure

Before the data taking run at LNGS the detectors were calibrated by inserting a ^{57}Co source via a removable plug through the bottom plate of the passive shielding.

From a comparison of the 122 keV peak of the ^{57}Co spectrum (see figure 4.7) with heater pulses of similar amplitude a calibration of the injected voltage in terms of γ energy is obtained. Heater pulses are then used to extrapolate the energy calibration from particle's energy high enough to penetrate the cold box down to the energy range of interest for Dark Matter detection. The detector response over the whole dynamic range is obtained by fitting the energy versus pulse height for all test pulses with a polynomial function (see figure 4.8). Once the response function is known, the energy of any particle pulse can be determined.
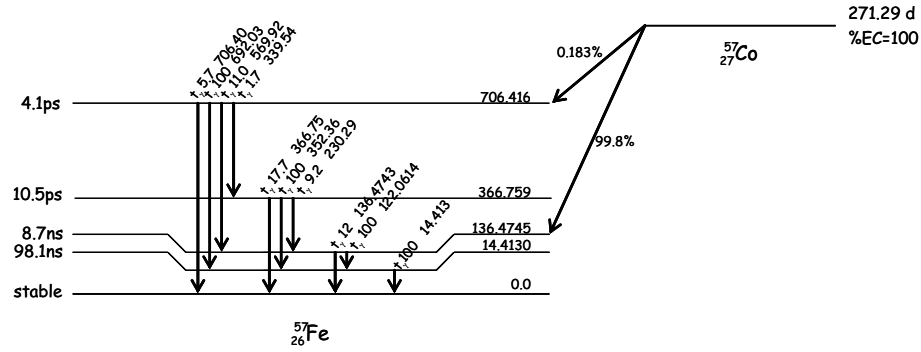
Figure 4.7: ^{57}Co decay scheme. $\dagger_\gamma$ values indicate the intensity of the line normalized to 100 for the most intense γ emitted from the level; energies are given in keV.
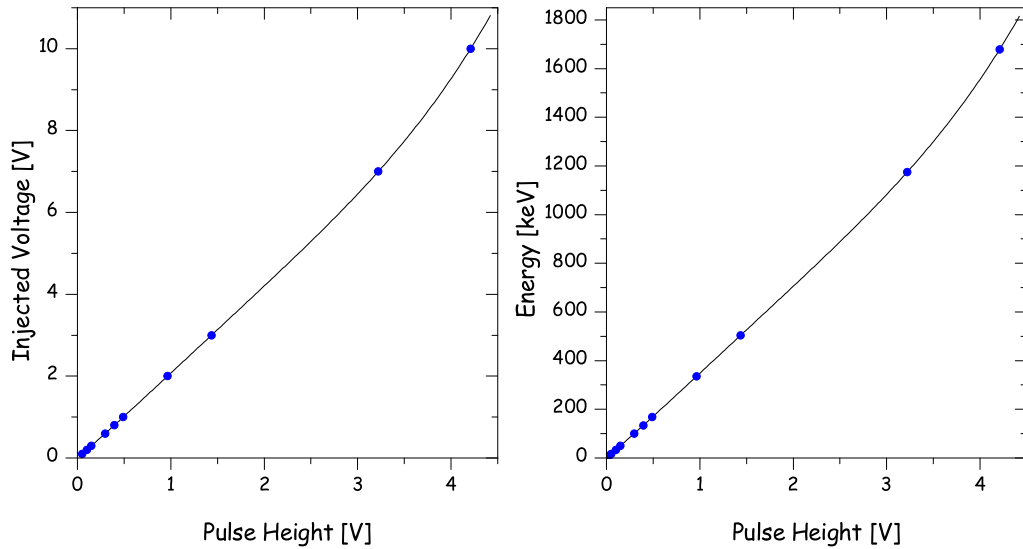

Figure 4.8: Response function of a CaWO$_4$ phonon detector. Left: Injected voltage versus pulse height. Right: Energy versus pulse height. The pulse height for heater pulses is determined with the template fit using an appropriate template. The scale factor between the injected heater voltage and γ energy is obtained comparing the amplitude of ^{57}Co pulses with heater pulses of similar amplitude.

The calibration of light detectors followed the same procedure but the calibration reference was provided by the light output of the scintillating crystal corresponding to incident 122 keV γ radiation[5]. As a consequence there is no absolute energy determination for light detectors for runs in the Gran Sasso setup,

---

[5]An absolute energy calibration for light detectors is not required to apply the discrimination technique.

but the pulse height produced in the light detector by the absorption of $122\,\mathrm{keV}$ γ in the scintillating absorber is assigned the nominal value of $122\,\mathrm{keV}$; the energy unit in the light channel is usually referred as keV electron equivalent (keV_{ee}). With this normalization, the response of the light detector is linearized using heater pulses applied to the thermometer.

This calibration technique would be affected by a non-linear relation between the energy deposited in the scintillating crystal and its light output. Such non-linearity is not observed in $CaWO_4$ (see figure 4.9).
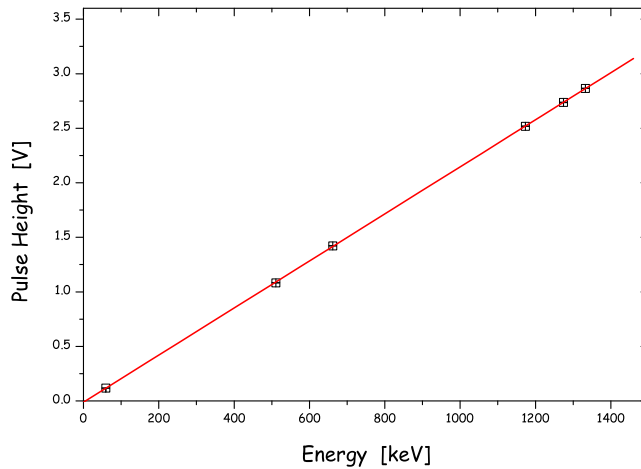

Figure 4.9: Linearity of the scintillation response as a function of the incident energy. Results are obtained by irradiating a $300\,\mathrm{g}$ $CaWO_4$ crystal at room temperature with different γ sources and measuring the scintillation light with a photomultiplier [Nin05].

Besides monitoring the long term stability of detectors and extrapolating the energy calibration, heater pulses provide a means to characterize the behaviour of the trigger efficiency. For that purpose a relatively high number of test pulses is injected near the detector threshold.

In a Dark Matter run a calibration with ^{57}Co is performed after operating conditions have been settled and it is repeated whenever settings are changed. Test pulses are injected during the whole run.

For the absolute calibration of light detectors an extremely low energetic source is needed due to the sensitivity of these detectors that are optimized to detect small amounts of scintillation light. For this purpose, dedicated runs have been performed in the Munich setup with a ^{55}Fe X-ray source installed inside the cryostat [6].

Results of these measurements are presented in the next chapter.

---

[6]The attenuation length of $6\,\mathrm{keV}$ X-rays in copper is about $10\,\mu\mathrm{m}$.

Chapter 5

Light detectors

Due to the small energy deposited by a WIMP-nucleus elastic scattering and the small amount of detectable scintillation light[1], the sensitivity and the threshold of light detectors are crucial parameters for the event discrimination in the energy range relevant for WIMP interactions on tungsten nuclei (threshold to 40 keV energy deposition in the $CaWO_4$ crystal).

In this chapter the main characteristics of light detectors are presented together with results of the improvements achieved by this work.

5.1 Substrates

The choice of the material to be used as substrate for light detectors is constrained by technical requirements related to the experimental technique. That means the material has to be suitable as an absorber in cryogenic calorimeters (i.e. it has to be heat leak free) and it has to have a high melting point to allow the deposition of thin films of materials with high melting temperature such as tungsten. In addition, to efficiently detect the scintillation light, photons have to be absorbed in the substrate, which means the material has to be non-transparent for the light that has to be detected, and the generated non-thermal phonons have to reach the thermometer film, which requires a material with good phonon propagation properties.

On the basis of the experience with sapphire detectors of CRESST I, the first choice as light detector substrate for CRESST II was sapphire with a sputtered silicon absorption layer on one surface[2]. Standard untreated silicon wafers are also suitable absorbers for the visible light emitted by $CaWO_4$ [Mac55].

Detailed results of the parallel testing of the two possibilities can be found in [Fra02].

---

[1] Due to the light collection efficiency, typically only about 1% of the energy of an electron recoil event in $CaWO_4$ is detected as scintillation light.

[2] Standard sapphire substrates are transparent for scintillation light in the visible spectrum.

Although the absorption layers sputtered on sapphire substrates have high potential, they introduce additional processing during the preparation of detectors. In addition, with the performed testing, it has been observed that the light signal detected with thermometers produced on sapphire wafers with sputtered silicon layers was smaller than for pure silicon wafers, notwithstanding the slightly better absorption measured for the former[3]. Therefore during the prototyping phase of CRESST II the attention has been focused on the optimization of light detectors with pure silicon absorbers.

Superconducting transitions of tungsten on silicon with critical temperature of the order of 10 mK have been obtained using the natural silicon oxide as an interdiffusion barrier[4].

To reduce the reflectivity of silicon, standard photovoltaic techniques of texturing have been tested [DiS03]. The resolution of textured detectors was observed to worsen noticeably with respect to a non textured silicon absorber. The effect was attributed to the increase of the effective surface area produced by the texturing that translates into a lower volume to surface ratio. This causes additional scattering of non-thermal phonons on the wafer surface before absorption in the film and consequently enhances the probability of thermalization [Kna85].

Light detector absorbers used during the prototyping phase of CRESST II consist of a $(30 \times 30 \times 0.45)\,\text{mm}^3$ n-type silicon wafer[5] (see figure 2.15) with 200 Å SiO_2 layer on both surfaces. The oxide layer thickness has been limited to 200 Å in order to minimize the degradation of high frequency phonons in the transmission to the thermometer film through the SiO_2 [Die79].

During this work additional tests have been performed with substrates consisting of a $1\,\mu\text{m}$ thick intrinsic silicon layer (001) epitaxially grown on an r-plane sapphire substrate 0.46 mm thick [Lar66]. For this particular type of substrate the surface on which to deposit the thermometer has to be chosen in order to maximize the energy flux per unit area and unit time ($\dot{Q}$) across the boundary from the substrate to the thermometer. Assuming a situation of dynamical equilibrium between the two layers of the substrate, that is (see equation 3.9)

$$\dot{Q}_{Si \rightarrow Sapph} = \dot{Q}_{Sapph \rightarrow Si}\,, \tag{5.1}$$

from values listed in table 3.3 it is possible to estimate that

$$\frac{\dot{Q}_{Si \rightarrow W}}{\dot{Q}_{Sapph \rightarrow W}} \approx 1. \tag{5.2}$$

On the basis of this consideration alone the two surfaces come out to be equivalent for the thermometer deposition. During a number of tests it has been

---

[3]The fact that the increased absorption is not reflected in the detected energy has probably to be ascribed to a partial degradation of phonons in the sputtered film.

[4]Tungsten films grown on silicon wafers from which the oxide layer was previously removed showed a critical temperature of the order of 1 K. [DiS03]

[5]The size of the light detector absorber is limited by the holder design.

possible to grow tungsten films with superconducting transitions in the interesting temperature range both on the silicon and on the sapphire surfaces.

The underling idea for testing the silicon-on-sapphire (SOS) is to exploit the potential of sapphire in terms of phonon transport, but with an epitaxially grown absorption layer which gives a good interface between the two materials [Vre86] and avoids the additional fabrication process needed to sputter the absorption layer. Figure 5.1 shows a light detector produced on a SOS substrate.

The reliability and reproducibility of superconducting transitions of tungsten films grown on silicon and on sapphire are still the objects of ongoing investigation. Unreliable and non reproducible superconducting transitions represented, in the course of this work, an important limitation for the testing steps needed to fully characterize and optimize the detector performances.

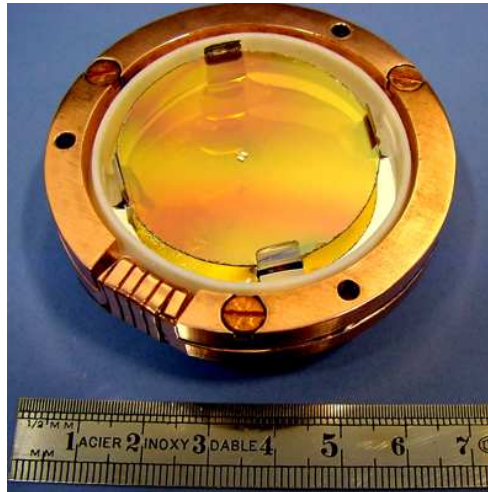Results of the performed tests are presented later in this chapter.

Figure 5.1: Light detector produced on SOS substrate.

5.2 Detector layout

The discrimination threshold of a detector module, that is the minimum energy at which the scintillation light due to a nuclear recoil in the scintillating crystal can be detected and distinguished from the scintillation light due to an electron recoil event, mostly depends on the performance of the light detector. To satisfy the experimental needs the light detector threshold has to be as low as possible and the total energy collected has to be maximized, this means it is necessary to maximize both the absorption of light and the collection of phonons in the thermometer. The collected energy depends on the size and on the material of

the substrate and the thermometer.

The optimization of these light detector parameters has been the main topic of the present work.

5.2.1   Film geometry

As mentioned before (see section 3.2.4), light detectors are optimized to work in calorimetric mode where the amplitude of the non-thermal signal component is defined by the heat capacity of the thermometer film. The detector sensitivity, expressed as the resistance change per energy change ($\delta R_f/\delta E$), can therefore be increased by reducing the thermometer's heat capacity[6] by decreasing the area of the thermometer film. The film thickness is fixed in order to efficiently absorb high frequency phonons coming from the substrate.

In a design where the thermometer alone provides the collecting area, the sensitivity gain is limited by the efficiency of the phonon collection process whose time constant is inversely proportional to the collecting area: for a $1\,\mathrm{mm}^2$ tungsten film on a $(30{\times}30{\times}0.45)\,\mathrm{mm}^3$ silicon wafer, the time constant τ_0 that appears in equation 3.17 is about $0.55\,\mathrm{ms}$.

To overcome this limit a very small tungsten thermometer has been combined with relatively large aluminium phonon collectors. This is obtained by partially covering the original tungsten film with a $10\,\mathrm{k\mathring{A}}$ thick aluminium layer that provides $1\,\mathrm{mm}^2$ of collecting area. The uncovered tungsten film in the middle (see figure 5.2) serves as the thermometer. Applying this solution, for a $1\,\mathrm{mm}^2$ collecting area the heat capacity of the system, whose only contribution at the operating temperature of detectors comes from the tungsten film ($(0.45{\times}0.3)\,\mathrm{mm}^2$ area, $2\,\mathrm{k\mathring{A}}$ thickness) is reduced by an order of magnitude with respect to a design where the same collecting area is provided by the thermometer alone. For a typical sensor of the described geometry operated at $10\,\mathrm{mK}$ in the middle of the transition ($R_{op}/R_n{=}1/2$ in equation 3.8) the heat capacity at the operating temperature is about $50\,\mathrm{fJ{\cdot}K^{-1}}$.
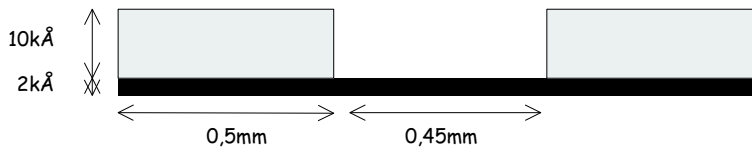

Figure 5.2: Cross section of the thermometer geometry for light detectors used in the prototyping stage of the second phase of CRESST.

The size of phonon collectors has been chosen in order to have negligible

---

[6]Decreasing the heat capacity C, a given energy δE collected in the thermometer leads to a higher temperature rise and therefore to a higher resistance rise.

quasi particles losses according to results obtained in [Loi01] and to maximize the energy collected in the thermometer film.

Limiting the attention to the non-thermal component of the signal by neglecting the thermalization in the absorber, the energy collected in the thermometer film is given by the time integral of the power input into the electron system of the thermometer (see equation 3.15), that is:

$$\delta E = \int_0^\infty P_0 e^{-\frac{t}{\tau_n}} dt = P_0 \tau_n. \tag{5.3}$$

From equation 5.3 it can be seen that the maximization of the energy collected in the thermometer requires the maximization of both the initial power input into the electron system of the thermometer, P_0, and the effective time constant for the thermalization of high frequency phonons, τ_n. The area of the thermometer-absorber interface has therefore to be sufficiently small as to be in the limit where the effective life-time of the non-thermal phonon population is given by $\tau_{crystal}$ (see equation 3.16) but, within this limit, it has to be as big as possible in order to maximize the initial power input into the electron system of the thermometer (see equation 3.15 and 3.19).

A further advantage of thermometers in this limit comes from the fact that partially inefficient phonon collectors would fail to maximize P_0 but would not reduce τ_n, as τ_n is independent of the area of the thermometer-absorber interface.

5.2.2 Thermal link

A decrease of the heat capacity of the system entails, for a given value of the thermal coupling to the heat sink G, a reduction of the intrinsic thermal relaxation time constant of the thermometer as expressed in equation 3.26. In order to optimize the detector sensitivity by integrating the energy of the scintillation light, the thermal relaxation time of the thermometer has to be longer than the light response of the scintillating crystal. In the specific case of $CaWO_4$ crystals the light emission occurs on a time scale of hundreds of microseconds at low temperatures (see figure 2.10 and [Bla83]).

The long time constant needed in the light detector has been obtained by replacing the gold wire thermal link described in section 3.1.2 with a gold film structure which allows a precise adjustment of the thermal coupling G. The thermal coupling of light detectors used during the prototyping period of the second phase of the CRESST experiment was realized via a 500 Å thick, $(1.5 \times 0.1)\,mm^2$ structure overlapping the tungsten film at one end and connected to the heat bath via a $25\,\mu m$ diameter gold wire[7] bonded onto an electrically insulated pad on the

---

[7]The conductance defined by the series of the two resistances is dominated by the resistance of the film structure, by far the largest of the two.

detector holder (see figure 5.3). The electrical insulation of the pad helps the immunity of the detector against electric interference.

5.2.3   Heater

The enhancement of the detector sensitivity achievable with a reduction of the heat capacity of the tungsten film is limited by the presence of the additional structures needed for detector operation. In order to minimize its contribution to the heat capacity of the system, the film heater is realized with an additional gold film structure of $(0.1 \times 0.24)\,\text{mm}^2$ area and $3\,\text{k\AA}$ thickness overlapping the tungsten thermometer on the other side with respect to the thermal link. The contribution of the heater structure to the heat capacity of the system at a temperature of $10\,\text{mK}$ is about $5\,\text{fJ·K}^{-1}$ (a comparable contribution to the heat capacity of the system comes from the structure realizing the thermal link). This heat capacity compares favourably with that of a gold wire heater which contributes about $300\,\text{fJ·K}^{-1}$ per millimeter of wire.

A scheme of the electrical end thermal connection of the light detector sensor is shown in figure 5.3.
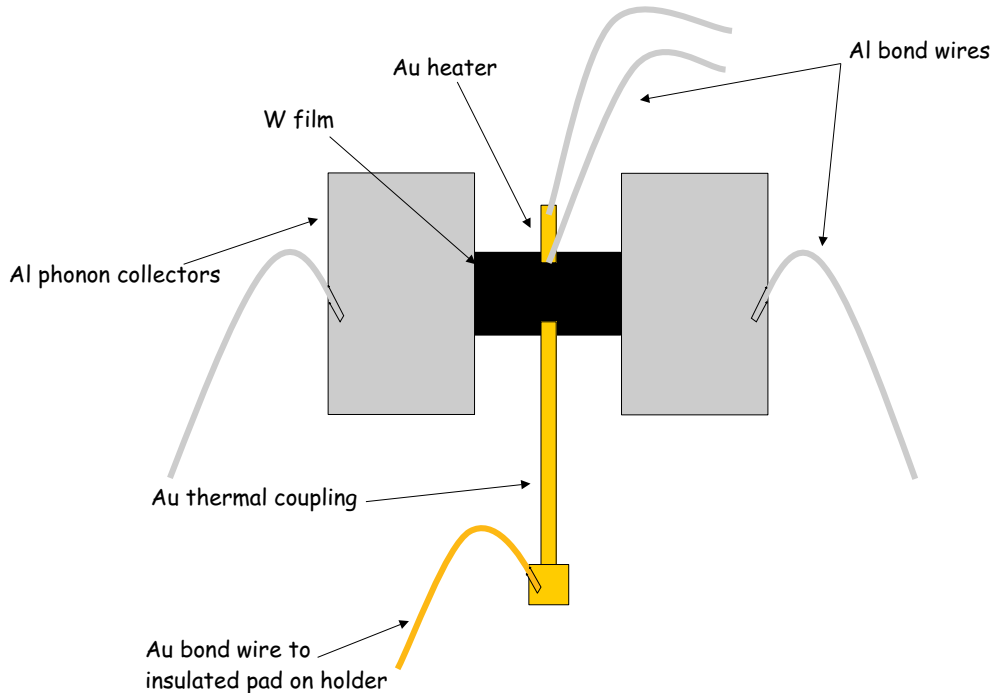

Figure 5.3: Layout and connection scheme of a light detector used in the prototyping stage of the second phase of CRESST.

A further possibility of improvement comes from the proposed use of a small

portion of the thermal link as heater, electrically shorting the rest with a superconducting structure as shown in figure 5.4. This solution, allowing a photolithography defined structure without the additional contribution to the heat capacity of the system due to the separate heater[8], has been successfully applied in some of the light detectors used for testing purposes in the Munich setup and is applied to light detectors under construction for the second phase of CRESST.
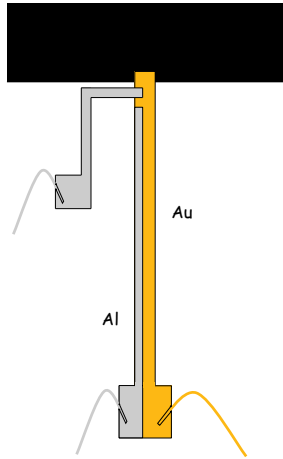

Figure 5.4: Layout of the new design of heater and thermal link for light detector sensors.

5.3 Detector fabrication

The first step of detector fabrication consists in the deposition of the tungsten film onto a previously cleaned surface of the absorber. The cleaning of surfaces is mandatory to obtain reproducible transition temperatures of films because ferromagnetic contaminations of the tungsten film in the order of ppm can significantly lower the transition temperature. Films are produced in an ultra high vacuum system using a tungsten single crystal with 99.99% purity as evaporation material. During the process the substrates are heated to ensure a good growth of the metal film[9].

After deposition tungsten films are structured to the final shape with a positive

---

[8]Removing the second structure used as heater halves the contribution to the heat capacity of the system due to gold.

[9]In the case of $CaWO_4$ crystals during a single evaporation run a buffer layer of SiO_2 is deposited through a shadow mask onto the crystal surface before the tungsten deposition in order to prevent interdiffusion between the film and the crystal.

photolithographic process and wet chemical etching[10]. Additional photolitho-
graphic lift off processes followed by deposition steps are performed to produce
aluminium and gold structures.

To meet the required surface cleanliness and radiopurity, several cleaning steps
are applied during the procedure.

A detailed description of the fabrication processes is given in [Fra02].
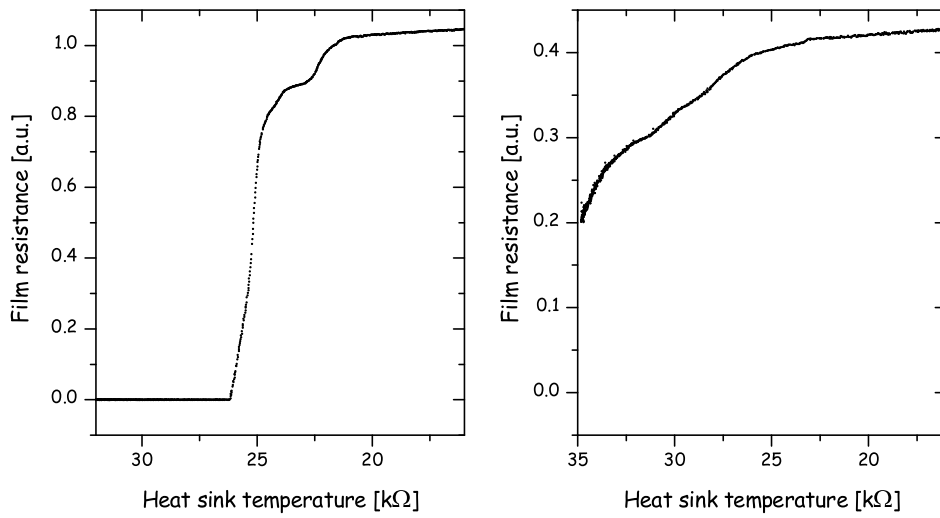

Figure 5.5: Transition curve of the same tungsten film as produced (left) and after
10 minutes backing at 150°C (right). The heat sink temperature is expressed as the
resistance of the carbon resistor monitoring the mixing chamber of the cryostat. The
resistance of the film is expressed in arbitrary units and the different measured values
can be ascribed to the different mounting. After the thermal treatment the film does
not become fully superconducting within the temperature range of the cryostat.

As already mentioned, the reliability and reproducibility of the superconduct-
ing transitions of light detectors' thermometers is still the subject of study. For
that purpose the influence of each step of the sensor fabrication process on the
superconducting transition of the tungsten films has been checked.

For some of the tungsten films it has been observed that both the shape of the
superconducting transition and the critical temperature are modified by a ther-
mal treatment simulating the conditions to which films are exposed during some
of the fabrication steps (e.g. baking of photo resist during photolithographic pro-
cesses, cleaning of surfaces with ion guns before gold and aluminium depositions)
as can be seen in figure 5.5.

---

[10]For tungsten etching a diluted mixture of NaH_2PO_4, NaOH and $Na_3Fe(CN)_6$ is used
instead of the conventional potassium based etchants to avoid radioactive contamination by
^{40}K.

5.4   Results

The effect of the introduction of aluminium phonon collectors and the thin film heater and thermal link can be qualitatively estimated from figure 5.6 where such a light detector is compared with a light detector in which the collecting area is provided by the thermometer alone, having as a calibration reference the same $CaWO_4$ crystal irradiated with a ^{57}Co source.
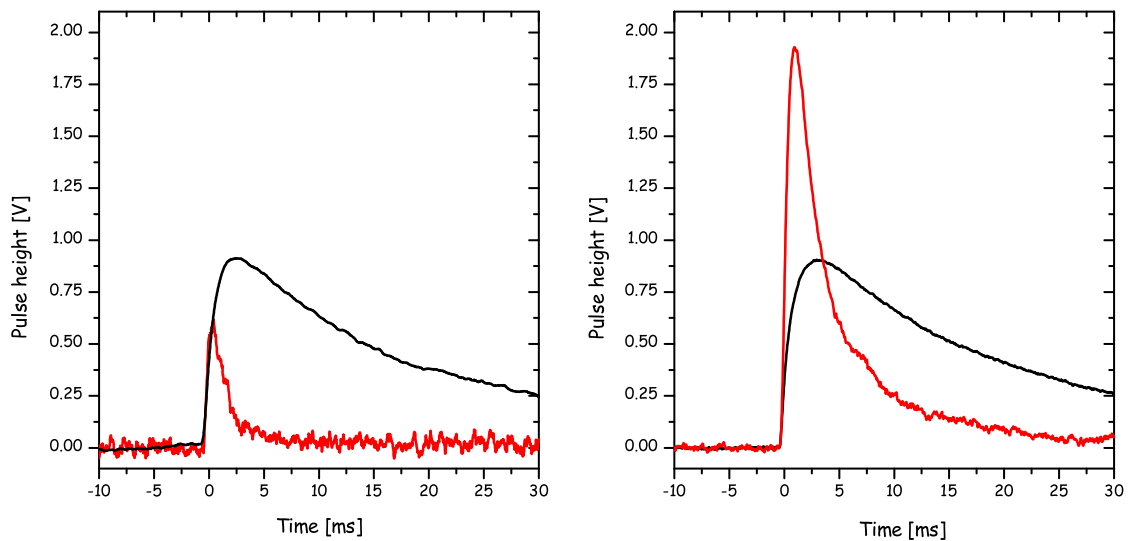Both the detector sensitivity and the signal quality can be seen to be significantly improved.

Figure 5.6: The $CaWO_4$ phonon detector Daisy mounted with a standard light detector (left) and with a light detector with phonon collectors and thin film thermal link (right) during two runs in the Gran Sasso setup. The black line is the measured signal in the phonon detector corresponding to about 122 keV energy deposition.

Since light detectors are optimized to operate in calorimetric mode, the pulse shape can be described, starting from equation 3.22, as:

$$f(t) = A_1(e^{-(t-t_0)/\tau_{in}} - e^{-(t-t_0)/\tau_n}) + A_2(e^{-(t-t_0)/\tau_t} - e^{-(t-t_0)/\tau_n}) + b \qquad (5.4)$$

where t_0 is the onset time of the pulse, and A_1, A_2 and b are three positive numbers representing the amplitude of the two signal components and of the baseline respectively. In this operating regime pulses are characterized by one common rise time for the two signal components and by two exponential decays. A fit of a light detector pulse is shown in figure 5.7 and relevant parameters resulting from the fit to data on particle interactions in the light detector absorber are shown in figure 5.8. In particular these results are obtained with the light

detector "BE10" consisting of a $(30 \times 30 \times 0.45) \text{mm}^3$ n-type silicon absorber with a thermometer of the geometry described in section 5.2.
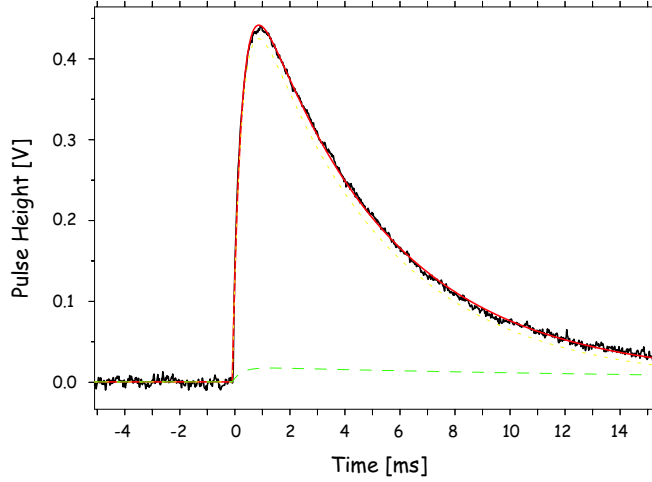

Figure 5.7: Pulse shape of the light detector BE10. The solid line represents the fit of a particle event of 3.8 keV in the light detector absorber. The dotted curve represents the non-thermal contribution to the signal while the dashed line represents the thermal component.

It can be seen that the thermal component gives only a marginal contribution to the signal amplitude. The decay time of the non-thermal component is the intrinsic time constant of the thermometer τ_{in}, which is controlled by the thermal coupling of the thermometer to the heat sink (see equation 3.26) whereas the rise time, which in a thermometer layout without phonon collectors is given by the time constant for the thermalization of high-frequency phonons (see equation 3.16), may receive an additional contribution due to the diffusion of quasi-particles when phonon collectors are used.

The fitted rise time of pulses in a light detector ($\tau_n = 0.349 \pm 0.006 \text{ ms}$) suggests that the effective life time of the non-thermal phonon population is not controlled by τ_{film} (see equation 3.16), as the ideal thermalization time[11] of the thermometer τ_0 that appears in equation 3.17 is always longer than the observed τ_n. Moreover the measured value seems to be longer than the thermalization time of the absorber crystal $\tau_{crystal}$ which, for the considered absorber dimensions, can be estimated to be about $120 \, \mu\text{s}$ [12].

As a consequence it can be inferred that the observed rise time of the signal

---

[11] For a 1 mm^2 tungsten film on a $(30 \times 30 \times 0.45) \text{ mm}^3$ silicon wafer, τ_0 is about 0.55 ms.

[12] The thermalization time of the absorber crystal is expected to scale as the ratio between the volume and the surface area of the absorber. Therefore, from the value measured in [Prö95], it is possible to evaluate $\tau_{crystal}$ for the current absorber geometry.
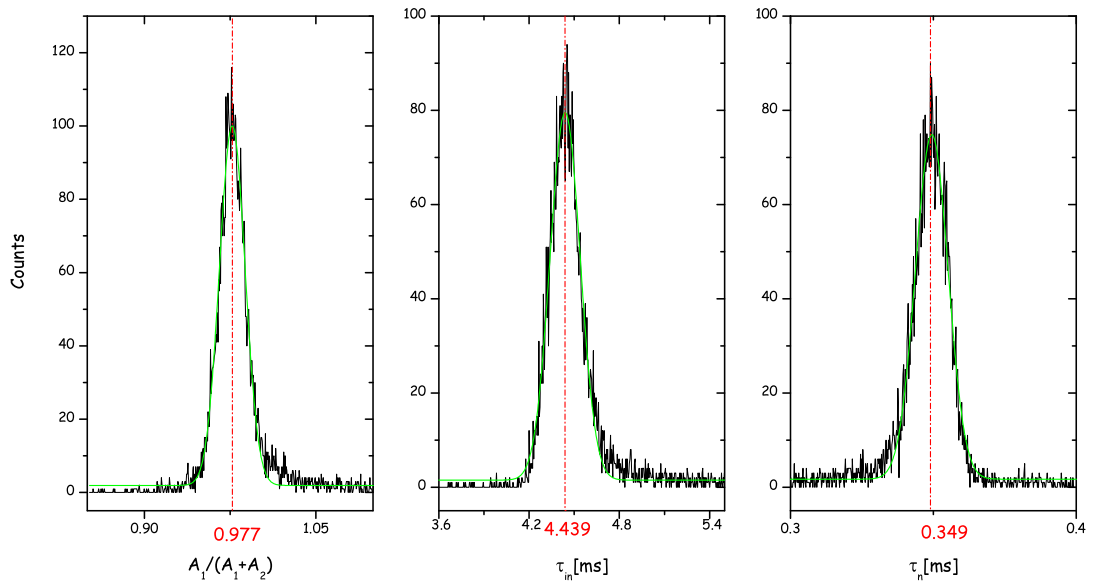
Figure 5.8: Relevant parameters resulting from the fit to data on particle interactions in the light detector absorber. Left: Ratio of non-thermal to thermal component. Center: decay time τ_{in} of the non-thermal component. Right: rise time τ_n of the two signal components.

is largely given by the time needed for quasi-particles to diffuse into the thermometer. Given the typical dimensions of the phonon collectors used, this is larger than expected from results obtained in a previous work of the CRESST group [Loi99] [Loi01] where quasi-particles have been measured to diffuse in an aluminium-tungsten bilayer over a distance of 2 mm in a time of about 0,2 ms. This suggests that the quality of the bilayer is a critical issue in order to improve the quasi-particle diffusion.

Recent measurements performed with a transition electron microscope [Hau05] showed that tungsten films grown on sapphire substrates have perfect crystalline structure whereas films grown on silicon substrates exhibit a polycrystalline structure, probably due to the presence of the amorphous oxide layer. As a consequence the tungsten-aluminium bilayer is expected to have a much better quality on sapphire substrates. This represents an additional argument for the use of silicon-on-sapphire absorbers.

A longer rise time is observed for pulses produced by the scintillation light, reflecting the time response of the scintillating crystal used. In figure 5.9 the different pulse shapes of signals originated from direct interaction in the light detector absorber and from the light emitted by a facing scintillating crystal[13]

---

[13]The two classes of signals can be distinguished in an independent way due to the fact

can be observed. In the specific case the light signal is due to the scintillation of
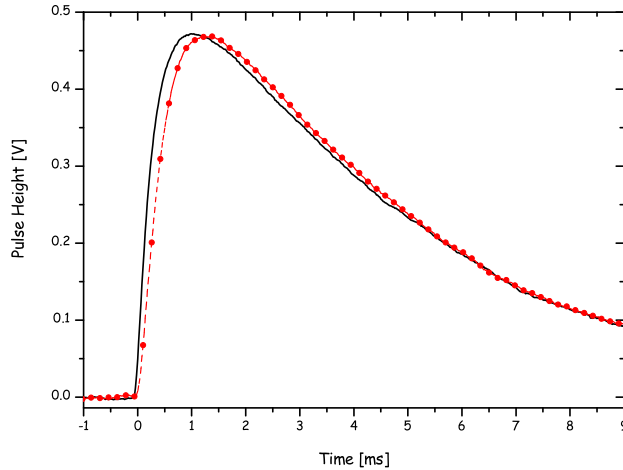a $ZnWO_4$ crystal and the measured rise time is about 0.55 ms.

Figure 5.9: Pulse shape of a 4 keV particle event in the light detector absorber (solid
curve) and of scintillation light signal of the same energy from a $ZnWO_4$ crystal (dotted
curve) in the light detector BE10.

5.4.1   Absorption

In order to achieve a good event discrimination in the energy range relevant for
WIMP interactions on tungsten nuclei, the amount of detected light has to be
maximized.

In the ideal case of a perfect crystal (i.e. without self absorption and light
trapping effects) and of a perfect reflecting cavity, the amount of detected light
would be independent of the size of the light detector.

A dependence of the amount of detected light on the absorber size has been
observed using a photomultiplier in a setup which tries to reproduce as much as
possible the geometry of a module (see figure 5.10). For that purpose a crystal
was placed in a reflecting cavity with the polymeric multilayer foil reflector placed
at a distance of 5 mm from the crystal; additional masks covered with multilayer
foil could be placed in front of the photocathode simulating the shape of the
"light detector". The main difference with respect to the layout of a detector
module derives from the fact that in a module the light detector is fully exposed
on both sides as it is located inside the reflecting cavity, therefore the light that

---

that light signals from direct interaction are not in coincidence with signals from the phonon
detector.

goes behind the light detector can be reflected and absorbed in the back side, while the light that does not hit the PMT directly but is reflected back at the side of the mask has a lower chance of being detected. As a consequence results presented in figure 5.11 have to be considered as lower limits of the detectable light.
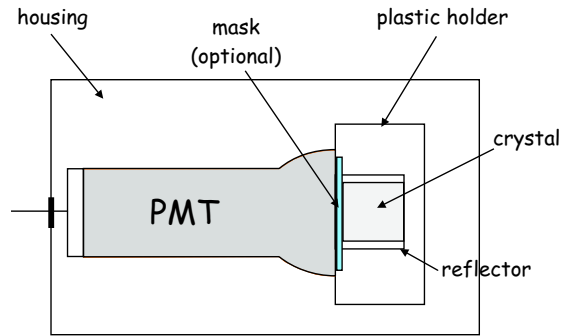

Figure 5.10: Schematic view of the photomultiplier setup used to verify the dependence of the detected light on the absorber size. On that purpose masks of different sizes are placed between the crystal and the photocathode [Nin04a].

Using the light detected without masks as reference, the detected light is reduced to about 71% when having a round mask of 40 mm diameter and to about 60% with a squared mask $(30{\times}30)\,\text{mm}^2$.
The effect is ascribed to non-ideal behaviour of the crystal because simulations of the holder with polymeric multilayer foil as a reflector indicate that the performance of the reflecting cavity is close to ideal [Fra02].
This observation, combined with the observation that the scintillation light does not escape the crystal with a uniform distribution but with well defined patterns which depend on the crystal sample[14], indicates that a unique quantitative optimization of the size of light detector absorbers is not possible due to the strong difference among various crystals.
The present choice has been to move from square detector absorbers $(30 \times 30 \times 0.45)\,\text{mm}^3$, used during the prototyping period, to round absorbers $(\varnothing{=}40\,\text{mm})$ that match the symmetry of the $CaWO_4$ crystals and at the same time lead to an increase of the absorbing area. For the future a better reproducibility of the characteristics of $CaWO_4$ crystals is being actively pursued in collaboration with crystal growers.
Tests to evaluate their absorption have been performed on SOS substrates, which could represent an attractive alternative to pure silicon. For that purpose results

---

[14]Tests have been performed having a small radioactive α source lying on one crystal surface and recording the emitted scintillation light with photographic films. Details on the tests and results are reported in [Nin05].
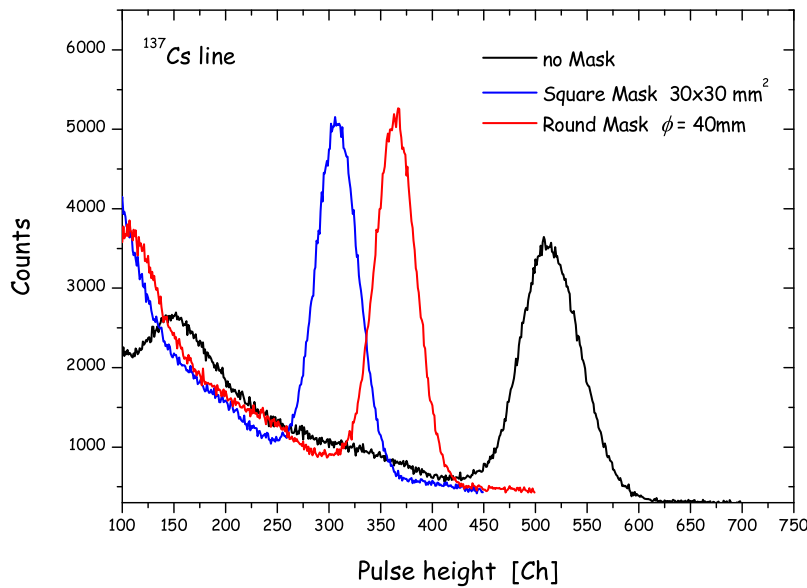
Figure 5.11: Amount of detected light using the PMT setup of figure 5.10 for different mask shapes. The detected light scales with the surface area of photocathode exposed to the scintillation light [Nin04a].

from transmission and reflectivity measurements have been combined to estimate the absorption of the material.

The transmission measurements were performed at room temperature using a Perkin Elmer Lambda 19 spectrometer at the Technical University of Munich in Garching.
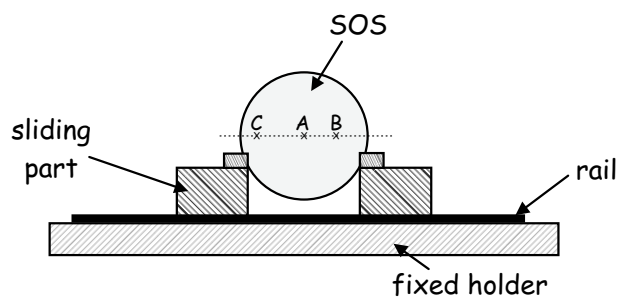
Figure 5.12: Schematic cross section of the holder used for the transmission and reflectivity measurements. Different probed positions are marked with a cross.

The spectra taken in the visible range from 250 nm to 700 nm in 1 nm steps for three different positions on the substrate, marked with crosse in figure 5.12, are shown in figure 5.13. Clearly visible for wavelengths larger than 450 nm is

the interference due to the reflection on the two surfaces of the thin silicon film. The transmission is observed to be uniform over the substrate[15].
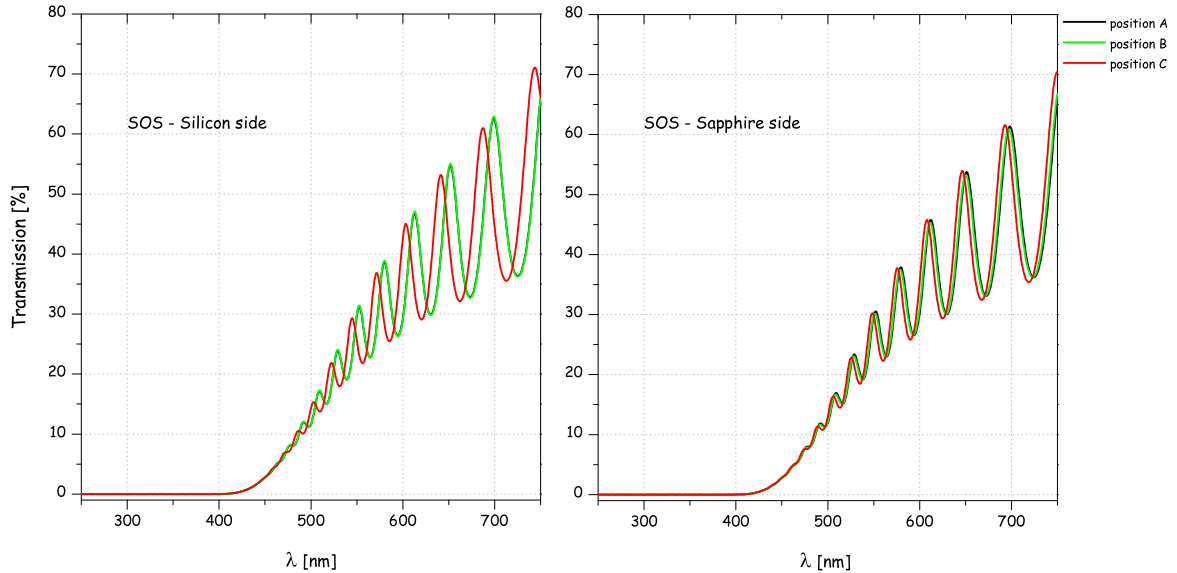

Figure 5.13: Transmission spectra for a SOS substrate measured in three different positions with silicon (left) and sapphire (right) side facing the light source.

Reflectivity measurements were performed at room temperature using a Kontron SFM 25 spectrophotometer at the Max-Planck-Institut in Munich, in the range from $350\,\mathrm{nm}$ to $600\,\mathrm{nm}$, in $2\,\mathrm{nm}$ steps with a spectrometer slit of $\sim 1\,\mathrm{mm}$. Reflection spectra measured in the central position (position A), are shown in figure 5.14. The reflection is lower when measuring through the sapphire layer.

From a combination with the previous results the absorption of the material can be estimated. In figure 5.15 it can be seen that the silicon layer gives an absorption of about 75% at the peak of the $CaWO_4$ emission, which increases to about 85% when measuring through the sapphire layer.

In normal operating conditions both sides of the light detector absorb the light, with the side facing the $CaWO_4$ being dominant [Fra02]. The real absorption will therefore be an average of the two, but with a dependence on the side facing the scintillating crystal (i.e. the side where the thermometer is deposited). In parallel with these tests, complete light detectors produced on SOS substrates ($40\,\mathrm{mm}$ diameter) with the thermometer on the silicon surface have been operated as cryogenic detectors in combination with a $(20 \times 10 \times 5)\,\mathrm{mm}^3$ $ZnWO_4$

---

[15]The small shift in the transmission curve measured when the light source is directed to a point close to edge of the substrate can be ascribed either to a misalignment of the substrate or to a different thickness of the silicon layer.
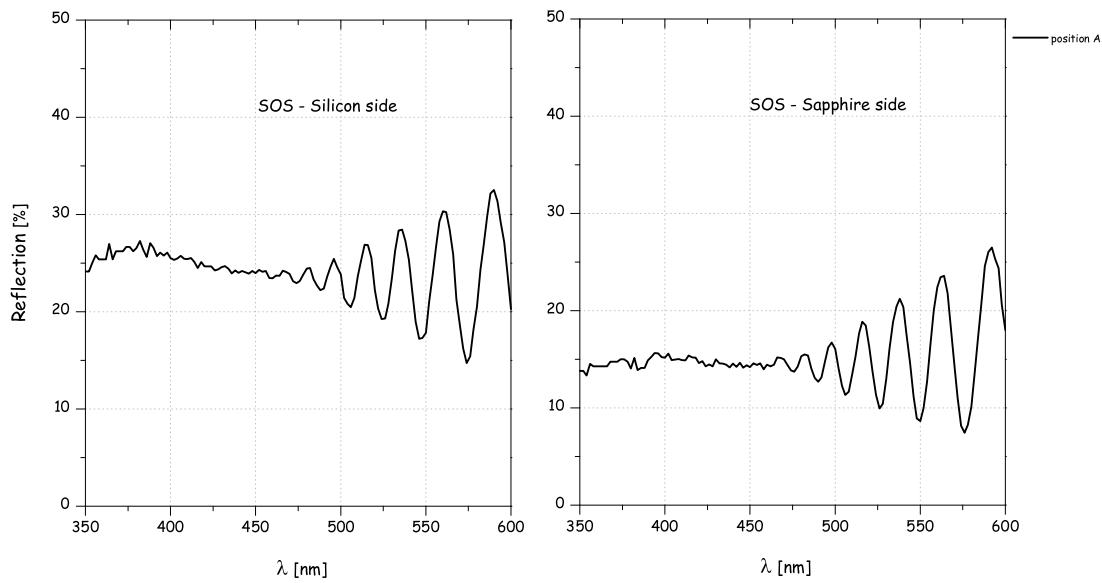
Figure 5.14: Reflection spectra for a SOS substrate measured in the central position with silicon (left) and sapphire (right) side facing the light source.
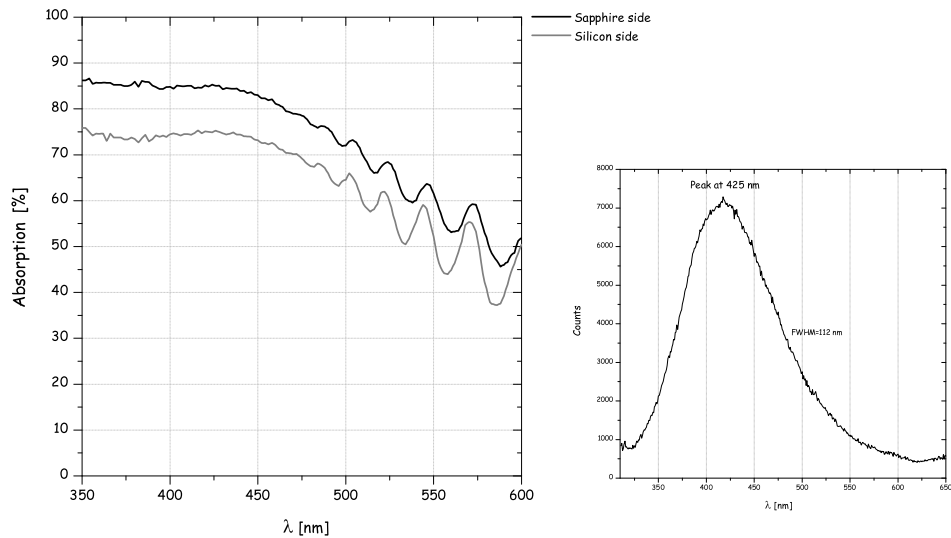

Figure 5.15: Absorption of SOS substrate between 350 and 600 nm estimated from the combination of a transmission and a reflectivity measurement. In gray and black are the different values obtained by measuring on the silicon and on the sapphire side respectively. A typical emission spectrum for a $CaWO_4$ crystal at room temperature is also shown [Nin05].

crystal in order to compare their performance with respect to silicon light detectors operated in the same setup. A relevant parameter for the comparison is the detected light, namely the fraction of the total energy deposited in the scintillating crystal that is measured in the light detector. This quantity includes not only the efficiency of the light detector, but also the efficiency of the light production and collection. Table 5.1 compiles the results of two different measurements.

Light Detector	Absorber	Size	Detected Light
BE10	Silicon	$(30 \times 30)\,\text{mm}^2$	1.2 %
SOS08	SOS-silicon	$\varnothing\,40\,\text{mm}$	1 %

Table 5.1: Fraction of the energy deposited in the ZnWO$_4$ detected in the light detector for different absorber materials.

Due to the extremely small size of the reference light source with respect to both light detector absorbers, the difference is ascribable to the different absorption properties of the material.
To confirm the behaviour observed with the transmission and reflectivity measurements, the same test will be repeated with light detectors produced on SOS substrates of the same size but having the thermometer on the sapphire surface.

5.4.2 Pulse Height

Besides the absolute amount of detected light, another important parameter to compare different materials is the observed temperature rise for a given energy deposition. This quantity also includes the efficiency of the phonon transport in the absorber and the efficiency of the quasi-particle transport from phonon collectors into the tungsten film.
The temperature rise for a 6 keV energy deposition has been estimated for the light detectors BE10 and SOS08. Results are summarized in table 5.2.

Light Detector	Absorber	T_{op} [mK]	C_{op} [fJ·K^{-1}]	$\Delta T_{op}(6\,\text{keV})$ [μK]
BE10	Silicon	29.18	94	39
SOS08	SOS-silicon	20.02	47	120

Table 5.2: Temperature rise for a 6 keV energy deposition in different absorber materials. For comparison operating temperatures and heat capacities calculated in the operating point are also listed.

For a quantitative comparison of the two absorber materials it is necessary to account for the different heat capacities of thermometers used, due both to a

different operating temperature[16] and also a different geometry. Appropriately
scaling the values in table 5.2, it can be seen that a 6 keV energy deposition
in the SOS absorber induces a temperature rise corresponding to 150% of the
temperature rise caused by the same energy deposition in a pure silicon absorber.

5.4.3   Threshold

An important property of light detectors is the minimum amount of detectable
energy (threshold). The threshold of a detector is determined by the baseline
noise which is the combination of different contributions (e.g. Johnson noise,
phonon noise, SQUID noise etc.). Two groups of noise sources can be distin-
guished: current like noise and energy like noise. The former originates in the
readout circuit and the SQUID and represents a constant noise level whereas the
latter originates in the detector itself and therefore is affected in the same way
as the signal by an increased detector sensitivity[17]. As a consequence, when the
noise starts to be dominated by energy like sources, the detector performance in
terms of signal to noise is not expected to improve with an improved sensitivity.
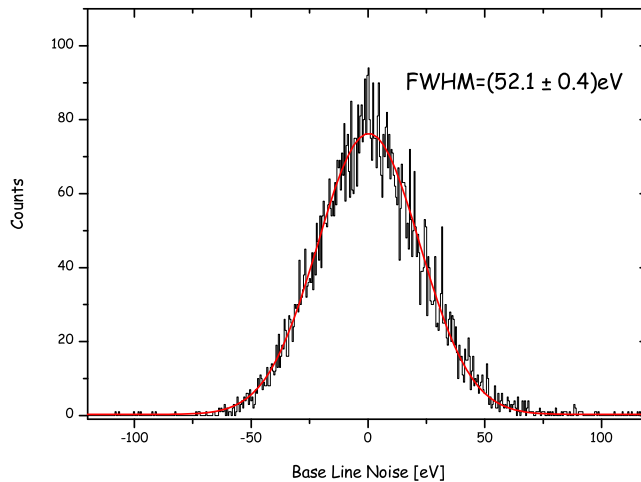

Figure 5.16: Spectrum of random base line samples over energy for the light detector
BE10 measured in the Munich setup.

Figure 5.16 shows the distribution of the base line noise for the light detector
BE10 measured in the Munich setup. The distribution is well represented by

---

[16]Different operating temperatures do not affect the quasi-particle diffusion due to the fact
that quasi-particles above the gap edge are out of thermal equilibrium.

[17]This aspect will be further exploited in a section 6.1.1 when comparing the noise level of
phonon and light detectors.

a Gaussian centered at zero with a FWHM[18] of about 52 eV. This measured noise level is well above all the contributions expected by the sources described in section 3.1.4. Therefore further detailed investigations are needed in order to understand the origin of this noise and to improve the light detector performances in this respect.

5.4.4 Uniformity

A possible non-uniformity of the response in the thin light detector substrates due to energy losses may limit the achievable resolution in normal running conditions when the absorber is non-uniformly irradiated.

In thin substrates non-thermal phonons created by an energy deposition far from the thermometer have to undergo many surface reflections before being absorbed in the thermometer and each one can lead to the decay of the phonons. For a given energy deposition in the absorber the measured amount on high frequency phonons would then depend on the distance of the energy deposition from the thermometer. To determine the significance of losses in the substrates, light detectors have been irradiated at different spots at different distances from the thermometer. By comparing pulse heights and resolutions of the different positions the losses in the substrates are derived.

Silicon

In silicon light detectors a position dependent response is expected due to the presence of the oxide layer on wafers which enhances losses of non-thermal phonons at the surfaces [Die79].

Tests to check the uniformity of the response have been performed irradiating the light detector BE10 with a ^{55}Fe X-ray source.

The spectrum obtained while illuminating the silicon absorber in one single spot using a collimator of 0.55 mm diameter[19] positioned on the diagonal of the square wafer at about 12.5 mm from the center (position of the thermometer) is shown in figure 5.17.

Adding to the previous one a second collimator of 0.35 mm diameter[20] positioned on the diagonal of the square wafer at a distance of about 6.5 mm from the center leads to the spectrum shown in figure 5.18. The collimating holes were chosen to be of different sizes in order to associate peaks in the spectrum with

---

[18]The acquired experience with CRESST detectors indicates that a value of five standard deviations of the distribution represents a conservative threshold for detectors.

[19]Due to the reduced possibilities of collimation in the limited space available in the cryostat, the finite size of the source (for conservativeness the source size has been assumed to be the size of its support) and technical limits in the collimator fabrication, the actual size of the illuminated spot on the absorber is about 0.94 mm diameter.

[20]The actual size of the illuminated spot on the slide is about 0.74 mm diameter.
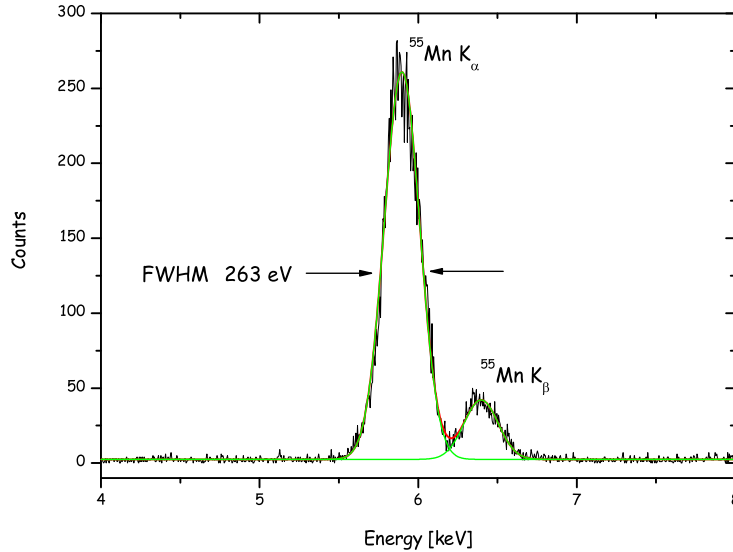
Figure 5.17: ^{55}Fe spectrum of the silicon light detector BE10 irradiated at one position. The gaussian fit of two peaks is superimposed.

the position on the silicon slide.

The described arrangement allows a measurement of the uniformity of the detector response not affected by the influence of the wafer's edges and of the thermometer itself.

The contributions of the different holes could not be separated within the limit of the resolution.

The resolution is observed to worsen which suggests that a slightly different response is obtained from the different illuminated positions on the absorber.

A qualitative evaluation of the separation of the two doublets has been obtained by fitting the spectrum of figure 5.18 with four gaussian peaks. Limiting the attention to the K_α line and keeping fixed the resolution of the two peaks to the value obtained in the test with a single collimator and their relative amplitudes as constrained by the geometrical configuration, the two K_α lines are about 2.5 % of their pulse height apart. This value gives an approximate estimate of the losses in the substrate for events whose distance from the thermometer differs by 6 mm.

A similar broadening of the K_α line (FWHM ≈ 320 eV) has been measured in a configuration where one of the two collimators, whose distance from the thermometer differs also by 6 mm, illuminates the region of the absorber edge. This indicates that the detectors are not affected by the presence of a region of smaller sensitivity[21]. Conversely an enhancement of about 7% of the detector response has been observed when illuminating the substrate in the region directly

---

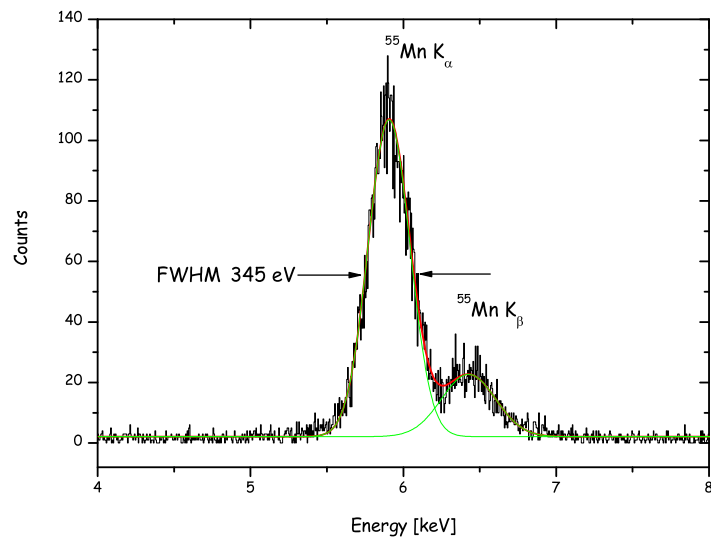[21]The substrate edges do not represent a dead volume for the detector.

Figure 5.18: ^{55}Fe spectrum of the silicon light detector BE10 irradiated at two different positions. A gaussian fit of two peaks is superimposed.
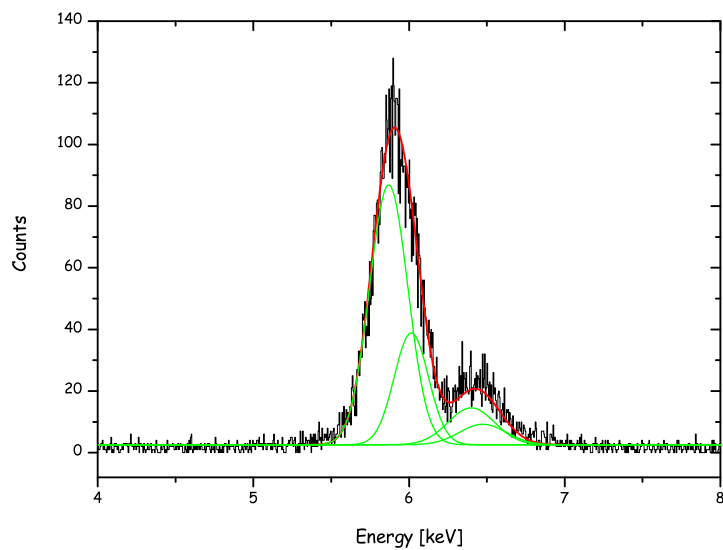

Figure 5.19: ^{55}Fe spectrum of the silicon light detector BE10 irradiated at two different positions. A gaussian fit of four peaks is superimposed.

behind the sensor. Phonons produced there by the interaction can be readily absorbed in the thermometer without undergoing any reflection.

The overall importance of the effect is negligible due to the small area of the

sensor in comparison with the absorber.

Silicon-on-Sapphire

In silicon-on-sapphire light detectors a less pronounced position dependence of
the response is expected due to the absence of the oxide layer on the sapphire
surface.

To compare the effect of losses in the different absorbers the light detector SOS08
has been irradiated in the same setup used for the silicon light detector.

The reconstructed spectrum (see section 4.4.1), obtained by illuminating the
absorber in one single spot using a collimator of $0.55 \, \text{mm}$ diameter at about
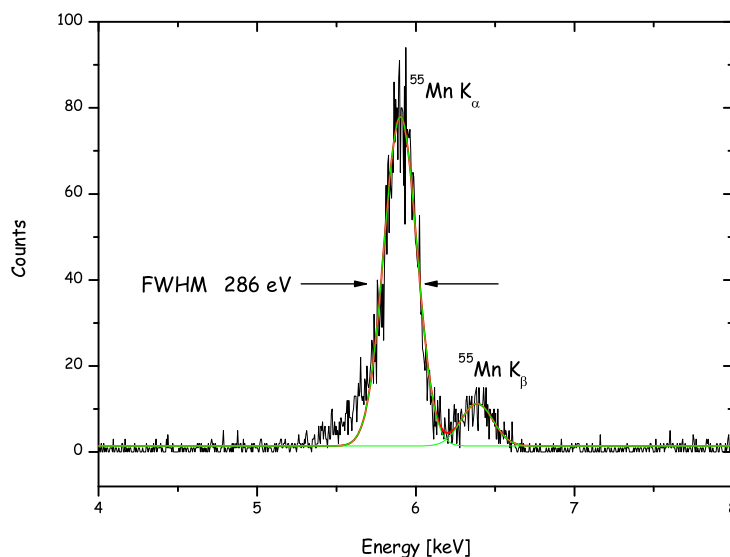$12.5 \, \text{mm}$ from the center (where the thermometer is positioned), is shown in
figure 5.20.

Figure 5.20: ^{55}Fe spectrum of the silicon-on-sapphire light detector SOS08 irradiated
at one position, reconstructed with the truncated fit method. A gaussian fit of two
peaks is superimposed.

The slightly worse energy resolution with respect to the value obtained for
pure silicon can be ascribed to the algorithm of pulse height reconstruction that,
as already pointed out, requires an absolute stability of the detector in the oper-
ating point; a condition that is never fulfilled in the ground level setup in Munich
due to the high event rate. Therefore, for a quantitative comparison the test has
to be repeated on a detector with a larger dynamic range[22] in which the ^{55}Fe can
be observed without the need to apply the truncated-fit reconstruction.

---

[22]This requires the fine tuning of the production process in order to obtain a light detector
that performs well but is less sensitive and therefore is not saturated by a $6 \, \text{keV}$ X-ray.

Chapter 6

Gran Sasso measurements

During the prototyping phase of CRESST II a number of short runs were performed in order to optimize the detector modules.

Besides allowing problems related with the scaling up of the proof-of-principle detector to be fixed and the thorough study of contaminations present in the crystal [Coz04], data taken with two detector modules during the period from January to March 2004 allowed the CRESST experiment to establish competitive limits on WIMP Dark Matter using the active background suppression technique.

6.1   Testing results

A central aspect of detector module optimization was the modification of the holding system in order to get rid of the spurious pulses without any associated light (dark events) which were observed in the phonon detector, unexplainable by known background sources.

An illustrative example of the problem can be seen in figure 6.1 where data taken in an early run (Run 26) are presented. The data sample corresponds to an exposure of 0.948 kg day of the module Daisy/BE13. The $CaWO_4$ crystal was held with teflon clamps (see figure 2.14) and the holder was assembled to have the transparent Polyethylenenaphthalate (PEN) support layer of the reflecting foil facing the detectors.

Despite the short exposure, there is a significant number of events in the energy range of interest for Dark Matter search.

The hypothesis of these events being due to alpha decays of nuclei implanted on surfaces surrounding the detector has been checked by removing all plastic materials[1] in the vicinity of the $CaWO_4$ crystal, namely Teflon clamps, which were replaced with silver coated Cu-Be clamps and the polymeric multilayer foil, which was substituted with a silver reflector. The data sample corresponding

---

[1]Materials that have electrostatic charged surfaces favour the deposition of dust particles and consequently of radon daughters.
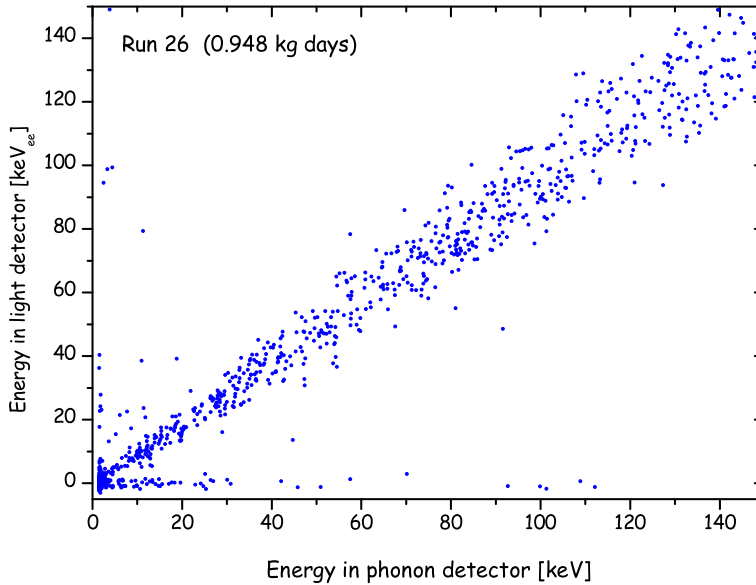
Figure 6.1: Energy in the light detector versus energy in the phonon detector for the module Daisy/BE13 in Run 26.

to an exposure of 8.1 kg day of the module Daisy/BE13 in this modified holder (Run 27) is shown in figure 6.2.
Notwithstanding the significant improvement with respect to the previous situation that can be observed at low energies, the use of this reflector led to a noticeable worsening of the light detector resolution at low energies that implies a worsening of the discrimination threshold. In addition, in the scatter plot a well defined class of events between 80 and 110 keV is clearly visible with little associated light that was not so prominent in the previous data set. The events appear at energies where no WIMP induced recoils are expected and with a rate that cannot be accounted with the expected WIMP-nucleus elastic scattering cross section. These events originate from the α decay of ^{210}Po (^{222}Rn daughter), which may be slightly implanted on the reflector or crystal surface by the parent α decay, from which only the daughter nucleus ^{206}Pb reaches the scintillating crystal. The implantation explains the broad measured spectrum. In the case of ^{210}Po implanted on the reflector surface the energy distribution of the daughter nuclei is expected to extend from the value corresponding to the kinetic energy of the nucleus (104 keV) down to lower values as a consequence of losses in escaping the material. Conversely, in the case of ^{210}Po implanted on the crystal surface, the measured energy distribution is expected to extend towards higher energy due to the contribution of the energy lost by the α in escaping the material.

While the latter situation is not problematic, the former could be a potentially dangerous source of background because the energy of the daughter nucleus, that can extend down to the interesting energy range, would be detected in the phonon detector together with a light signal typical for the recoil of a heavy nucleus, consequently mimic a WIMP event.
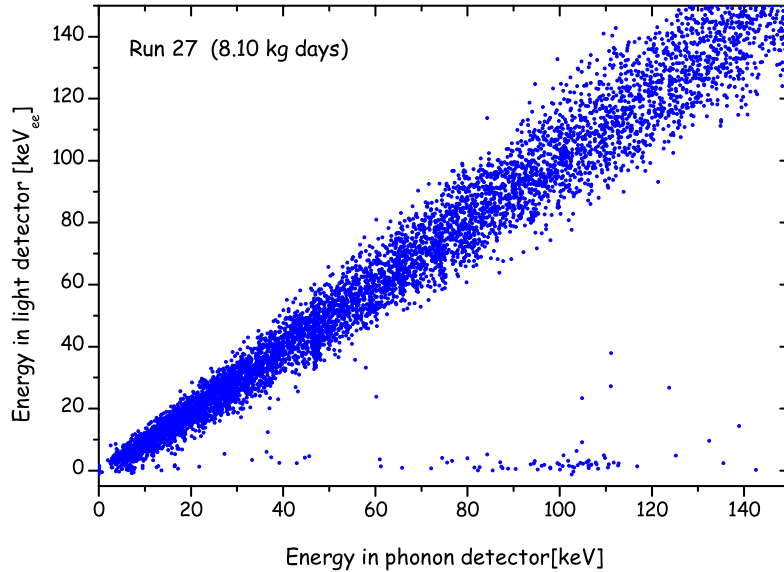

Figure 6.2: Energy in the light detector versus energy in the phonon detector for the module Daisy/BE13 in Run 27.

As mentioned in a previous section (see section 2.3.2), this background is naturally suppressed by the presence of a scintillating layer on the inner side of the reflecting cavity where the absorption of α particles makes a further production of scintillating light. The effect can be clearly observed from the data sample collected with the module Daisy/BE13 in Run 28 (figure 6.3). In this case the $CaWO_4$ crystal was held as in the previous run with silver coated Cu-Be clamps but the reflector was again the polymeric foil mounted with the scintillating PEN support layer facing the detectors.
The statistics of events between 80 and 110 keV in the phonon detector with little associated light is significantly reduced with respect to Run 27; furthermore the number of events in the energy range of interest for Dark Matter search is still at the level of the previous run suggesting that dark events observed in the early runs have to be attributed to stress on the scintillating crystal due to the holding system.
The interpretation is supported by the observation that dark events from the data sample of Run 26 have no associated light as expected for pulses produced
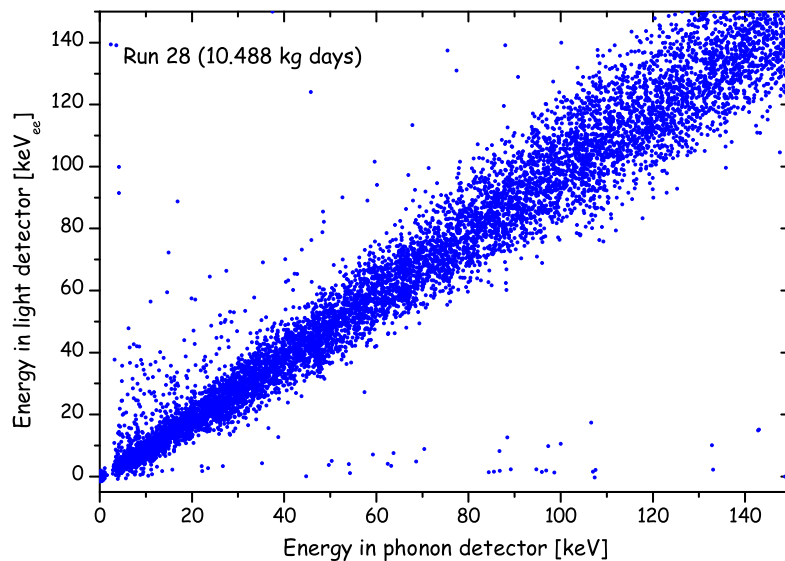
Figure 6.3: Energy in the light detector versus energy in the phonon detector for the module Daisy/BE13 in Run 28.

by stress in the crystal, whereas dark events observed in Run 27 and Run 28 show little but clearly detectable light signals as shown in figure 6.4.
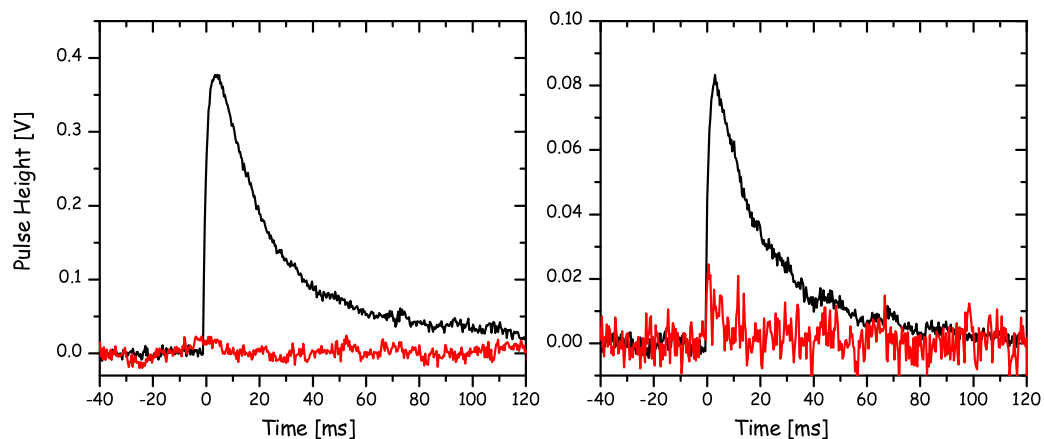
Figure 6.4: "Dark events" in the module Daisy/BE13 observed in Run 26 (left) and Run 28 (right). The black line is the measured signal in the phonon channel corresponding to about 27 keV energy deposition.

The holding system by Cu-Be clamps (figure 2.14) will be adopted in the final holder design for CRESST phase II detector modules.

In the future design all parts of the holder that extend inside the reflector, besides being highly reflective, will be coated with a scintillating layer in order to completely suppress the background due to contamination of the surfaces surrounding the detectors.

6.1.1 Light detectors

The short runs performed during the prototyping phase of CRESST II allowed a detailed study of the light detectors' performances when running in a low background environment in association with a 300 g $CaWO_4$ crystal. Due to the high interaction rate at sea level in the big scintillating crystal, a complete module can be reliably tested only in an underground facility.

Results presented concern two light detectors (BE13 and BE14) with the thermometer geometry shown in figure 5.3 produced on $(30{\times}30{\times}0.45)mm^3$ n-type silicon absorbers with $200\,\text{Å}$ SiO_2 layers on both surfaces.

Threshold

As already mentioned in section 5.4.3, an important property of light detectors is the energy threshold that is determined by the noise of the base line.

From the comparison of the noise level of phonon and light detectors in the data samples collected in the Gran Sasso facility, the latter have been observed to show a more unfavourable signal to noise ratio as can be seen from figure 6.5 and 6.6.
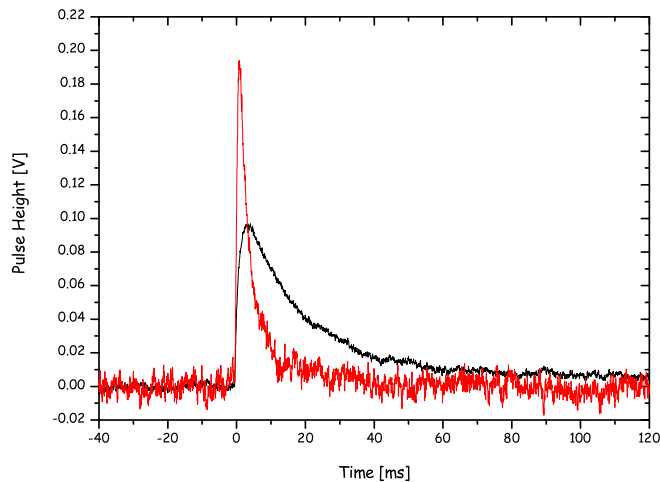

Figure 6.5: Coincident signals in the module Daisy/BE13. The black line is the measured signal in the phonon detector corresponding to about 30 keV energy deposition.
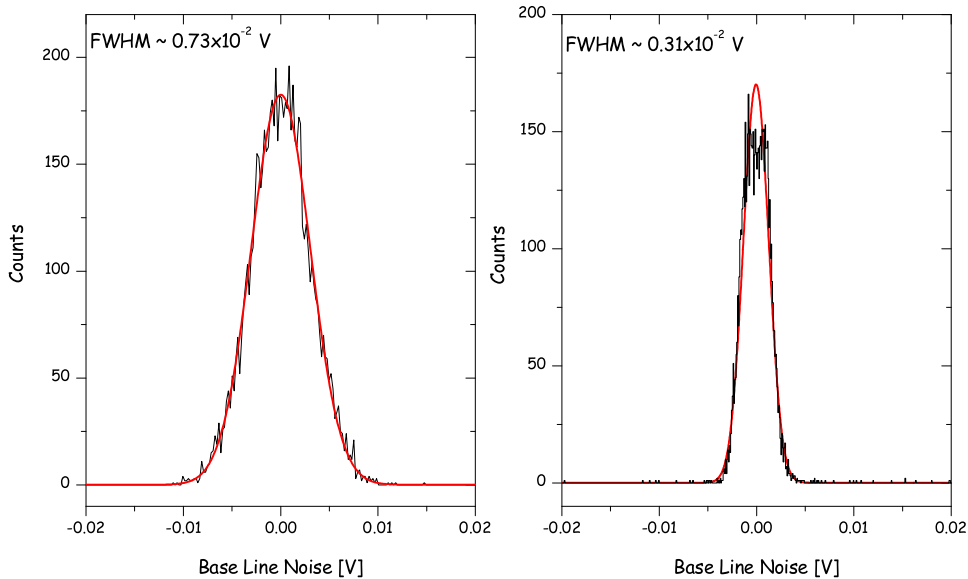
Figure 6.6: Spectrum of the random base line samples plotted over pulse height for the light detector BE13 (left) and for the phonon detector Daisy (right) measured in the Gran Sasso facility. The gaussian fit of the distribution is superimposed.

The worse performance of the more sensitive detector suggests that the observed noise is dominated by energy like sources. Furthermore the absolute measured noise level, which in the case of the light detector BE13 corresponds to about $1.4\,\mathrm{keV}_{ee} \approx 14\,\mathrm{eV}$ [2], is above all the contributions expected by the known fundamental sources[3].

This observed energy like excess noise deserves a systematic investigation in order to understand its origin and possibly cure it. This would allow a significant improvement of the detector performances [Sei04] [Gal04b].

Resolution

The energy resolution of light detectors plays an important role in the performance of a detector module because it determines the discrimination threshold of a CRESST II detector module. The resolution of the light detector defines the width of the different bands which correspond to the various types of interaction in the scintillating absorber and, therefore, the energy in the phonon detector below which they merge rendering the discrimination inefficient.

---

[2]The better performance with respect to the value reported in section 5.4.3 has to be ascribed to the different measuring setup.

[3]An excess noise that cannot be explained by the fundamental sources has been observed by many groups [BT01] [Lin01] [Gal04a].
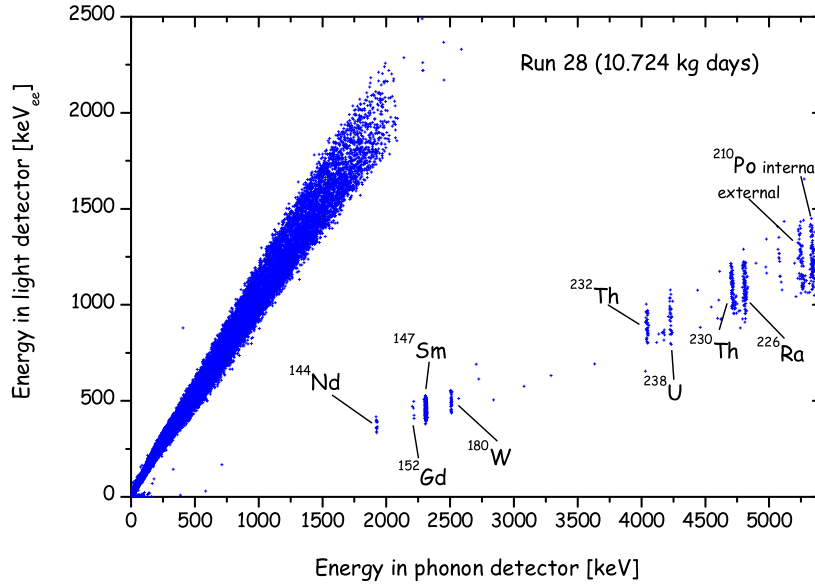
Figure 6.7: Energy in the light detector versus energy in the phonon detector measured in the Gran Sasso setup. The upper band comes from γ and β interactions in the $CaWO_4$ crystal whereas the lower band shows peaks produced by α interactions. The observed α peaks are identified and discussed in detail in [Coz04].

The observed resolution of light detectors when used in a detector module reflects not only the performance of the detector itself but also fluctuations of the light production[4] and collection.

The widening of the upper band of figure 6.7 with energy is due to an almost linear dependence of the light detector resolution with energy. This may be a result of a slight dependence of the light output with respect to the position of the energy deposition within the $CaWO_4$ crystal. To extract the energy dependence of the resolution of the light detectors used in Gran Sasso, data from a ^{232}Th calibration have been used (see figure 6.8). In this data set the low energy continuum is due to Compton scattered high energetic γ which interact uniformly in the crystal volume, as expected for nuclear recoils induced by neutrons and WIMPs. The light detector resolution is modelled in the energy range $0-300\,\mathrm{keV}$ by the power series

$$\Delta E = \sum_{i=0}^{3} A_i E^i \tag{6.1}$$

and the coefficients have been extracted from the thorium calibration data set. Results are shown in table 6.1.

---

[4]In the measurement performed with a photomultiplier setup the energy resolution achieved has been observed to strongly depend on the crystal sample [Nin05].
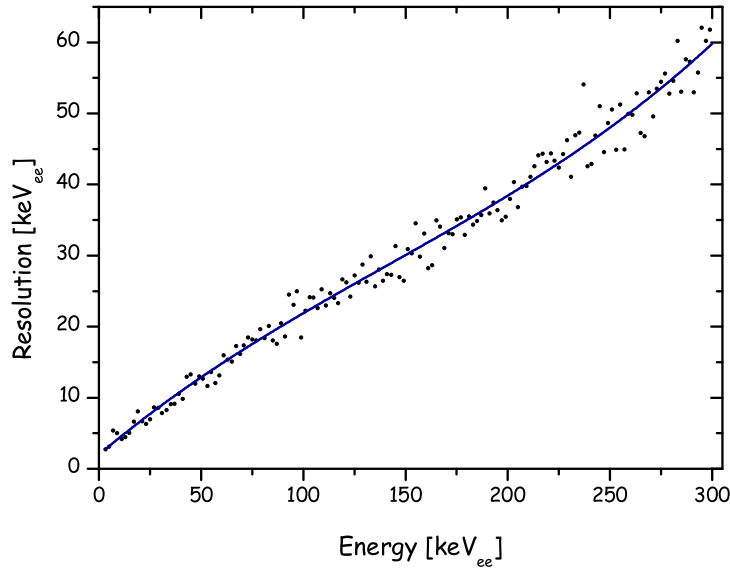
Figure 6.8: Resolution of the light detector BE13 as a function of energy in a ^{232}Th calibration. The full line shows the result of the fit used to compute the coefficients of the polynomial parametrization 6.1.

Light detector	A_0 [keV$_{ee}$]	A_1	A_2 [keV$_{ee}^{-1}$]	A_3 [keV$_{ee}^{-2}$]
BE13	1.974	0.24347	-0.5794$\times10^{-3}$	0.1368$\times10^{-5}$
BE14	3.446	0.24218	-0.1617$\times10^{-3}$	-0.7127$\times10^{-5}$

Table 6.1: Coefficients of the parametrization 6.1 of the light detector resolution extracted from the thorium calibration performed in the Gran Sasso setup.

The light detector BE13 shows a better energy resolution as indicated by the smaller value of A_0. The energy resolution at zero energy represents the final limitation due to the detector noise and is in good agreement with the energy resolution of heater pulses shown in figure 6.9.

The light detector resolution modelled by the sum in equation 6.1 is assumed to be independent of the energy deposition mechanism. The validity of the statement can be checked by comparing the light detector resolution for the different bands visible in figure 6.7 at the same light output. Doing this at the nominal light output of $484\,$keV$_{ee}$, corresponding to the α line at $2.31\,$MeV, the light detector resolution is $64 \pm 7\,$keV and $77 \pm 8\,$keV for the α and γ/β bands respectively.
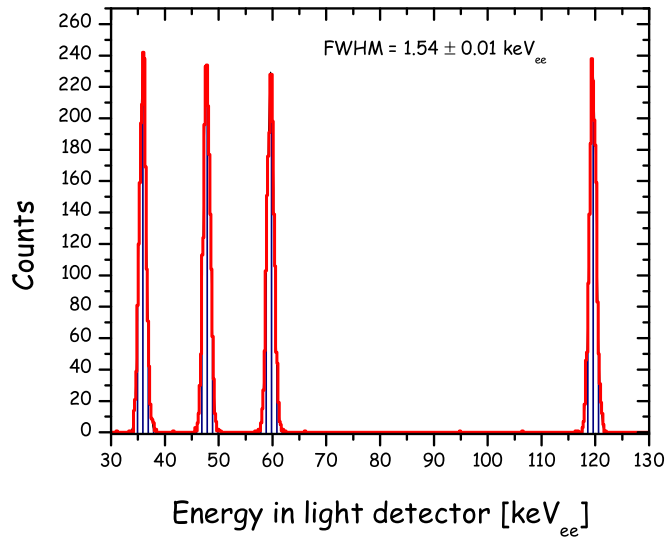
Figure 6.9: Gaussian fit of heater pulses of different energies injected in the light detector BE13. From the fit a FWHM of $1.54 \pm 0.01 \, \text{keV}_{ee}$ is calculated.

6.2 Dark Matter results

Competitive limits on WIMP Dark Matter using the active background suppression technique have been achieved using a data sample collected during a running period of 53 days with two detector modules in the Gran Sasso facility. The two CaWO$_4$ crystals Julia and Daisy were associated with light detectors BE14 and BE13 respectively. In table 6.2 relevant parameters of the measuring period are summarized.

Module	Measuring time [days]	Dead time [days]	Stability cut [days]	Mass [g]	Exposure [kg days]
Julia/BE14	37.572	3.391	0.518	291.4	9.809
Daisy/BE13	39.043	3.469	0.621	306.8	10.724

Table 6.2: Measurement time and exposure of detector modules in Run 28.

The data acquisition system has been described in section 4.1. In the specific case of this running period each trigger introduced a dead time of about 70 ms to allow the read out of the digitizer and the sampling of the next pre-trigger period.

The stability in the operating point was kept via the two control loops monitoring baseline and pulse height of heater pulses. The periods with significant deviation from the operating point were cut from the data sample ("stability

cut" in table 6.2).

Detectors were calibrated at the beginning of the data taking period with a ^{57}Co source and at the end of it with a ^{232}Th source. The latter allowed the energy dependence of the light detectors resolution to be tested, along with the reliability of the truncated fit procedure [Ang05] described in section 4.4.1 that is applied for the study of the α background of the detectors. The analysis of the low energy part of the spectrum that is of interest for Dark Matter limits does not involve the truncation procedure.

The accuracy of the energy calibration of phonon detectors in the energy range of interest for WIMP-nucleus scattering is of the order of few percent[5]; this is consistent with the accuracy of the analog square-rooter used to inject heater pulses. The tendency to slightly overestimate the energy of events leads to an overestimation of the actual threshold and, due to the quasi-exponential decreasing of the WIMP signal as a function of the recoil energy, to the assignment of a higher scale factor to the expected energy spectrum[6] in order to reproduce the measured one. As a consequence Dark Matter limits are moved towards conservative estimates.

The hardware threshold of phonon detectors was set to an energy of about 5 keV and 100% trigger efficiency was confirmed during the Dark Matter data taking period by means of the low energy heater pulses.

The data sample collected for the two modules is presented in figure 6.10 where the low energy region is shown in scatter plots of light energy to phonon energy ratio versus phonon energy. The points with negative energy arise from the fitting of pulses close to the noise.

6.2.1   WIMP exclusion limits

The determination of the acceptance band of WIMP interactions requires the knowledge of the energy resolution of the light and phonon detectors and of the quenching factor for nuclear recoils.

Using a quenching factor of 7.4 as determined in the course of the proof-of-principle experiment (see section 2.3.1[7]) and taking into account the resolution of the two detectors, the red lines in the scatter plots of figure 6.10 are obtained[8].

---

[5]At 46.54 keV the calibration with heater pulses is 1.2% too high [Ang05].

[6]The shape of the expected energy spectrum due to WIMPs is known with the exception of the normalization.

[7]Data have been reanalyzed recently [Ang05] using the template fit procedure yielding a slightly higher quenching factor with respect to the value of 7.4 stated in [Meu99]. The approach of using the lower value has been chosen for conservativeness.

[8]For each energy in the phonon detector the value expected in the light detector for the considered quenching factor is calculated. The resolution of the two detectors is taken into account summing quadratically (the two contributions are independent) the resolution of the phonon detector divided by the considered quenching factor and the resolution of the light
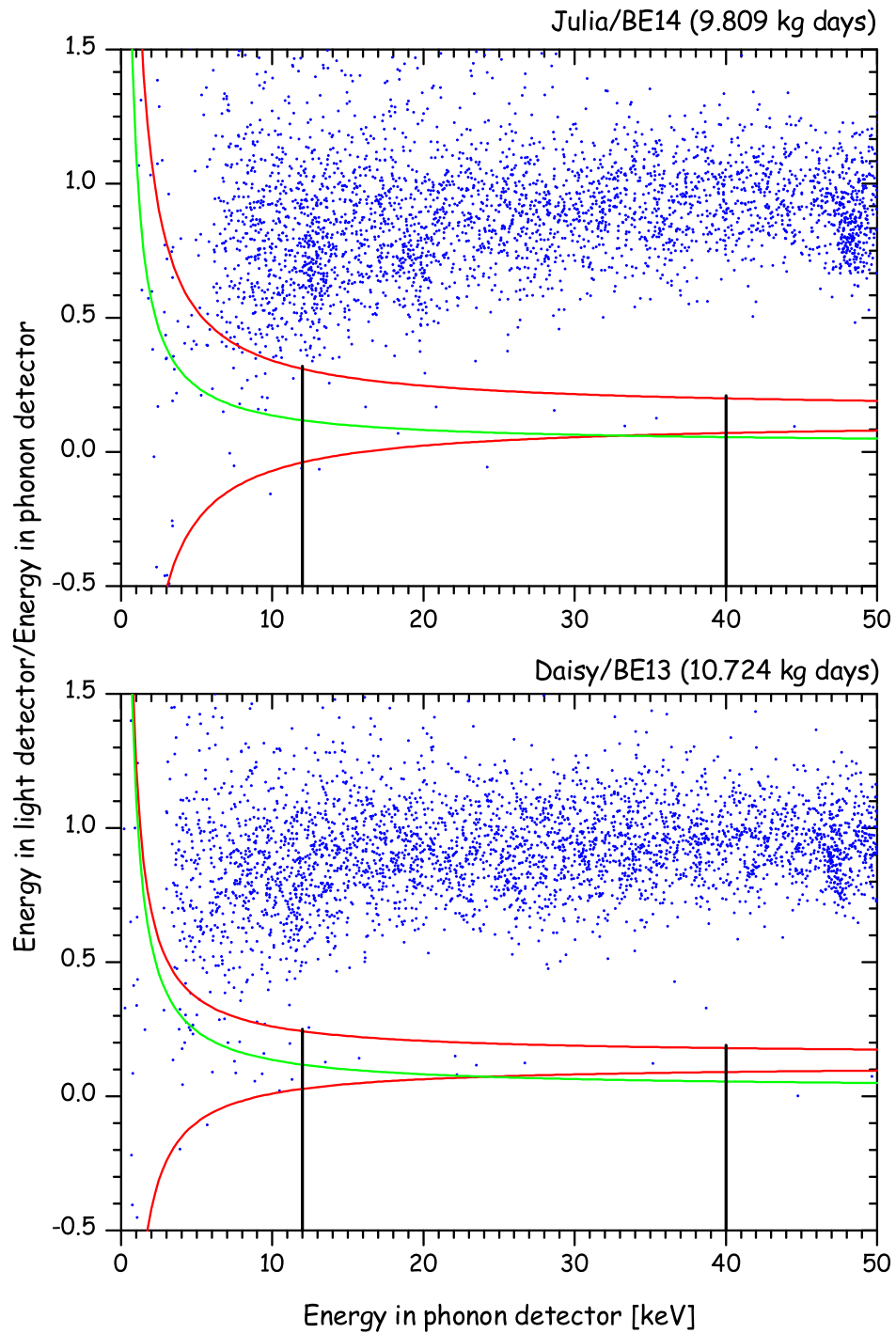
Figure 6.10: Low energy event distribution from the data sample collected in Run 28. Assuming a quenching factor of 7.4 for nuclear recoils, the regions below the upper red lines contain 90% of the nuclear recoils while the lower ones represent the 10% boundary. Assuming a quenching factor of 40 for tungsten recoils, 90% of these events are expected in the region below the green lines. The vertical lines delimit the energy range used in the analysis.

The upper lines represent the boundary below which 90% of nuclear recoils with quenching factor of 7.4 are expected, while the lower ones mark the 10% boundary.

The energy threshold of the acceptance region is determined by the discrimination threshold of the detector module. In the specific case of the data sample from Run 28 the analysis threshold has been set at 12 keV in order to be well above the energy where γ and recoil bands merge. The upper limit of the energy range is constrained by the physics of the interaction, namely by the vanishing of the expected energy spectrum in $CaWO_4$ at recoil energies of about 40 keV (see figure 1.5).

In the nuclear recoils acceptance region identified according to these criteria there are a total of 16 events for the two modules. Attributing all observed nuclear recoils to WIMP interactions, the resulting event rate for WIMP-nucleus elastic scattering for $12\,keV \leq E_r \leq 40\,keV$ is

$$R = (0.87 \pm 0.22)/(kg \cdot day) \qquad (6.2)$$

where a correction is applied to compensate the effect of the 90% boundary of the acceptance region. The quoted error is purely statistical. Systematic effect have been studied checking the stability of the result with respect to variation of the quenching factor [Ang05].

Since the quenching factor value used has been obtained from neutron induced nuclear recoils, the neutron background is expected in the region between the red lines. Furthermore, Monte Carlo simulations of the CRESST setup [Wul04a] without neutron shield give an estimate for the neutron background of about 0.6 events/(kg·day) in the energy range $12\,keV \leq E_r \leq 40\,keV$, suggesting that the observed rate is to be ascribed to neutron background.

The information on the expected neutron background in not used in the analysis where all the observed nuclear recoils, yielding to the rate in equation 6.2, are attributed to WIMP interactions. To suppress the neutron background the final experimental setup will include a neutron moderator and a muon veto.

To extract WIMP exclusion limits, the energy spectrum of nuclear recoils observed in the acceptance region has to be convolved with the energy resolution of the detector and then compared with the theoretical one. In the analysis of the data sample of Run 28, the expected spectrum for spin independent interaction is calculated assuming the standard Dark Matter halo model described in section 1.3.1 and the parametrization of the nuclear form factor described in [Lew96]. Using the optimum interval method [Yel02] for deciding the compatibility of expected and observed spectra, the dashed line in figure 6.11 is obtained [Ang05]. The result is stable with respect to the data sample used as can be seen in figure 6.12 from the exclusion limits obtained using the data sample of each detector module separately.

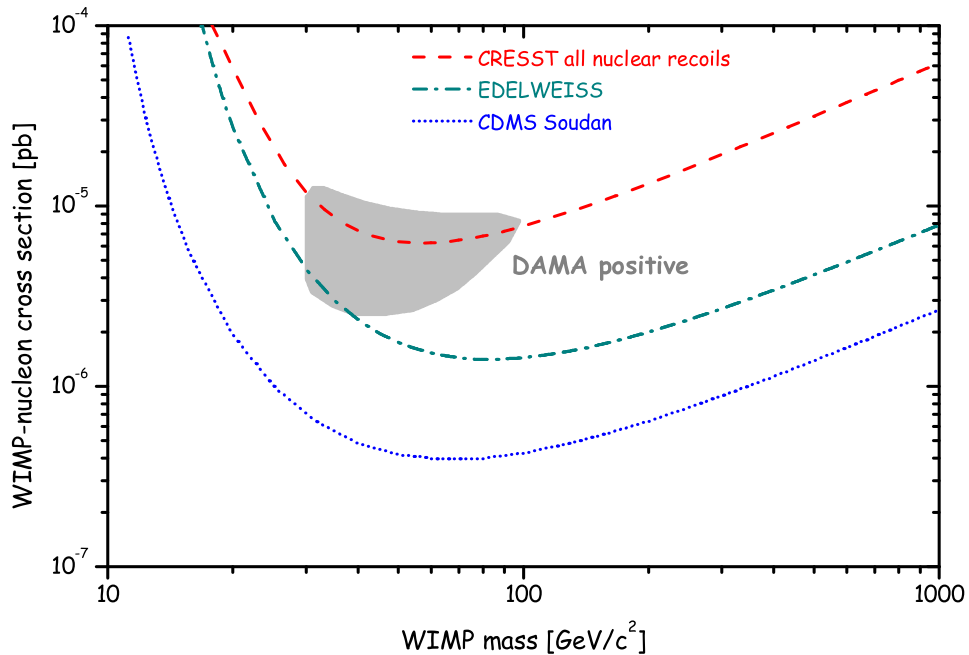detector, the latter being the leading term.

Figure 6.11: Spin independent WIMP-nucleon cross section limits at 90% C.L. as a function of the WIMP mass obtained from the data sample of Run 28 attributing all observed nuclear recoils to WIMP interactions. For comparison recent limits from the EDELWEISS Dark Matter search [Cha04], obtained with an exposure of 30.5 kg days of germanium, and from the CDMS experiment [col04b], corresponding to an exposure of 52.6 raw kg days of germanium in the final setup with neutron moderator and muon veto, are shown. The filled region indicates the DAMA evidence [Ber04].

The quenching factor experiment

As already mentioned in a previous chapter, there is the possibility to further exploit the active discrimination technique in order to distinguish between neutron interactions, mainly causing oxygen and calcium recoils[9], and WIMP interactions that mainly scatter off tungsten nuclei. This possibility requires the knowledge of the quenching factor for different recoiling nuclei. With the dedicated experiment introduced in section 2.3.1 a quenching factor of 40 ± 5 has been determined for tungsten nuclei (see figure 2.11).

The measured value is supported by the quenching factor that can be inferred from the background events due to ^{210}Po surface contamination observed in the data sample collected during Run 27 (see section 6.1). The data sample is plotted in figure 6.13 as light energy to phonon energy ratio versus phonon energy.

---

[9]For kinematic reasons neutrons with the spectrum measured in the Gran Sasso underground laboratory produce recoils in the interesting energy range mainly on oxygen nuclei.
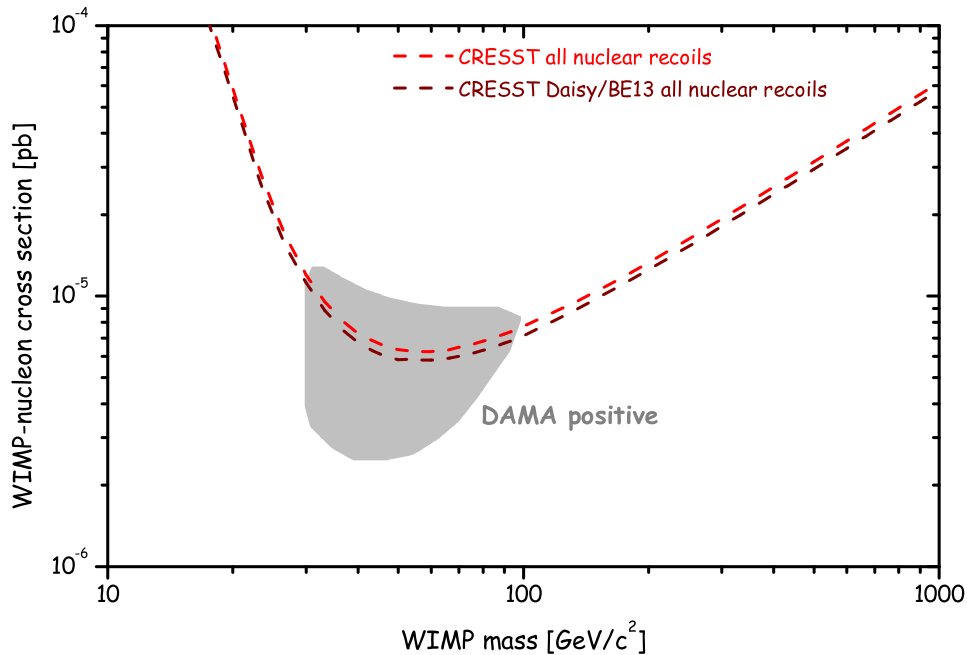
Figure 6.12: Spin independent WIMP-nucleon cross section limits at 90% C.L. as a function of the WIMP mass obtained from the data sample of Run 28 attributing all observed nuclear recoils to WIMP interactions. The two lines are obtained from the complete data sample (red) and from the module Daisy/BE13 alone (maroon). The filled region indicates the DAMA evidence.

Ascribing the group of events between 80 and 110 keV to α decays of ^{210}Po atoms from which only the daughter nucleus ^{206}Pb reaches the crystal, the quenching factor for ^{206}Pb can be estimated from the light yield of these events. The obtained value of 48.7 ± 7.1 is in good agreement with the previous result and with the observed systematic increase of the quenching factor with the mass of the recoiling nucleus. The events appearing at about the same value of the ratio between energy in the light detector and energy in the phonon detector indicates that the quenching factor is independent of the recoil energy.

Using a quenching factor of 40 to determine the acceptance band for WIMP interactions (i.e. limiting the attention to tungsten recoils) the boundary below which 90% of tungsten recoils are expected is represented by the green lines in figure 6.10. The detector module Daisy/BE13 shows zero events in the energy interval of interest, while the module Julia/BE14 has three events.
The different behaviour of the two modules has to be ascribed to the different resolution of the light detectors. The better resolution of the light detector BE13 (see table 6.1) prevents the "leakage" of neutron induced events into the tungsten
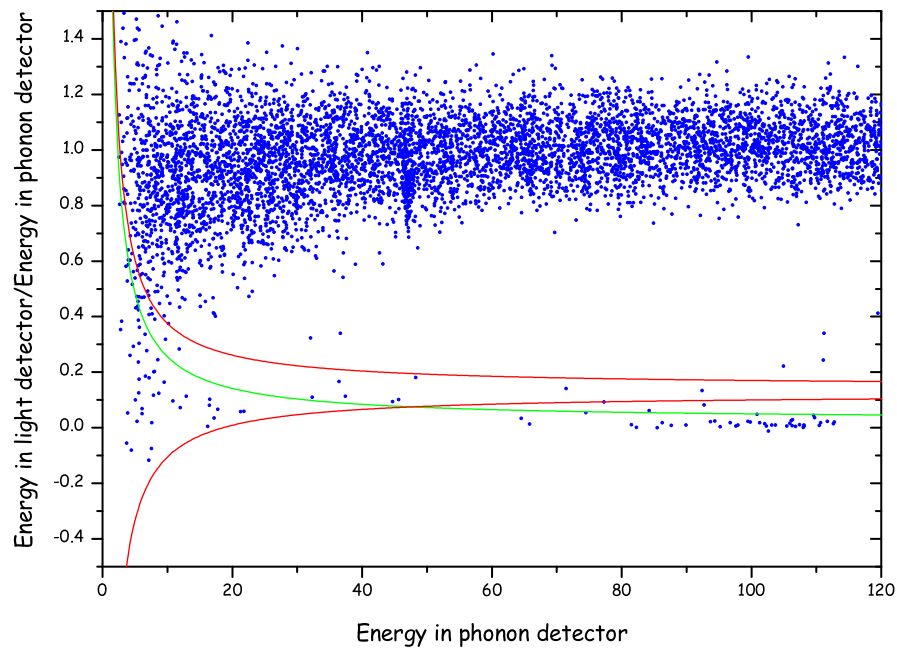
Figure 6.13: Energy distribution of events from the data sample collected in Run 27. The region below the upper red line contains 90% of the neutron induced nuclear recoils (quenching factor of 7.4) while the lower one represents the 10% boundary. The green line shows the boundary of the 90% acceptance region for nuclear recoils with quenching factor of 40.
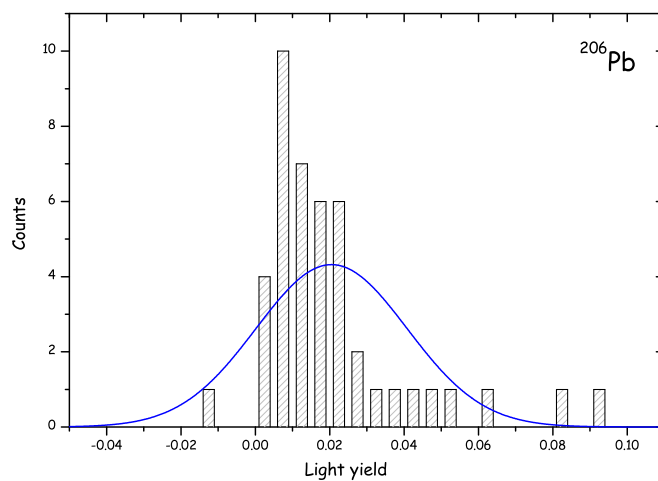
Figure 6.14: Light yield for ^{206}Pb recoils. From the gaussian fit a quenching factor of 48.7 ± 7.1 is calculated.

recoils acceptance region that may occur as a consequence of statistical fluctuations in the light detector. Using the known resolution of light detectors and assuming gaussian fluctuations, for each event in the neutron acceptance region it is possible to calculate the probability of it appearing in the tungsten recoils acceptance region[10]. This method leads to an estimated leakage of 1.1 events for the module Daisy/BE13 and of 3.6 events for the module Julia/BE14, indicating that the different resolution of the light detectors accounts for the different behaviour of the two modules.

Using the detector module Daisy/BE13 to set an exclusion limit on the spin independent WIMP-nucleus elastic scattering, the solid red line in figure 6.15 is obtained.

Systematic effects have been studied as before by checking the stability of the result with respect to the variation of the quenching factor and of the analysis threshold [Ang05].

The significantly more stringent limit obtained by applying the discrimination of the recoiling nucleus based on the knowledge of the quenching factor opens important possibilities for improving the experimental sensitivity, not only in terms of background suppression, but also concerning the possibility to verify a possible WIMP signal, offering a multiple target choice within a single absorber material.

As can be seen from the different behaviour of the two detector modules that have been running in the Gran Sasso facility, the successful application of the discrimination mainly depends on the performance of light detectors.

To this end further improvement of the light detectors is actively pursued.

6.3   Status

The data taking of Run 28 was halted on March 23$^{\rm rd}$ 2004 to proceed with the upgrade which, in addition to the completion of the shielding with the installation of neutron moderator and muon veto, will involve the installation of a 66 channel SQUID readout system to enable the operation of 33 detector modules for a total target mass of 10 kg.

As shown in figure 6.16, the expected sensitivity of the CRESST experiment with 30 kg·year of measurement covers significant regions of the parameter space allowed by several supersymmetric models.

---

[10]For each event in the neutron acceptance region the energy expected in the light detector for the considered quenching factor is calculated. This value is assumed to be the mean value of a gaussian distribution with width given by the light detector resolution as calculated from values in table 6.1; therefore the probability that each event would have appeared below the boundary of the tungsten acceptance region is calculated as the integral of the gaussian distribution below the boundary.
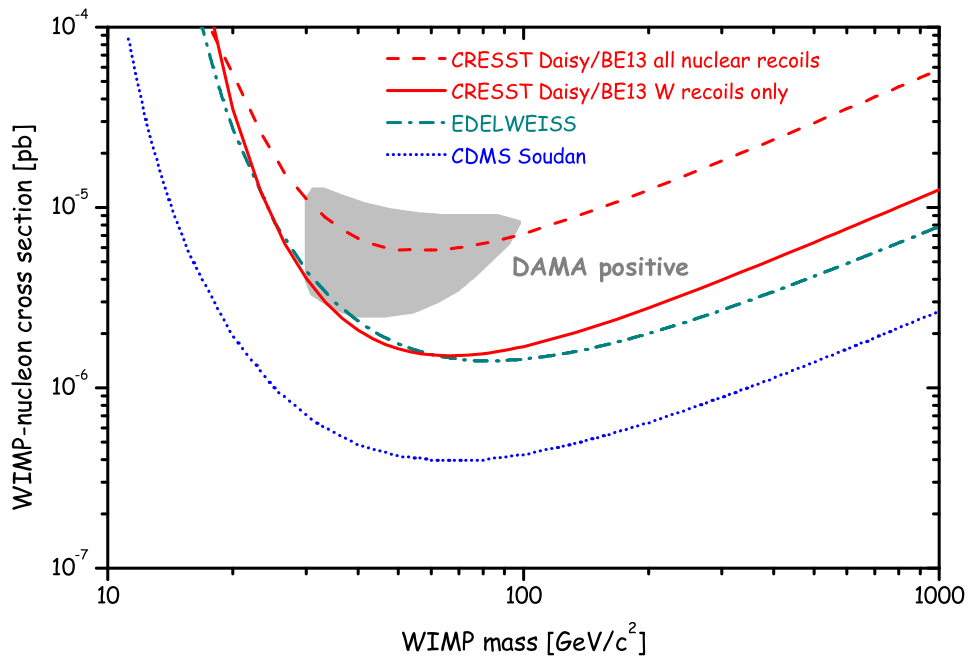
Figure 6.15: Spin independent WIMP-nucleon cross section limits at 90% C.L. as a function of the WIMP mass obtained from the data sample of the module Daisy/BE13 collected in Run 28. The dashed red line is obtained attributing all observed nuclear recoils to WIMP interactions whereas the solid line is obtained considering tungsten recoils only. For comparison recent limits from the EDELWEISS Dark Matter search [Cha04], obtained with an exposure of 30.5 kg days of germanium, and from the CDMS experiment [col04b], corresponding to an exposure of 52.6 raw kg days of germanium in the final setup with neutron moderator and muon veto, are shown. The filled region indicates the DAMA evidence [Ber04].
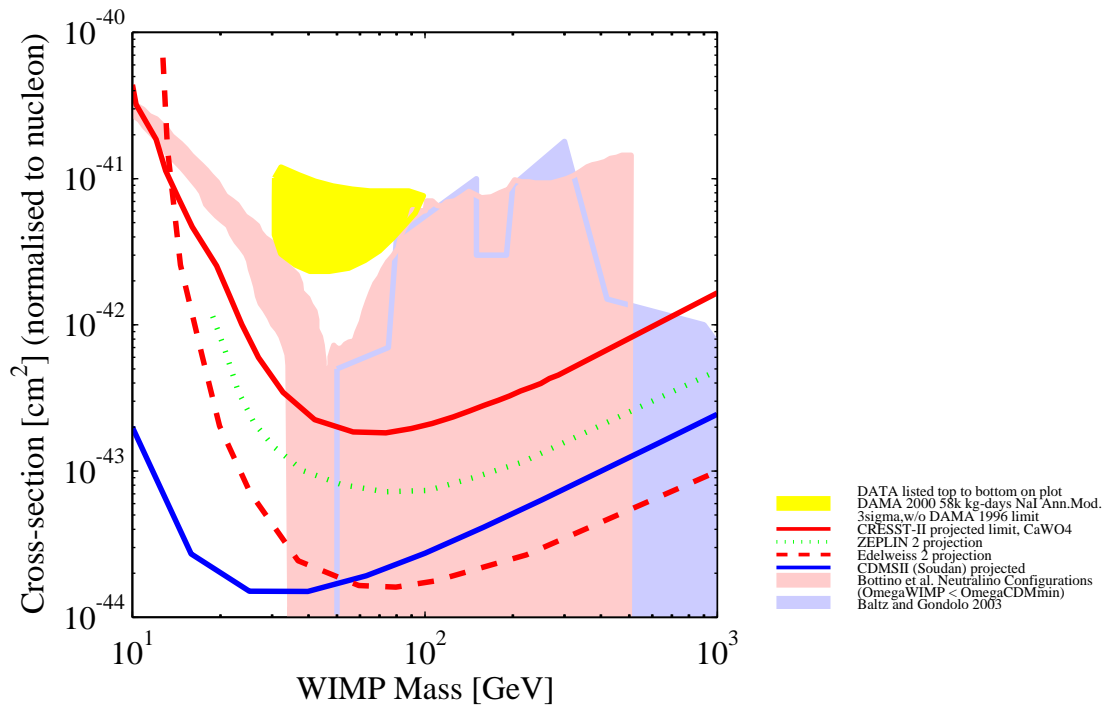
Figure 6.16: Projected sensitivity of some of the next generation experiments in the WIMP mass - cross section parameter space. These limits start to probe interesting regions of the parameter space allowed by several supersymmetric models. As an example allowed regions by [Bot04] (pink) and [Bal03] (light blue) are shown. The yellow region indicates the DAMA evidence. Figure from [Gai].

Chapter 7

Conclusions and Perspectives

The aim of the second phase of the CRESST experiment is to detect WIMP
Dark Matter particles via their elastic scattering off nuclei.
WIMP-nucleus elastic scattering event rates are expected to be less than one
event per day and per kg of detector mass; therefore the suppression of back-
ground that would hide or mimic the WIMP signal is of crucial importance.
Moreover, since the energy transferred to a nucleus in a WIMP-nucleus elastic
scattering is extremely low (a few tens of keV), the energy threshold and the sen-
sitivity of detectors are additional fundamental issues in a Dark Matter search.
Detectors developed for CRESST consist of a $300\,g$ $CaWO_4$ scintillating crystal
operated as a cryogenic calorimeter in close proximity to a second much smaller
cryogenic calorimeter used to detect the scintillation light produced in the target
crystal. Active background suppression is achieved by the simultaneous measure-
ment of a phonon and a light signal from the scintillating cryogenic calorimeter.

Only about 1% of the energy deposited in $CaWO_4$ by β or γ interactions can
be detected as scintillation light; therefore the sensitivity of light detectors is a
fundamental issue for the discrimination of electron recoils from nuclear recoils
at energies relevant for WIMP searches.
The main goal of this work was to develop extremely sensitive cryogenic calorime-
ters for the detection of the $CaWO_4$ scintillation light. This has been achieved
with a new thermometer geometry characterized by phonon collectors and a thin
film thermal coupling to the heat sink. This concept allows for a high sensitivity
by decoupling the area required for the collection of non-thermal phonons and
the heat capacity of the sensor, and permits to make the thermal relaxation time
of the thermometer long enough to allow the integration of the scintillation light,
despite the slow light emission of $CaWO_4$ at low temperature.
First results on the development of this new light detector concept have been
published in [Pet04].

In the course of this work extensive studies have been carried out in order to fully characterize light detectors used in Dark Matter runs. Results have been presented together with further options of improvements which are being actively pursued.
Simultaneously the testing of new materials to be used as substrates has begun and additional testing is ongoing.

A number of short runs have been performed in the Gran Sasso facility in order to optimize the detector modules allowing problems related with the scaling up of the proof-of-principle detector to be fixed and the thorough study of contaminations present in the crystals. Special attention was devoted to the detector holder and light reflector in order to get rid of spurious pulses observed in the phonon detector in the early runs without any associated light.

By means of the significantly improved sensitivity and signal quality obtained with the new generation of light detectors developed within this work, an efficient discrimination down to recoil energies of about $10\,\mathrm{keV}$ has been achieved during the prototyping period by the simultaneous detection of phonons and light. The analysis of measurements performed at the Gran Sasso facility during the prototyping period is presented with the first limits on WIMP Dark Matter obtained using the active background suppression technique and its extension based on the knowledge of the quenching factors of different nuclei.

The upgrade of the CRESST experimental setup will allow the installation of 33 detector modules for a total target mass of $10\,\mathrm{kg}$. Together with the recently installed neutron shield and muon veto this should enhance the sensitivity to WIMP interactions by two orders of magnitude. The method developed for identifying the recoiling nuclei offers a multiple target choice within one absorber material enhancing as a consequence the detector sensitivity. In the case of a positive signal a unique signature will be provided comparing rates and spectra in different absorber materials.

Bibliography

[Abr02]   D. Abrams et al.,   Exclusion Limits on the WIMP-Nucleon Cross-Section from the Cryogenic Dark Matter Search, *Phys. Rev. D* 66(122003)

[Abu00]   R. Abusaidi et al., Exclusion Limits on the WIMP-Nucleon Cross Section from the Cryogenic Dark Matter Search, *Phys. Rev. Lett.* **84** (2000) 5699

[Alt01]   M. Altmann et al., Update of the Proposal to the LNGS for a Second Phase of the CRESST Dark Matter Search, February 2001

[Ang02]   G. Angloher et al., Limits on WIMP dark matter using sapphire cryogenic detectors, *Astropart. Phys.* **18** (2002) 43–55

[Ang04]   G. Angloher, private communication, 2004

[Ang05]   G. Angloher, et al., F. Petricca, Limits on WIMP dark matter using scintillating $CaWO_4$ cryogenic detectors with active background suppression, *Accepted for publication in Astropart. Phys.*

[Apr04]   E. Aprile et al., In *Proceeding of 6th UCLA Symposium on Sources and Detection of Dark Matter and Dark Energy in the Universe*, 2004

[Arn99]   F. Arneodo et al., Neutron Background Measurements in the Hall C of the Gran Sasso Laboratory, *Nuovo Cim. A* **112** (1999) 819–831

[Arp92]   C. Arpesella, Background Measurements at Gran Sasso Laboratories, *Nucl. Phys. B (Proc. Suppl.)* **28A** (1992) 420

[Ash76]   N. W. Ashcroft, N. D. Mermin, *Solid State Physics*, Holt-Saunders International Editions, 1976

[Bah98]   N. A. Bahcall, X. Fan, The Most Massive Distant Clusters: Determining Ω and σ_8, *Ap. J.* **504** (1998) 1–6

[Bal03]   E. A. Baltz, P. Gondolo, Improved constraints on supersymmetric dark matter from muon g–2, *Phys. Rev. D* **67** (2003) 063503

[Bau99]   L. Baudis et al., New Limits on Dark Matter WIMPs from the Heidelberg-Moscow Experiment, *Phys. Rev. D* **59** (1999) 022001

[Bel85]   E. Bellotti et al., New Measurement of Rock Contaminations and Neutron Activity in the Gran Sasso Tunnel, *INFN/TC-85/19* (1985)

[Bel96]   A. de Bellefon et al., Dark matter search with a low temperature sapphire bolometer, *Astropart. Phys.* **6** (1996) 35–43

[Ben01]   A. Benoit et al., First results of the EDELWEISS WIMP search using a 320 g heat-and-ionization Ge detector, *Phys. Lett. B* **513** (2001) 15–22

[Ben02]   A. Benoit et al., Improved Exclusion Limits from the EDELWEISS WIMP Search, *Phys. Lett. B* **545** (2002) 43–49

[Ber96]   R. Bernabei et al., Search for WIMP annual modulation signature: results from DAMA/NaI-3 and DAMA/NaI-4 and the global combined analysis, *Phys. Lett. B* **389** (1996) 757

[Ber00]   R. Bernabei et al., Search for WIMP annual modulation signature: results from DAMA/NaI-3 and DAMA/NaI-4 and the global combined analysis, *Phys. Lett. B* **480** (2000) 23

[Ber03]   R. Bernabei et al., Dark Matter search, *Riv. N. Cim.* **26(1)** (2003) 1–73

[Ber04]   R. Bernabei et al., DAMA/NaI results, *Preprint* **astro-ph/0405282** (2004)

[Ber05]   G. Bertone, D. Hooper, J. Silk, Particle Dark Matter: Evidence, Candidates and Constraints, *Phys. Rept.* **405** (2005) 279–390

[Bin87]   J. Binney, S. Tremaine, *Galactic Dynamics*, Princeton University Press, 1987

[Bir67]   J. B. Birks, *Theory and Practice of Scintillation Counting*, Pergamon, 1967

[Bla83]   G. Blasse, G. Bokkers, Low-Temperature Decay-Time Measurements on the Luminescence of Calcium Tungstate, *J. Solid State Chem.* **49** (1983) 126–128

[Bot97]   A. Bottino et al., Exploring the Supersymmetric Parameter Space by Direct Search for WIMPs, *Phys. Lett. B* **402** (1997) 113

[Bot04]   A. Bottino et al., Light neutralinos and WIMP direct searches, *Phys. Rev. D* **69** (2004) 037302

[BT01]   W. M. Bergmann Tiest et al., In F. S. Porter, D. McCammon, M. Galeazzi, Stahle C. K., editors, *Low Temperature Detectors*, volume 605 of *AIP conference proceedings*, p. 199, 2001

[Buc04]   C. Bucci, private communication, 2004

[Büh96]   M. Bühler et al., Status and Low Background Considerations for the CRESST Dark Matter Search, *Nucl. Instr. and Meth. A* **370** (1996) 237

[Car99]   R.G. Carlberg et al., The $\Omega_m - \Omega_\Lambda$ Dependence of the Apparent Cluster Ω, *Ap. J.* **516** (1999) 552

[Cha04]   G. Chardin et al., Latest results from the EDELWEISS WIMP search, *Nucl. Instr. Meth. A* **520** (2004) 101–104

[Chi79]   C. C. Chi, J. Clarke, Quasiparticle branch mixing rates in superconducting aluminium, *Phys. Rev. B* **19(9)** (1979) 4495–4509

[Cla89]   J. Clarke, In *Proceedings of the IEEE*, volume 77, 1989

[col03]   WMAP collaboration, First Year Results from WMAP, *Ap. J. S.* 148(1)

[col04a]   CAST collaboration, First results from the CERN Axion Solar Telescope, *submitted for pubblication to Phys. Rev. Lett.* **hep-ex/0411033** (2004)

[col04b]   CDMS collaboration, First Results from the Cryogenic Dark Matter Search in the Soudan Underground Lab, *Phys. Rev. Lett.* **93** (2004) 211301

[Cop96]   C. J. Copi, D. N. Schramm, The Nuclear Impact on Cosmology: The $H_0 - \Omega$ Diagram, *Comm. Nucl. Part. Phys.* **22** (1996) 1

[Cop03]   C.J. Copi, L.M. Krauss, Comparing WIMP Interaction Rate Detectors with Annual Modulation Detectors, *Phys. Rev. Lett.* **67** (2003) 103507

[Coz04]   C. Cozzini, et al., F. Petricca, Detection of the Natural Alpha Decay of Tungsten, *Phys. Rev. C* **70** (2004) 064606

[Dav85]   M. Davis et al., The Evolution of Large Scale Structure in a Universe Dominated by Cold Dark Matter, *Ap. J.* **292** (1985) 371–394

[Die79]   W. Dietsche, H. Kinder, Spectroscopy of Phonon Scattering in Glass, *Phys. Rev. Lett.* **43(19)** (1979) 1413–1417

[DiS03]   P. DiStefano et al., Textured Silicon Calorimetric Light Detector, *J. Appl. Phys.* **94(10)** (2003) 6887

[DiT92]   J. F. DiTusa et al., Role of phonon dimensionality on electron-phonon scattering rates, *Phys. Rev. Lett.* **68** (1992) 1156–1159

[dmf]   The Future of Dark Matter Detection Workshop Web Page: http://kicp.uchicago.edu/workshops/dmd2004/

[Dug77]   J. S. Dugdale, *The electrical properties of metals and alloys*, Edward Arnold, 1977

[Eng92]   J. Engel, Nuclear Form Factors for the Scattering of Neutralinos, *Nucl. Phys. B (Proc. Suppl.)* **28A** (1992) 310–313

[Fen01]   J. L. Feng et al., Prospects for indirect detection of neutralino dark matter, *Phys. Rev. D* **63** (2001) 045024

[Fra02]   T. Frank, *Development of Scintillating Calorimeters for Discrimination of Nuclear Recoils and Fully Ionizing Events*, PhD thesis, Technische Universität München, 2002

[Fre88]   K. Freese et al., Signal Modulation in Cold Dark Matter Detection, *Phys. Rev. D* **37** (1988) 3388

[Gai]   R. Gaitskell, V. Mandic, Direct Detection of WIMP Dark Matter, Sensitivity Plots, web link http://dmtools.berkeley.edu/limitplots/

[Gal03]   M. Galeazzi, D. McCammon, Microcalorimeter and bolometer model, *J. Appl. Phys.* **93** (2003) 4856

[Gal04a] M. Galeazzi, Performance of resistive microcalorimeters and bolometers, *Nucl. Instr. and Meth. A* **520** (2004) 320–324

[Gal04b] M. Galeazzi et al., Intrinsic noise sources in superconductors near the transition temperature, *Nucl. Instr. and Meth. A* **520** (2004) 344–347

[Gam46]   G. Gamow, Expanding Universe and the Origin of Elements, *Phys. Rev.* **70** (1946) 572

[Gam48a] G. Gamow, The Origin of Elements and the Separation of Galaxies, *Phys. Rev.* **74** (1948) 505

[Gam48b] G. Gamow et al., The Evolution of the Universe, *Nature* **162** (1948) 774

[Gat95]   E. I. Gates, G. Gyuk, M. S. Turner, The Local Halo Density, *Ap. J. L.* **449** (1995) 123

[GB99a]   J. Garcia-Bellido, Astrophysics and Cosmology, *Casta-Papiernicka 1999, High-energy physics* **ESHEP 99** (1999) 109–186

[GB99b]   J. Garcia-Bellido, The Origin of Matter and Structure in the Universe, *Phil. Trans. Roy. Soc. Lond. A* **357** (1999) 3237–3257

[GG03]   M. C. Gonzales-Garcia, Y. Nir, Neutrino masses and mixing: evidence and implications, *Rev. Mod. Phys.* **75** (2003) 345

[Glu73]   M. Gluyas, F. D. Huges, B.W. James, The Elastic Constants of Calcium Tungstate, *J. Phys. D: Appl. Phys.* **6** (1973) 2025–2037

[GM89]   L. Gonzales-Mestres, D. Perret-Gallix, Detection of Low Energy Solar Neutrinos and Galactic Dark Matter with Crystal Scintillators, *Nucl. Instr. and Meth. A* **279** (1989) 382–387

[Gon04]   P. Gondolo, Introduction to Non-Baryonic Dark Matter, *Lectures delivered at the NATO Advanced Study Institute "Frontiers of the Universe", 8-20 Sept 2003, Cargese,* astro–ph/0403064

[Goo85]   M. W. Goodman, E. Witten, Detectability of certain Dark Matter candidates, *Phys. Rev. D* **31** (1985) 3059

[Gre02]   A. M. Green, Calculating Exclusion Limits for WIMP Direct Detection Experiments without Background Subtraction, *Phys. Rev. D* **65** (2002) 023520

[Har79]   J. P. Harrison, Heat Transfer Between Liquid Helium and Solids Below 100 mK, *J. Low Temp. Phys.* **37** (1979) 467–565

[Har02]   S. P. Hart et al., Status of dark matter searches in the Boulby mine, *Nucl. Phys. B (Proc. Suppl.)* **110** (2002) 91–93

[Hau05]   D. Hauff, private communication, 2005

[Hoe02]   H. Hoekstra et al., Current status of weak gravitational lensing, *New Astron. Rev.* **46** (2002) 767

[Hsi68]   S. Y. Hsieh et al., Diffusion of quasiparticles in superconducting aluminium films, *Phys. Rev. Lett.* **20(26)** (1968) 1502–1504

[hub]   Hubble Space Telescope Web Page:
            http://hubblesite.org

[Hub29]   E. P. Hubble, A relation between distance and radial velocity among extragalactic nebulae, *Publ. Nat. Acad. Sci.* **15** (1929) 168

[Ira02]   Igor G. Irastorza et al., Present status of IGEX dark matter search at Canfranc Underground Laboratory

[Jun96]   G. Jungman, M. Kamionkowski, K. Griest, Supersymmetric Dark Matter, *Phys. Rep.* **267** (1996) 195

[Kap76]   S. B. Kaplan et al., Quasiparticle and phonon lifetimes in superconductors, *Phys. Rev. B* **14(11)** (1976) 4854–4873

[Kas98]   A. Kashlinsky, Determining Ω from the cluster correlation function, *Phys. Rep.* **307** (1998) 67–73

[Kee02]   R. Keeling, *Studies of Scintillators for the CRESST Dark Matter Search*, PhD thesis, University of Oxford, 2002

[Ker86]   F. J. Kerr, D. Lynden-Bell, Review of galactic constants, *Mon. Not. Roy. Astron. Soc.* **221** (1986) 1023

[Kha02]   S. Khalil, C. Munoz, The Enigma of the Dark Matter, *Contemp. Phys.* **43** (2002) 51–62

[Kit67]   C. Kittel, *Introduction to Solid State Physics*, John Wiley and Sons, third Edition, 1967

[Kna85]   W. Knaak et al., In J. P. Wolfe A. C. Anderson, editor, *Phonon Scattering in Condensed Matter: Proceedings of the Fifth International Conference.*, Springer Series in Solid-State Science, pp. 174–176. Springer Verlag, 1985

[Kno03]   R. A. Knop et al., New Contraints on Ω_m, Ω_Λ, and w from an Independent set of 11 High-Redshift Supernovae Observed with the Hubble Space Telescope, *Ap. J.* **598** (2003) 102–137

[Kos92]   M. Koshiba, Observational neutrino astrophysics, *Phys. Rep.* **(220)** (1992) 229–381

[Kur82]   M. Kurakado, Possibility of high resolution detectors using superconducting tunnel junctions, *Nucl. Instr. and Meth.* **196** (1982) 275–277

[Kur04]   A. Kurylov, M. Kamionkowski, Generalized analysis of weakly-interacting massive particle searches, *Phys. Rev. D* **69** (2004) 063503

[Lar66]   P. A. Larssen, Crystallographic Match in Epitaxy between Silicon and Sapphire, *Acta Cryst.* **20** (1966) 599–602

[Leo90]   P. J. T. Leonard, S. Tremaine, The local Galactic escape speed, *Ap. J.* **353** (1990) 486

[Lew96]   J. D. Lewin, P. F. Smith, Review of Mathematics, Numerical Factors, and Corrections for Dark Matter Experiments based on Elastic Nuclear Recoil, *Astropart. Phys.* **6** (1996) 87

[Lin01]   M. A. Lindeman et al., In F. S. Porter, D. McCammon, M. Galeazzi, Stahle C. K., editors, *Low Temperature Detectors*, volume 605 of *AIP conference proceedings*, p. 203, 2001

[Liu91]   J. Liu, N. Giordano, Electron-phonon scattering times in thin Sb films, *Phys. Rev. B* **43** (1991) 3928–3932

[Loi99]   M. Loidl, *Diffusion und Einfang von Quasiteilchen*, PhD thesis, Ludwig-Maximilians-Universität, München, 1999

[Loi01]   M. Loidl et al., Quasiparticle diffusion over several mm in cryogenic detectors, *Nucl. Instr. and Meth. A* **465** (2001) 440–446

[Mac55]   G. G. MacFarlane, V. Roberts, Infrared Absorption of Silicon Near the Lattice Edge, *Phys. Rev.* **98** (1955) 1865–1866

[Mar90]   H. J. Maris, Phonon propagation with isotope scattering and spontaneous anharmonic decay, *Phys. Rev. B* **41(14)** (1990) 9736–9743

[Mat82]   J. C. Mather, Bolometer noise: nonequilibrium theory, *Appl. Opt.* **21(6)** (1982) 1125–1129

[McC93]   D. McCammon et al., Thermal calorimeters for high resolution X-ray spectroscopy, *Nucl. Instr. and Meth. A* **326** (1993) 157–165

[Meu99]   P. Meunier et al., Discrimination between Nuclear Recoils and Electron Recoils by Simultaneous Detection of Phonons and Scintillation Light, *Appl. Phys. Lett.* **75(9)** (1999) 1335

[Mos84]   S. H. Moseley, J. C. Mather, D. McCammon, Thermal detectors as x-ray spectrometers, *J. Appl. Phys.* **56(5)** (1984) 1257–1262

[Nar78]   V. Narayanamurti et al., Quasiparticle and phonon propagation in bulk, superconducting lead, *Phys. Rev. B* **18(11)** (1978) 6041–6052

[Nin04a]   J. Ninković, private communication, 2004

[Nin04b]   J. Ninković et al., to be published

[Nin05]   J. Ninković,   *Investigation of CaWO₄ Crystals for Simultaneous Phonon-Light Detection in the CRESST Dark Matter Search*, PhD thesis, Technische Universität München, 2005

[Pec77]   R.D. Peccei, H.R. Quinn, CP Conservation in the Presence of Pseudoparticles, *Phys. Rev. Lett.* **(38)** (1977) 1440

[Pen65]   A. A. Penzias, R. W. Wilson, A Measurement of Excess Antenna Temperature at 4080 mc/s, *Ap. J.* **142** (1965) 419–421

[Pet04]   F. Petricca et al., Light detector development for CRESST II, *Nucl. Instr. and Meth. A* **520** (2004) 193–196

[Pip55]   A. B. Pippard, Ultrasonic Attenuation in Metals, *Philos. Mag.* **46** (1955) 1104–1114

[Pob92]   F. Pobell, *Matter and Methods at Low Temperatures*, Springer-Verlag, 1992

[Pri96]   J.R. Primack, In A. Deckel, J. P. Ostriker, editors, *Formation of Structure in the Universe*, p. 1, Proceedings of Jerusalem Winter School, 1996. Cambridge University Press

[Prö95]   F. Pröbst et al., Model for Cryogenic Particle Detectors with Superconducting Phase Transition Thermometers, *J. of Low Temp. Phys.* **100** (1995) 69

[Raf97]   G. G. Raffelt, In *Proceedings of the 1997 European School of High-Energy Physics, Menstrup near Naestved, Denmark*, 1997

[RI78]   A. C. Rose-Innes, E. H. Rhoderick, *Introduction to Superconductivity*, volume 6 of *International series in solid state physics*, Pergamon Press, second Edition, 1978

[Ros00]   L. J. Rosenberg, van Bibber K. A., Searches for invisible axions, *Phys. Rept.* **325** (2000) 1

[Sei04]   G. M. Seidel, I. S. Beloborodov, Intrinsic excess noise in a transition edge sensor, *Nucl. Instr. and Meth. A* **520** (2004) 325–328

[Sim71]   G. Simmons, H. Wang, *Single Crystal Elastic Constants and Calculated Aggregate Properties: A HANDBOOK*, The M.I.T. Press, second Edition, 1971

[Sol72]   L. Solymar, *Superconductive Tunneling and Applications*, Chapman and Hall, 1972

[Spe03]   D. N. Spergel et al., First Year Wilkinson Microwave Anisotropy Probe (WMAP) Observations: Determination of Cosmological Parameters, *Ap. J. S.* **148** (2003) 175

[Spi99]   M. Spiro, E. Aubourg, N. Palanque-Delabrouille, Baryonic Dark Matter, *Nucl. Phys. B (Proc. Suppl.)* **77** (1999) 402–419

[Spi00]   M. Spiro, E. Aubourg, N. Palanque-Delabrouille, Search for Galactic Dark Matter, *Physica Scripta* **T85** (2000) 254–258

[Spo00]   N. Spooner et al., NaI dark matter limits and the NAIAD array – a detector with improved sensitivity to WIMPs using unencapsulated NaI, *Phys. Lett. B* **473** (2000) 330

[Tam85a]   S.-i. Tamura, Spontaneous decay rates of LA phonons in quasi-isotropic solids, *Phys. Rev. B* **31(4)** (1985) 2574–2577

[Tam85b]   S.-i. Tamura, Maris H. J., Spontaneous decay of TA phonons, *Phys. Rev. B* **31(4)** (1985) 2595–2598

[Tin96]   M. Tinkham, *Introduction to Superconductivity*, McGraw-Hill, second Edition, 1996

[Tov00]   D.R. Tovey et al., A New Model Independent Method for Extracting Spin-Dependent (Cross Section) Limits from Dark Matter Searches, *Phys. Lett. B* **488** (2000) 17–26

[Tri73]   B. B. Triplett et al., Critical Field for Superconductivity and Low-Temperature Normal-State Heat Capacity of Tungsten, *J. of Low Temp. Phys.* **12** (1973) 499–518

[Tur90]   M. S. Turner, Windows on the axion, *Phys. Rept.* **197** (1990) 67

[Vre86]   T. Vreeland, Strain measurement in heteroepitaxial layers - Silicon on Sapphire, *J. Mater. Res.* **1(5)** (1986) 712–716

[Was86]   I. Wasserman, Possibility of detecting heavy neutral fermions in the Galaxy, *Phys. Rev. D* **33** (1986) 2071

[Web00]   M.F. Weber et al., Giant Birefringent Optics in Multilayer Polymer Mirrors, *Science* **287** (2000) 2451

[Wei72]   S. Weinberg, *Gravitation and Cosmology*, John Wiley and Sons, 1972

[Wei03]   C. Weinheimer, In *Proceedings of the 10th Int. Workshop on Neutrino Telescopes, Venice/Italy March 2003*, 2003

[Wul04a] H. Wulandari, J. Jochum, W. Rau, F. von Feilitzsch, Neutron Background Studies for the CRESST Dark Matter experiment, *Preprint* hep-ex/0401032

[Wul04b] H. Wulandari, J. Jochum, W. Rau, F. von Feilitzsch, Neutron Flux at the Gran Sasso Underground Laboratory Revisited, *Astropart. Phys.* **22** (2004) 313–322

[Yel02] S. Yellin, Finding an upper limit in the presence of an unknown background, *Phys. Rev. D* **66** (2002) 032005

[Zwi33] F. Zwicky, Die Rotverschiebung von extragalaktischen Nebeln, *Helv. Phys. Acta* **6** (1933) 110–127

Acknowledgements

While writing this work I was yearning to write the last page and now that it is done I realize that few more lines are needed to express my gratitude to those that, in many different ways, helped me to reach this end.

After a long reflection I think my first thanks should go to Prof. Dr. Biebel and to Dr. Pröbst for giving me the opportunity to put myself to the test performing this work within the CRESST group at Max-Planck-Institut in Munich. The latter I should especially thank for his constant and patient supervision that guided me through these three years of work.

A sincere thankfulness I have to express to the whole MPI group for the moral and practical support! Too many names for a list and too high risk of forgetting some! Each of them knows the reason why I feel so grateful, so I will not stay forever in front of this white sheet of paper looking for the most suitable words to say thank you... I am simply saying it now!

Those that got into my private life becoming real friends deserve special thanks, not only because they made my stay very agreeable, but because they took care of me in all possible manners.

I will not forget my little Gran Sasso family! During my shifts some of them were invaluably useful in solving many experimental problems (in spite of being not always directly involved) but all of them were invaluably useful in helping me to survive "many experimental problems"!

My family should read what I wrote about them last time... my feeling is unchanged, although I must mention that in the mean while I changed my sponsor who explicitly asked to be acknowledged. In fact I have to admit that his willingness to follow me anywhere I choused made this experience possible! Do I have to say thank you?

P.S. I am especially grateful to Barnaby who read (with impressing quickness) the whole thesis improving my English.